DETAILED DESIGN REPORT FOR DANMAX:

POWDER DIFFRACTION INSTRUMENTS

In situ materials studies in the 15-35 keV range using powder X-ray diffraction and full field imaging at MAX IV.

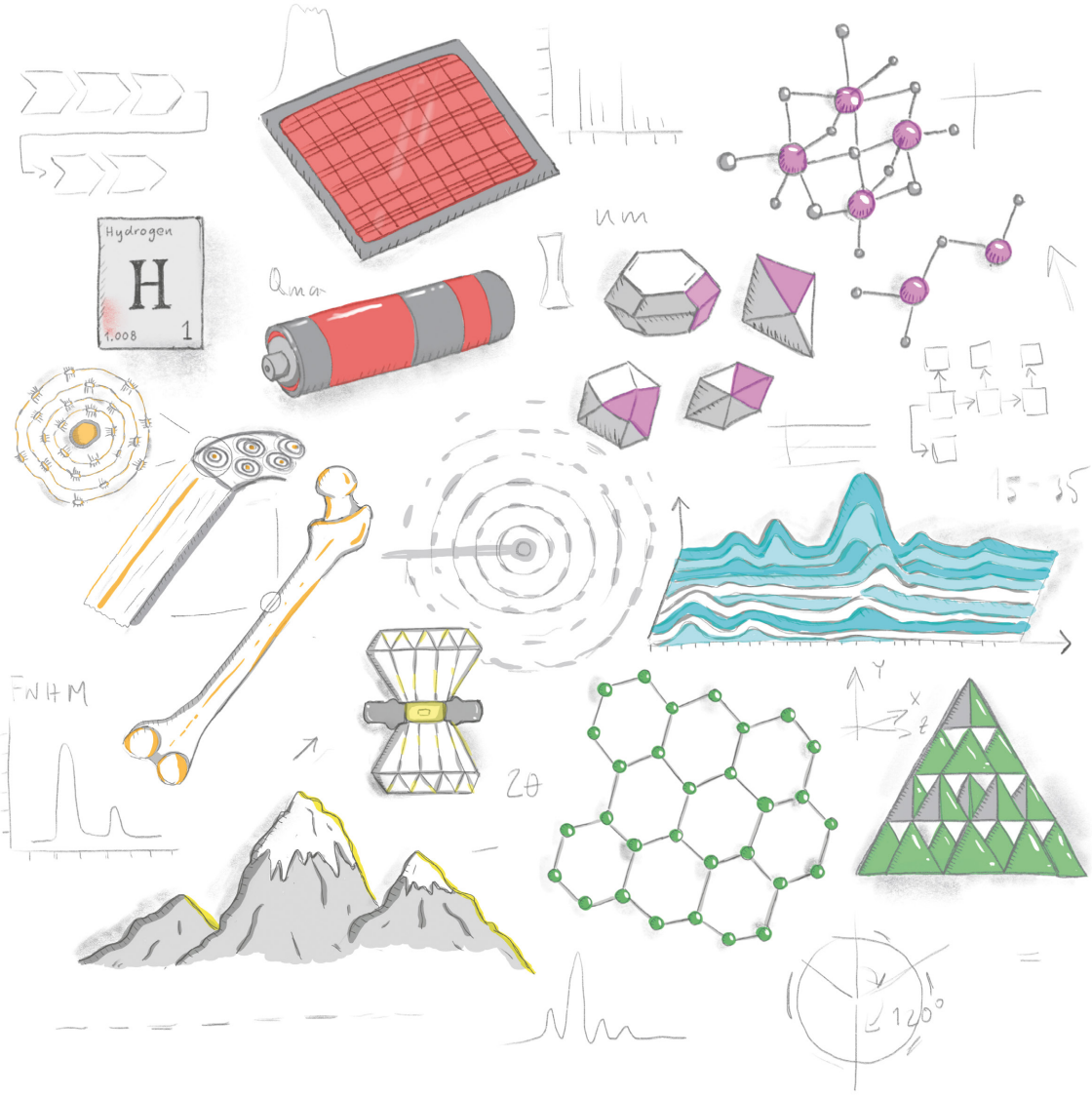

Version 2.0 - October 8, 2019

Mads Ry Vogel Jørgensen*
Department of Chemistry & iNANO, Aarhus University & MAX IV Laboratory.
Innokenty Kantor
Department of Physics, Technical University of Denmark & MAX IV Laboratory.

*mads@chem.au.dk

Cover illustration:
Emelie Hilner, 2019

Preface

This report is the second revision of the detailed design report (DDR) for the PXRD end station at the DanMAX beamline. The current version reflects the discussions, comments and suggestions put forward during the external review of the first edition of the DDR. The major change made to the end station is the location of the two PXRD instruments. In the original report the high resolution PXRD instrument was placed directly behind the imaging instrument with the area detector instrument placed further downstream. In this revised DDR the area detector PXRD instrument is placed immediately downstream of the imaging instrument and the high resolution PXRD instrument is placed several meters downstream. The report by the DDR review committee has been included in Appendix E. Concrete recommendations made by the committee are highlighted in **bold and underlined typeface** through the document.

1. Introduction

DanMAX will be a world-leading materials science beamline dedicated to in situ and operando experiments on real materials. The beamline will operate in the 15 - 35 keV range and conduct full field imaging and powder X-ray diffraction experiments. With a large and diverse user community, focus will be on high throughput and extended provision of data analysis tools. The combination of two related techniques will ensure cross talk between communities and seed new collaborations and science will profit from the high complementarity of the techniques.

The beamline is being built at achromat 4 at the MAX IV 3 GeV storage ring. The project is funded by grants from 'Nationalt Udvalg for Forskningstruktur' under the Danish Ministry of Higher Education and Science, the Capital Region, and the Central Denmark Region. In addition to these grants the MAX IV laboratory, Technical University of Denmark, Aarhus University, and University of Copenhagen are also contributing financially to the project.

Figure 1 Aerial view of the MAX IV Laboratory. Photo: Mads Ry Jørgensen

The powder X-ray diffraction instrumentation will consist of two separate instruments, one for high resolution and one for large sample environments. With these two dedicated instruments users will not have to compromise when designing their experiments and will be able to obtain the best possible data.

This document describes the detailed design of the powder diffraction instrumentation and is preceded by the DDR for the X-ray optics of the beamline (Kantor *et al.*, 2017). A similar document describing the detailed design of the imaging instrumentation has been prepared and reviewed parallel to this document. The focus in the report is on the larger pieces of equipment that need to be procured and a less detailed description on the smaller custom-engineered pieces of equipment. During the revision of the report a beamline engineer has joined the team. She will work on the detailing and interfacing of the remaining items.

Contents

This page is intentionally left blank

2. Beamline Layout

The overall layout of the beamline, see Figure 2, and in particular the experimental hutch was presented for the DanMAX consortium at the second DanMAX Users Meeting on 16 January 2017. The layout of the PXRD instrumentation with two stations; one for high resolution and one with a very flexible set-up with an area detector for large sample environments (SE), were found to be well-suited for the science cases presented in the Conceptual Design Report (CDR, Gundlach *et al.*, 2014), and the following discussion forms the basis for the work described in this document. The optical layout of beamline is summarized in section 3. A detailed description of the optics and expected performance is given in the Detailed Design Report (DDR, Kantor *et al.*, 2017).

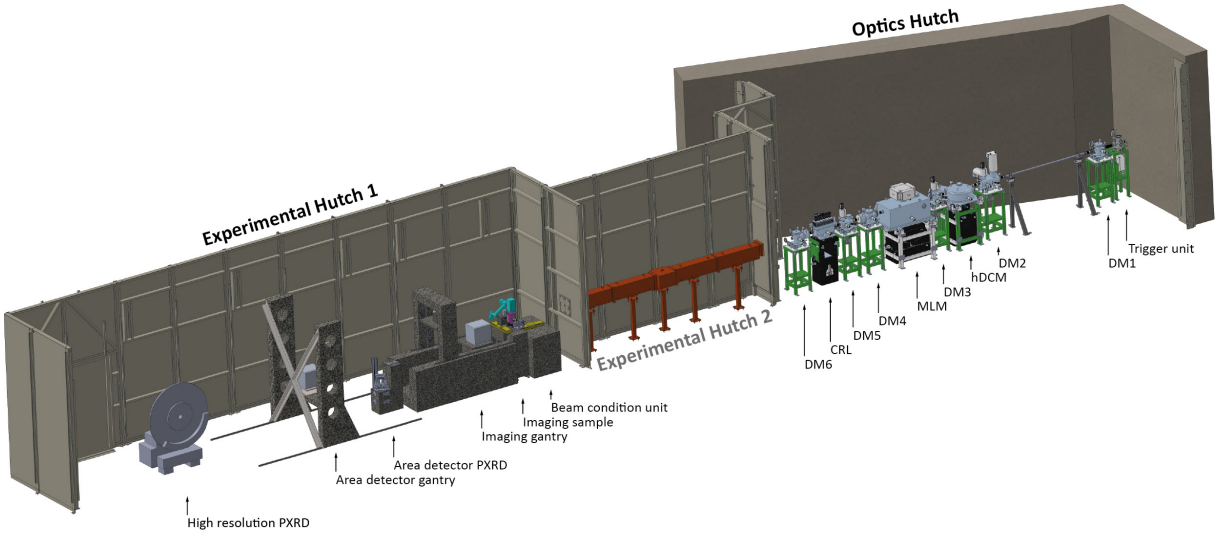

Figure 2 Layout of the DanMAX beamline. DMX consists of various diagnostics modules containing, filters, beam viewers, slits, and radiation safety equipment.

The dimensions of the DanMAX experimental hutch 1 (EH1)[1] is approximately 14 m in length by 4.5 meters in width. The hutch is quite long to ensure a large sample to detector distance for dark field diffraction imaging which is preferably up to several meters, but it also offers more flexibility for new developments for future upgrades. The benefit of PXRD is that the detector gantry can be shared to save cost and increase the flexibility of detector positioning.

We have opted for two dedicated set-ups for PXRD instead of one multipurpose set-up that would likely have resulted in some compromises. The two proposed instruments are:

- *Flexible setup with Area Detector for large sample environments (PXRD 2D)*. This instrument is built around a hexapod that can accommodate bulky and heavy sample environments (SE). The main detector used for this setup will be a CdTe based pixel detector. To better facilitate high maximum Q measurements for, e.g. total scattering (TS) experiments, a large area amorphous silicon flat-panel detector will likely also be available. The detector positioning stage will offer large flexibility in both sample to detector distance and in detector tilt to

[1] A second experimental hutch, EH2, has been constructed, but is not shown in Figure 2. The technique for this additional beamline has not been decided nor has the funding for optics and instrument been obtained at this time.

increase the attainable Q range. The detector positioning stage is also used for the far field imaging detector and the final specification is not included here. The specifications given are the minimum requirements for PXRD. The instrument is described in detail in section 4.

- *High resolution instrument (PXRD 1D)* with a sturdy and precise goniometer which holds a 1D microstrip detector covering a large angular range and smaller SE. To a large extent this set-up will be used for data collection on capillary samples. The instrument will have a robotic sample changer and use an automatic sample alignment system, thus ensuring optimal data quality. The instrument will furthermore have a motorized table with a breadboard layout to mount SE. The instrument is described in detail in section 5.

The choice of two instruments is largely determined by the requirements stated in the science cases as described in the CDR. DanMAX should be able to both measure data with good peak resolution and data with a high maximum momentum transfer, Q, but also measure data with a good temporal resolution and with azimuthal information for, e.g. texture analysis.

The former can be obtained with a 1D microstrip detector, which can have a very large angular coverage, as illustrated in the left panel of Figure 3. However, due to the narrow width of such a detector, the solid angle covered is rather small, and thus, the counting time for data with a high signal-to-noise ratio (SNR) will be increased. Furthermore, only a narrow slice in the vertical scattering plane is collected and thus no information about texturing is obtained.

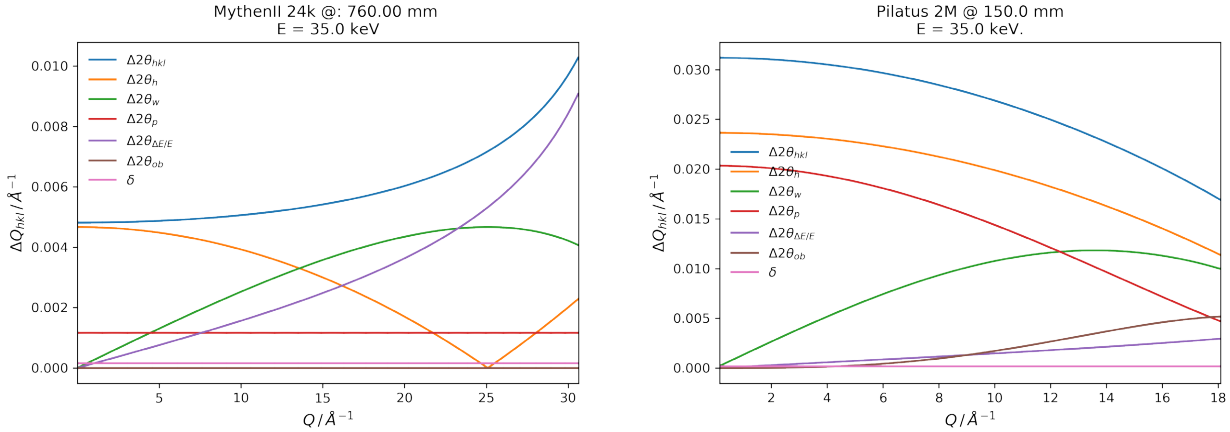

Figure 3 Estimated geometrical contributions to the peak broadening as defined by Dippel *et al.* (2015). The different effects are shown and the subscript refers to; *h*: sample height, *w*: sample thickness/diameter, *p*: pixels size, *ob*: obliqueness, *ΔE/E*: energy band pass, and *δ* is the beam divergence, in this case 9 µrad. Left: A simulated MYTEH2 24K detector with a 50 µm pixel size and a sample to detector distance (SDD) of 760 mm. Right: A simulated PILATUS 2M with a pixel size of 172 µm and a SDD of 150 mm. The simulated detector is moved up by 130 mm to increase the accessible Q range. The direct beam would hit the detector at approximately 14 mm from the lower edge. In both cases a sample of ⌀200 µm has been used.

By using an area detector, data can be collected in a larger solid angle, thus increasing the number of photons detected and thereby the overall temporal resolution of the experiment. It also yields information about the texture of the sample as a larger part of the Debye-Scherrer cone is recorded. The peak resolution on the area detector is often poorer than on the microstrip detector and is highly correlated with the detector distance. In the right panel of Figure 3 this is illustrated for a typical set-

up where the detector is placed close to the sample for maximal coverage. It can be seen that the peak width is expected to be approximately 5-6 times that of the high-resolution set-up. At larger distances, the peak resolution improves at the expense of smaller angular coverage due to the limited size of the detector.

2.1. Layout of Conventional buildings

The layout of the beamline is shown in Figure 4. A room equipped for simple sample manipulation and preparation of sample environments is located adjacent to EH1. The normal entrance to EH1 is through this room. A chicane intended for user equipment for EH1 is located in this room as well. The room is equipped with point ventilation, thus allowing soldering, gluing and other tasks and minor repairs to be carried out. There is no drain at the beamline, and thus, no sink nor running water is installed. A fully equipped chemistry lab is located across the outer walkway around the experimental hall. This lab is shared with the other beamlines, and is where most of the sample preparation is expected to take place.

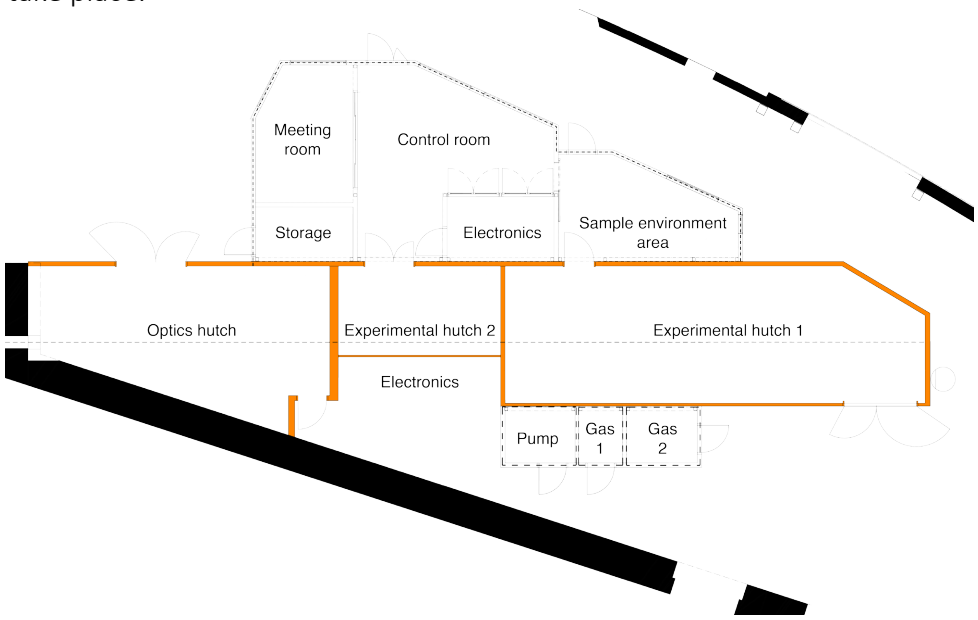

Figure 4 Layout of the beamline. The beam path is illustrated as the horizontal dashed line. The radiation safety hutches are shown in orange.

The control room is connected to the sample environment area through a sliding door. Here a long table has been installed with space for 4-5 operators. Behind the operators there is access to 4 of the electronics racks at the beamline. Here we will mount the motor control for the end station and detector servers. The remainder of the racks, six full size, have been installed in the area labeled 'Electronics' on the inboard side of EH2 in Figure 4 . Adjacent to the control room we have a meeting room available for users when they work on data reduction and modeling. This room is prepared for easy reconfiguration into a control room for EH2 in the future.

2.1. Experimental Hutch 1 Layout

The floor plan of EH1 is shown in Figure 5. The inner dimensions of the hutch are 14.0 by 4.6 meters. The beam enters the hutch at 38.1 m from the source. The beam is located at 1320 mm above the floor and ~2 m from the back (inboard) wall. There are two entrances to the hutch; a set of large double doors, w2000 x h2300 mm opening, on the inboard side at the downstream end of the hutch, and a single door, w900 x h2000 mm opening, on the outboard side of the hutch at the upstream

end. The single door is the normal user entrance, while the double doors will be used for moving equipment in and out. A crane rated at 1000 kg is available and can access most of the floor area in EH1, see the hatched area in Figure 5. The height of the radiation safety hutches is approx. 4.2 m. However, the crane and ventilation restrict the useable height to 3.1 m.

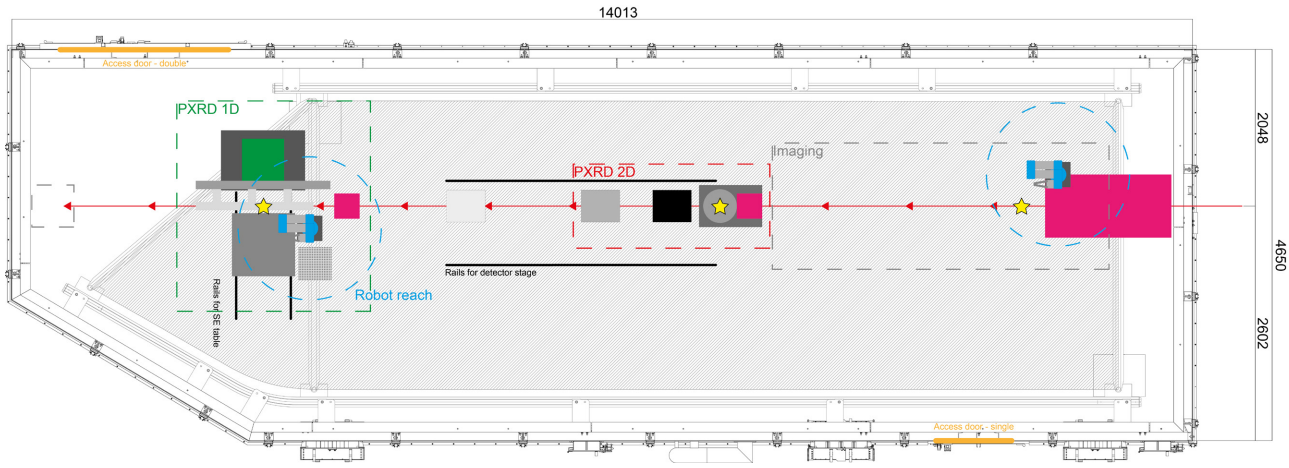

Figure 5 Layout of the PXRD instruments in the experimental hutch. The beam is illustrated by the red line and the arrows indicate the beam directions. The sample positions are marked with yellow stars and the instrument outlines with dashed lines. The beam conditionioning unit and the slits and ion chambers for the two PXRD instruments are marked with pink squares. PXRD 1D corresponds to the high resolution set-up, while PXRD 2D corresponds to the area detector set-up. In the figure the three positions of the area detector is shown in black and two tones of grey.

The first component in EH1 is a vacuum window to separate the vacuum in the experimental hutch and the UHV conditions in the optical hutch (OH) and the storage ring. This window is detailed in section 3.1. A range of equipment for beam conditioning is placed just downstream of the window. This beam conditioning unit is further discussed in section 3.2.2.

The imaging sample goniometer and near field detector support will follow downstream of the beam conditioning unit. The setup needs to be very stable and will be made from granite or similar. The design of the setup is described in the imaging DDR. It will be ~4.5 m long, and the sample position for the imaging goniometer is approx. 40.1 m from the source. For the dark field microscopy option, a relatively large sample to detector distance is needed, i.e. this instrument is placed with the sample position upstream in the hutch and the detector gantry is placed further downstream.

The PXRD 2D instrument is placed immediately downstream of the imaging instrument and upstream of the high resolution instrument. This location minimizes the blind regions for the dark field microscopy set-up. The sample position is approx. 43.5 m the source. The sample stage is quite short (<1 m), but the total length of the instrument varies based on the detector distance. The detector positioning stage is also used for the far field imaging detector and the final specification is thus not included here, but will appear in the DDR for the imaging instrument.

The high resolution PXRD 1D instrument is placed downstream of the other instruments and will have a sample position at 49.0 m from the source. The length of the instrument is approximately 2.5 m.

By moving the detector gantry all the way upstream, it will be possible to (temporarily) install an instrument that is up to approximately 4 meters in length between the two PXRD instruments. We also foresee that a small detector table can be installed at the very downstream end to accommodate area detectors for, e.g. ptychographic experiments or small angle X-ray scattering. This will be a future addition and should be driven by an interesting science case and by the user community.

Most of the PXRD experiments will use rather large beams and thus temperature stability is not a major issue. However, for experiments with highly focused beams temperature stability is a concern. This is also the case for imaging experiments as temperature changes will deteriorate the resolution. The ventilation system of EH1 was specified to be stable to within ±1 °C. This is not the temporal stability, but instead it means that the temperature is ±1°C in all locations of the hutch. The temporal stability should be much better and only slowly changing temperatures (day/night) is expected. All pieces of equipment generating a lot of heat will be moved outside EH1, if at all possible. It may also be possible to construct a small climate controlled tent around the entrance to EH1.

Cooling water is available with outlets in three locations along the inside wall of EH1. Furthermore, pressurized air and nitrogen gas is available near both the imaging instrument and the area detector instrument.

This page is intentionally left blank

3. X-ray Source and Optics

DanMAX will utilize a 3m long in-vacuum undulator with a magnetic period of 16 mm and a minimum gap of 4 mm to maximize the available flux at 35 keV. The full details of the IVU is given in the DDR. Based on the requirements stated in the CDR and the DDR we have designed the optical scheme illustrated in Figure 6. Overall, the beamline will have two modes of operation: high energy resolution or high intensity. This is possible by using two monochromators; first a cryo-cooled Si (111) double crystal monochromator (DCM) followed by a water-cooled multilayer mirror monochromator (MLM). To decrease vibrations, both monochromators are horizontally deflecting, thus, ensuring a more stable beam.

By combining the two monochromators, the beamline can run in three different modes:

- *DCM only*: Monochromatic mode without harmonic rejection. This option ensures the highest monochromatic flux and preserved coherence. This mode is intended for phase contrast imaging, diffraction contrast imaging and PXRD in the range 20-35 keV[2].

- *DCM and MLM*: Monochromatic mode with harmonic rejection. The DCM determines the band pass and higher harmonics (HH) are rejected by the MLM. In some cases this option is necessary for PXRD and diffraction contrast imaging at lower photon energies (15-20 keV).

- *MLM only*: Quasi-monochromatic mode. The band pass of the MLM is determined by the multilayer coating(s), thus leading to a quasi-monochromatic beam with very high intensity. This operational mode is perfect for, e.g. fast absorption contrast imaging and fast, albeit low resolution, diffraction. This mode can potentially also be used to obtain a more intense flat field for faster detector calibration.

In the three different modes the total offset of the incoming and outgoing beam is always 10 mm. This ensures that only minimal alignment is needed when changing modes.

Finally, the beam size/divergence can be adjusted by inserting Be compound refractive lenses (CRL) into the beam. The beam size can be adjusted from approx. 5 x 50 μm^2 to 1.3 x 1.2 mm^2 (FWHM) using the CRLs in the optical hutch. For PXRD experiments requiring smaller beams than this, additional optical elements will be added in the experimental hutch to focus the beam even tighter, see section 7.

The expected performance of the optics is described in detail in the DDR and will not be repeated here. The only simulation of the optical system that will be conducted for this report is the requirements for the secondary focusing optics for tighter focus necessary for, e.g. high pressure and spatially resolved experiments.

[2] The energy at which HH rejection is no longer an issue is unfortunately not known as the commonly used undulator spectrum codes are not precise at high energies. The simulations based on these codes thus become highly imprecise and overestimate the HH flux, e.g. increasing HH fraction as a function of energy, which is clearly unphysical.

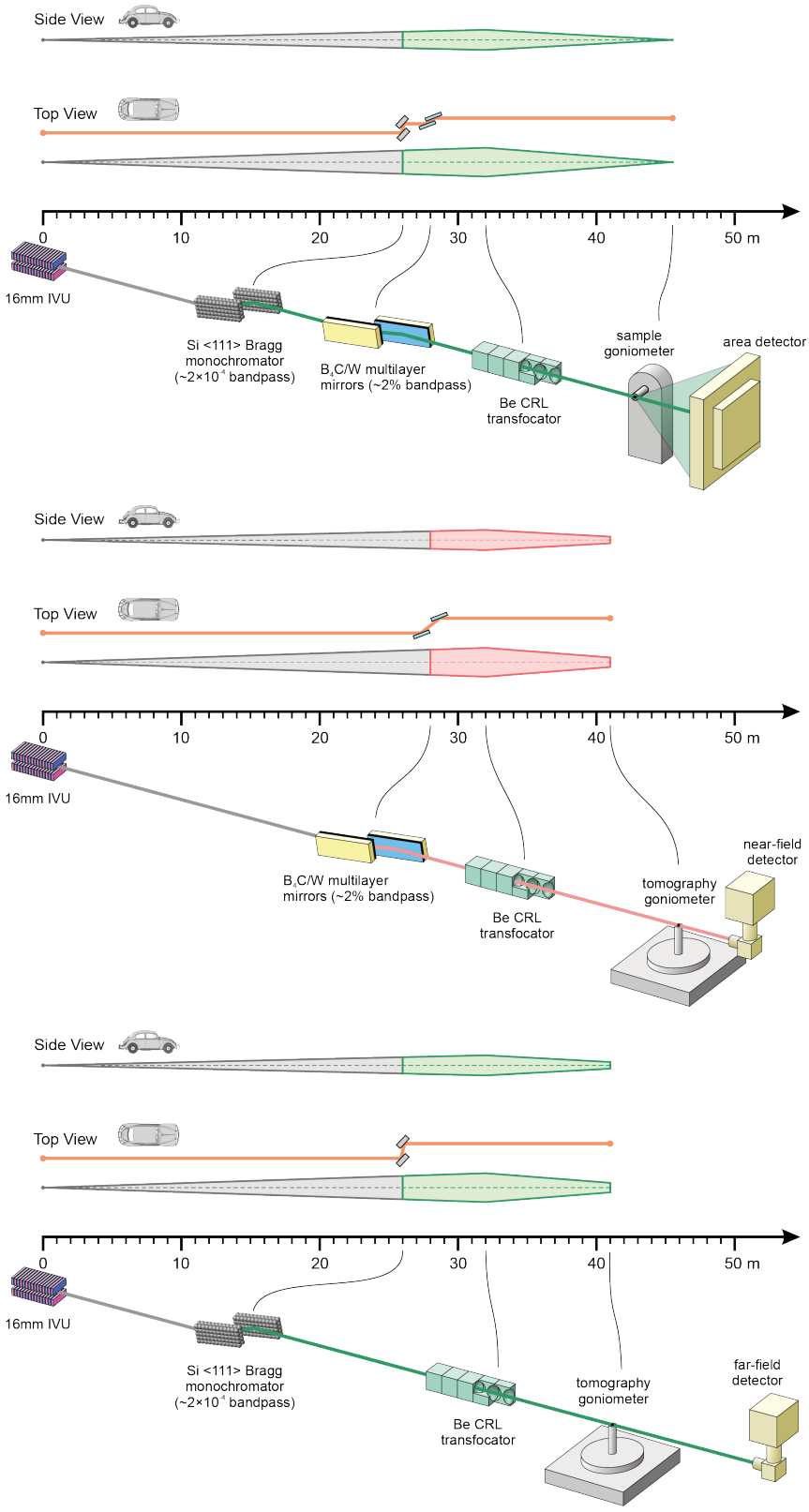

Figure 6 Optics Layout for DanMAX. Top: Narrow bandwidth with harmonic rejection using both Si (111) hDCM and multilayer mirrors. Middle: High intensity mode using only multilayer mirrors. Bottom: Narrow bandwidth without harmonic rejection using only Si (111) hDCM. All modes can be used for both PXRD and imaging.

3.1. Vacuum System in EH1

To separate the UHV zone in the OH and beam transport tube (and the machine!) and ambient conditions (or low vacuum) in EH1, a window is needed.[3] To preserve coherence, this window must either be very a thin, amorphous and homogeneous compound, or be constructed from a polished single crystal. The aperture of the window shall be ~ø3 mm, to match the unfocused beam size, which is 1000 x 1000 μm^2 (FWHM) at this point. The window can be made from either diamond, glassy carbon, or SiN. Glassy carbon is quite brittle and while it is cheaper than diamond its performance is likely lower. Single crystal diamond windows in UHV flanges are commercially available. The 'rule of thumb' is that the thickness must be 1.7% of the aperture diameter[4], i.e. 55 (85) µm for a ø3 (ø5) mm window. At this minimum thickness, the window is presumably quite sensitive to pressure waves, and thus, we suggest using a significantly thicker window to minimize the risk of venting the optics. Our preferred solution is a 250 µm thick single crystal diamond solution.

The vacuum system in EH1 must be highly flexible to allow for the installation of evacuated beam tubes to the instrument in use. To ensure fast and easy installation we will use KF40 fittings. Since the absolute vacuum level is not critical, we will have a scroll pump located in the pump room outside EH1 to minimize vibrations near the experiments. The vacuum connection to this pump will be fairly long, and thus the vacuum conductance will be poor, but should be sufficient to reach the desired vacuum level (~mbar). To achieve flexibility, it is also necessary that various equipment along the beam path can be removed, e.g. focusing and sample holder at the imaging instrument and slits and ion chambers at PXRD 2D.

Due to the flexibility of the vacuum system, unfortunately the risk of rapid ventilation, and thus the creation of a pressure wave, exist. The window described above is the only separation between the experiment (i.e. ambient conditions) and the optics and machine! It is therefore of utmost importance to protect this window. The beam conditioning unit (section 3.2) will effectively protect the window.

3.2. Beam Conditioning Unit

Various shared units for beam conditioning will be placed on a common support at the upstream end of EH1. This includes (from upstream to downstream): beam position monitor, shutter, attenuator, alignment laser, decoherer, slits and a small windowless ion chamber. In addition to this, the unit will also hold the beam condenser and sample changing robot for the imaging instrument. All of this equipment will be on a granite, or synthetic granite, support. The assembly is shown in Figure 7. The beam conditioning unit will be installed alongside the PXRD 2D sample stage.

[3] To prevent accidental venting of the machine, a pressure gauge in the OH is connected to a fast closing valve in the FE.

[4] http://www.diamond-materials.com

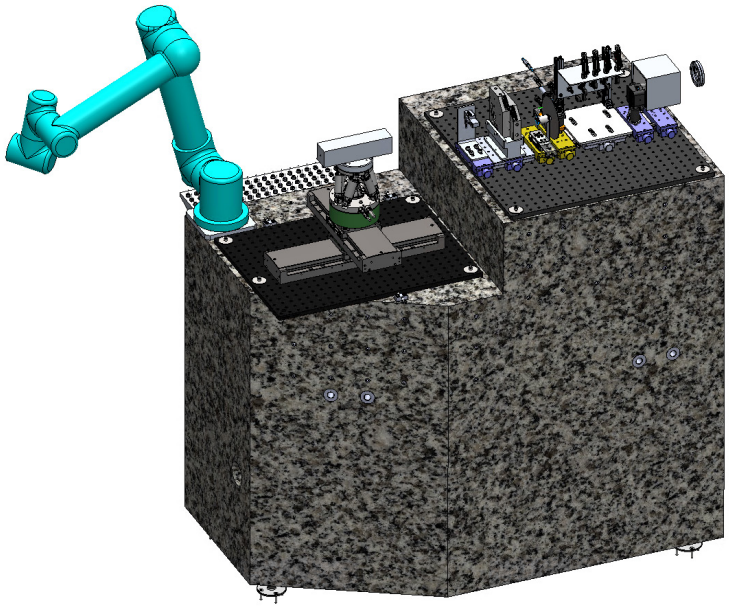

Figure 7 Beam conditioning unit. The beam will enter through the diamond window in the flange on the right side.

3.2.1. Shutter

Most of the anticipated experiments will rely on gating the detectors to determine exposure time and not on a mechanical shutter. It will nevertheless be advantageous to have a mechanical shutter in the experimental hutch to protect the sample from radiation damage, while, e.g. the SDD or sample temperature is changed. It will also be useful for collecting dark frames, e.g. when using an aSi detector. Several commercial solutions with high reliability and fast opening times are available, e.g. from Cedrat[5] and Arinax[6]. The expected experiments at DanMAX does not need a very fast response time as the exposure time is controlled by gating the detectors. Thus, we suggest to use the same solution that is adapted at the Balder beamline, namely using a laser shutter from Thorlabs,[7] but exchanging the aluminum shutter blade with tungsten or tantalum. This is a very cost effective solution.

3.2.2. Attenuator

It is often necessary to attenuate the beam, either to spare the sample the full intensity of the beam, to decrease the diffracted signal to the bounds of the detectors dynamic range (especially for aSi detectors) and particular during the installation and alignment of beam stops, etc.

The device must allow for stepwise changes of the attenuation by utilizing several attenuators with varying thicknesses. Similar attenuators are utilized in many beamlines and several designs exist. It is proposed to use both W and Ni as these metals are available in various thicknesses and do not have any absorption edges in the 15-35 keV range. They are both available in high purity, have good mechanical stability, and are stable under ambient conditions. A versatile design using six foils will allow for a wide range of attenuation for all energies, see Table 1.

[5] http://www.cedrat-technologies.com/fileadmin/user_upload/CTEC/Applications/Instrumentation/brochure-synchrotron.pdf
[6] https://www.arinax.com/colibri-x-ray-fast-shutter/
[7] https://www.thorlabs.com

Table 1 Transmission of X-rays for various Ni and W foil thicknesses (d) at three different photon energies (E).

E (keV)	D (μm)						
	Ni: 25	Ni: 50	W: 50	W: 100	W: 200	W: 400	All:
15	0.233	0.054	4.8e-6	2e-11	5e-22	3e-43	2e-82
25	0.670	0.449	0.046	2.1e-3	4.5e-6	2e-11	3e-21
35	0.855	0.732	0.222	0.049	2.4e-3	5.9e-6	1e-10

The foils will be mounted in holders driven in and out of the beam using pneumatic actuators. In addition to the foils listed in Table 1, we will also have one to two additional holders to accommodate foils for absolute energy calibration, e.g. Mo. The design must be able to accommodate limit switches to give reliable feedback to the operators. The attenuator will be placed upstream of the imaging setup and may incorporate a ∼ø1 mm pinhole to minimize scattering from the polycrystalline foils.

3.2.3. Alignment Laser

To aid in instrument, SE and beam stop alignment, it is preferable to have a pre-aligned laser that can be inserted into the beam path. The laser should emit 532 nm (green) light for maximum visibility. The power output should be low enough so that no laser safety system is required. To align the laser, translation perpendicular to the beam (XY) is needed as well as pitch and yaw adjustments. In practice the laser will be mounted perpendicular to the X-ray beam to save space, and the beam will be reflected along the X-ray beam path using a mirror. The laser will be adjustment along YZ, and the pitch and yaw will be adjusted on the mirror in the beam path. These adjustments should be manual. The movement of the set-up in/out of the beam paths should be remote controlled, e.g. with pneumatics.

This page is intentionally left blank

4. Area Detector Instrument, PXRD 2D

The science case for the beamline formulates a need for a flexible general purpose instrument that can handle a wide range of sample environments (SE) and obtain high quality data with good time resolution. To facilitate this, we propose an instrument with a flexible hexapod sample stage and a detector positioning gantry that can accept various different area detectors. The detailed description of the instrument is presented in this section.

4.1. Area Detectors

Area detectors are very powerful tools for diffraction as a large volume of reciprocal space can be collected at once. The resolution is in general not as high as point or strip detectors due to larger pixels and/or geometrical factors. However, by increasing the SDD a better resolution can be obtained at the expense of lower reciprocal space coverage. As area detectors collect data on a large azimuthal section of the Debye-Scherer cone, it is possible to obtain information about texturing or alternatively if the sample is isotropic, increase the signal statistics by azimuthal averaging.

Two types of area detectors are foreseen at DanMAX; hybrid pixel array detectors (HPAD) and amorphous silicon (aSi) TFT panels with CsI:Tl scintillators. HPADs, described in detail below, are currently the state-of-the-art and do have a lot of highly attractive features. They are, however, also quite expensive, and thus, the size of such a detector will be limited due to budgetary constraints. On the other hand aSi panels are a known and proven technology that does have lower dynamic range, image lag and higher noise than the HPADs. However, these detectors are available with a large active area and at a much lower price than HPADs. The specifics of the two types of detectors are discussed below.

4.1.1. Hybrid Pixel Array Detectors

HPADs are direct detection devices where the energy from an absorbed X-ray photon excites an electron to the conduction band. This electron loses its energy by interacting with other electrons, thus creating a large number of electron-hole pairs inside the sensor material. This charge[8] is pulled into the detection and counting circuit using a bias on the sensor. The sensor is bonded directly to the readout electronics. The electronics vary between manufacturers, but in general the charge pulse is amplified and compared to a threshold. If the pulse is higher than the threshold, and the electronic shutter is open, it is counted. I.e. HPADs are photon counting detectors. The threshold can be used to discriminate against low energy photons to, e.g. suppress fluorescence. The threshold is normally set to half the pulse height, equivalent to half the photon energy. This ensures that a photon hitting on the border between two pixels will only be counted once. In case the photon hits the corner shared between four pixels, it may not be detected as the charge is shared between four pixels and is likely to be below the threshold in all pixels. This effect, charge sharing, can be a problem for very sharp and local intensities, e.g. from single crystal diffraction. For PXRD the signals are distributed over many pixels and this effect will just lead to a slightly lower detector efficiency overall. The threshold also filters out any electronic noise (at least in the energy range of DanMAX), and thus the signal to noise in HPADs is excellent. Similarly, since the noise is extremely low and the counters are very deep (often >20 bit), the dynamic range is much larger than conventional area detectors, such as imaging plate scanners, CCDs, and CMOS. The large area detectors are built from a number of

[8] For the Dectris (https://www.dectris.com) PILATUS series, holes are detected for the Si version and electrons for CdTe.

separate modules. The modules used in the Dectris PILATUS3 detectors have modules with an active area of 83.78 x 33.56 mm^2. This means that inactive regions exist between the modules. The regions will normally not pose a big challenge as it is possible to position the detector such that data is collected at all momentum transfers at different azimuthal angles. However, for the most accurate experiments it may be necessary to translate the detector and do multiple exposures to 'fill in' the missing regions. Each module (in the Si PILATUS3) is composed of 8 x 2 read-out chips providing a continuous active region. However, near the edges of the read-out chips the pixels have a 1.5 times larger area. In the corner the four adjacent pixels have a 2.25 (1.5^2) times larger area. The counts from these edge/corner pixels are subsequently distributed equally to three/nine normally sized pixels by the software (Kraft *et al.*, 2009).

Three materials are currently commercially available as sensors in HPADs; Si, GaAs and CdTe. For the energy range 15-35 keV GaAs is superior to Si and CdTe (Brönnimann & Trüb, 2016). However, Si and CdTe are more (commercially) developed and are the only ones to be discussed in detail. The X-ray absorption in a 1000 µm thick Si wafer is approximately 90% at 15 keV, but decreases to approximately 20% at 35 keV. This means that the efficiency of a HPAD with a 1000 µm thick Si will necessarily be lower than 20% at the highest operating energies at DanMAX. In addition to being less efficient, this also leads to severe parallax and oblique incidence effects as the attenuation length is very large compared to the pixel size at high oblique incident angles. The parallax effect is that the electron cloud is not necessarily created in the pixel where the photon arrived at the front of the sensor, leading to a geometrical distortion. The oblique incidence effect is that the effective path length through the sensor is larger at large oblique angles, and thus the chance of interaction is higher. This leads to higher apparent signals at higher incident angles (Hülsen *et al.*, 2005). Another undesirable effect is that some of the penetrating beam will hit the electronics beneath the sensor layer, leading to backscattering and thus higher noise. It will also have a negative effect on the lifetime of the electronics. For a 300 µm thick Si PILATUS pixel the lifetime is estimated to be 10^6 Gy, which corresponds to approximately 100 days of continuous illumination of 12 keV photons at a count rate of 10^6 cps (Brönnimann & Trüb, 2016).

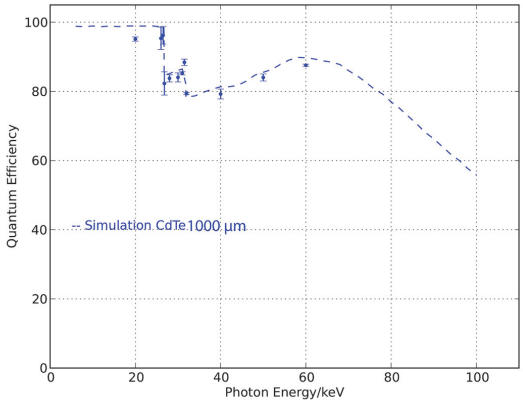

Figure 8 Quantum efficiency of the PILATUS3 X CdTe detector module measured in cooperation with PTB at the BAM beamline at BESSY II. The dip in the QE from above 26 keV is caused by fluorescence losses occurring for photon energies above the Cd and Te K-edges. The QE is measured for energy threshold set to 50% of the photon energy. Figure credit: Dectris AG (https://www.dectris.com).

In the case of the CdTe sensor based HPADs the absorption is close to 100%, and the attenuation length is very short in the full energy range of DanMAX. This translates into high efficiency, no oblique

incidence effects and only small (probably undetectable) parallax effects. However, it should be noted that both Cd (K edge at 26.7 keV) and Te (K edge at 31.8 keV) have absorption edges in the working energy range. These absorption edges and fluorescence decrease the efficiency to approximately 80% in the range ~26-45 keV, see Figure 8. Experiments should be designed in a way to avoid the absorption edges. The point spread increases by approximately 20% above the above-mentioned the Cd K-edge. A problem with CdTe HPAD detectors has been the so-called polarization effect, which changes the detector performance as a function of time under biasing. However, according to marketing material from Dectris the problem is now limited to variations less than 1% at 2.5 x 10^6 cps/pixel over periods of 'several hours'. This seems to be consistent with the experience at other beamlines utilizing this detector. Another issue with the CdTe detector is that the sensor is not available in wafers large enough to make a seamless module as for the Si version. The PILATUS3 CdTe modules are therefore constructed with two sensors each covering 4 x 2 read-out chips. This leads to a 3 px wide gap in each module. This may lead to additional difficulties for the most accurate experiments.

The area detector will not only be used for PXRD, but may also be used directly on the imaging stage. The active area of HPAD detectors are often covered in metalized mylar film, which offers the underlying delicate modules little protection against impact. A shield that protects the detector form accidental impact while moving the detector and changing setup or sample must therefore be implemented. Additionally, careful planning is required and procedures need to be in place when moving the detector. Review panel suggestion: "It might be worth considering having two sets of cables installed for the two experimental stations to reduce risk and time overhead when swapping the detector [Pilatus 2M] between setups."

Since HPADs are photon counting detectors, they do suffer from dead time effects at high count rates. The problem arises when a pulse arrives at the comparator before the signal from the prior pulse has fallen below the comparator threshold. The dead time depends on the gain of the signal amplifier and thus, the photon energy. The effect is well characterized, and a correction can be applied reliably up to a certain cut-off rate. The Dectris PILATUS3 detectors employ a retriggering mechanism which assumes a certain peak time after which the comparator will be active again and will count another photon if the level is still above the threshold. This increases the usable count rate from approx. 1.5 x 10^6 cps/pixel to approximately 5 x 10^6 cps/pixel. It is worth noting that the recorded intensity does not obey Poisson statistics if the rate correction is applied (Brönnimann & Trüb, 2016). It should also be noted that the count rate limitations depend on the bunch mode of the synchrotron storage ring, especially in the case of large bunches in certain timing modes, yielding very high instantaneous count rates that can saturate the detector (Trueb *et al*., 2012, 2015). It seems that the corrections are able to model the data from different bunch modes. However, the performance should be verified by Monte Carlo models if MAX IV plans to start running in timing or hybrid filling modes. It should be noted that there are currently no plans to implement timing modes at MAX IV as these will increase the emittance.

A few companies have developed commercial HPAD detectors, e.g. Dectris, (imXPAD[9]) and X-Spectrum[10]. The Dectris PILATUS3 series is based on readout chips developed by the company,

[9] The imXPAD webpage (http://www.imxpad.com/) is no longer available and the company is presumably closed.
[10] http://www.x-spectrum.de

whereas the X-Spectrum Lambda series is based on the Medipix3 readout chip. Each of these has its own merits and features. The Medipix3 chip for example has dual counters and two thresholds that can be used for, e.g. zero-readout time or discrimination of higher harmonics. These features, however, result in a reduction of the counter to a depth of only 12-bit; which is too low for diffraction data (unless frames of very low exposure time are acquired and subsequently summed). An advantage of the Medipix3 is the small pixel size, 55 µm, compared to the 172 µm pixel size in the PILATUS3.[11] HPADs are built from individual modules and thus, it is in principle possible to tailor the size and the geometry to the experiment. For the available (off the shelf) detectors there is a large difference between active areas. The largest available X-Spectrum detector is the 2M with an active area of approximately 8 x 8 cm^2. Larger sizes can be custom-made. However, the cost and necessary computing infrastructure for such a large detector of this type is prohibitive. The PILATUS3 X CdTe series is available in up to 2M with an active area of approximately 25 x 28 cm^2 and must be considered the superior choice despite the large pixel size. Specifications are listed in Table 2.

Table 2 Comparison of potential HPAD detectors for DanMAX

	X-Spectrum Lambda 2M (GaAa/CdTe)	Dectris PILATUS3 X CdTe 2M
No of modules	3	3 x 8
Active area [mm^2]	~84 x 84	253.7 x 288.8
Pixel size [μm^2]	55 x 55	172 x 172
Number of pixels	1536 x 1528	1475 x 1679
Max count rate [cps/pixel]	7.5 X 10^5	1 x 10^7
Max frame rate [Hz]	2000 (12 bits) – 1000 (24 bits)	250 (20 bits)
Readout time [ms]	0 (12 bits) – 1 (24 bits)	0.95
Counter depth	24 bit	20 bit
Threshold energy [keV]	5-50 / 5-75	8-40

4.1.2. Amorphous Silicon Detectors

Large flat panel detectors based on a photosensitive amorphous silicon TFT circuit coupled to a CsI:Tl scintillators have been developed primarily for medical imaging. These detectors initially had low dynamic range and poor distortion and flat-field corrections and were unsuited for diffraction purposes. Many of these problems have been solved/improved, and the detectors have found their way onto synchrotron beamlines during the last decade and are used for diffraction at, e.g. ID22@ESRF, 11ID@APS, P02.1 and P07@PETRAIII. These detectors are also being planned/commissioned at new beamline projects, e.g. I15-1@Diamond and P21@PETRAIII.

The CsI:Tl scintillator crystals grow in needle shapes which are aligned with their long axis perpendicular to the detector face. This helps to improve the point spread function as the light created is internally reflected inside the crystal along the needle axis towards the photo sensor. The point spread is slightly larger than a pixel. The absorption edges (K) for Cs and I are 36.0 keV and 33.2 keV, respectively. This will likely increase the point spread function and lower the DQE for the detectors or cause a non-uniform response at energies above 33 keV.

[11] Dectris offer another detector series 'EIGER X' with a 75 µ pixel size. It has recently become available with CdTe sensor. However, it is approximately 50-70% more expensive per unit area compared to the PILATUS3 X CdTe series.

Commercially available aSi detectors have up to 16 bit dynamic range. However, as the noise level in these detectors is substantial it is necessary to subtract a dark image. This is normally performed directly in the detector control software. An intrinsic effect of the aSi detector is 'image lag' (or ghosting) where some of the signal is apparent on subsequent frames. This effect amounts to typically a few percent after the initial readout (Lee *et al.*, 2007). This is an important effect if the diffraction intensities are changing positions rapidly, but in many cases, it is not a major problem. At the I15-1 beamline the experience is that the aSi detectors perform best when they are externally triggered at a constant rate[12]. The start and stop procedures of the readout apparently cause changes in the dark current and thus decrease the data quality. This, however, means that external signals cannot trigger the detector, and the SE will have to be synchronized to the detector trigger. It also means that the data collection system will have to decide which of the frames in the continuous data stream should be kept and which ones should be deleted immediately. The experience at various beamlines suggest that part of the noise is correlated with the temperature of the detector which varies depending on the usage pattern, i.e. the dark frames should ideally be re-recorded before each exposure. This leads to lower time resolution, and it is thus preferable to avoid this. To minimize the effect, several beamlines add active cooling to the detector.

To our knowledge, only aSi detectors from General Electric (GE) and PerkinElmer (now Varex Imaging[13], VI) have been employed for PXRD at synchrotron facilities. Detectors from GE are available, but we have not been able to obtain specifications from the company. The specifications of the suitable detectors from VI are listed in Table 3.

Based on the experience at the XPDF beamline at Diamond, the XRD1611 has slightly less noise than the XRD4343, however, it is also less efficient. At DanMAX the energy is lower and the efficiency should be good in either case. The frame rate of the XRD4343 is four times faster, which could become useful, but in contrast has lower resolution than the XRD1611 due to the larger pixels. The effect of resolution is explored in section 4.3, where the two are also compared to the PILATUS3 2M. A minor benefit of the XRD4343 is its narrow bezel, ~19 mm, allowing for, e.g. simultaneous PXRD/PDF and SAXS experiments.

Table 3 Comparison of potential aSi detectors for DanMAX

	Varex Imaging XRD 4343CT	Varex Imaging XRD 1622 AP	Varex Imaging XRD 1611 CP3
Area [mm^2]	432 x 432	409.6 x 409.6	409.6 x 409.6
Pixel size [µm^2]	150 x 150	200 x 200	100 x 100
Number of pixels	2880 x 2880	2048 x 2048	4096 x 4096
Max frame rate [Hz][14]	15	10	3.75
ADC	16	16	16
Dynamic range [dB]	-	87	>84
Image lag	< 5%	< 6%	< 8%
Used at beamlines (in use or commissioning)	I15-1@DLS, P2.1 and P21@PETRAIII	P2.1@PETRAIII	I15-1@DLS, ID22@ESRF

[12] Personal correspondence w/ Dr. P. Chater at Diamond Light Source

[13] https://www.vareximaging.com

[14] Only the full resolution frame rate is listed here. There are various binning and ROI modes with higher frame rates.

We propose that a large HPAD detector is prioritized and that an aSi be procured if the budget allows for a second area detector. The aSi detector could be a valuable addition at the beamline and may be added as a future upgrade if it is not possible to fit it in the construction project. Review panel suggestion: "We strongly support the choice of the Pilatus and the concept of additionally purchasing a flat panel detector, which will add flexibility and capability as well as ease initial testing/commissioning of the experiments."

4.2. Stage for Sample and Sample Environment

Being able to handle a wide range of sample environments (SE) is a central focus for the beamline and thus, the instrumentation needs to be flexible to accommodate any (reasonable) future request. Six degrees of freedom is in general required to fully align any SE. In many cases two translations, XY, would be sufficient, but in some cases rotations are needed as well. To limit load restrictions the stage should be able to carry at least 100 kg of load, and preferably be able to carry this load even if it is not centered. Except for experiments with highly focused beams; e.g. diamond anvil cells, spatially resolved PXRD or PXRD contrast tomography, etc., the sample will be quite large (>100 µm) and thus the accuracy and repeatability of the positioning is relatively easily achievable. The accuracy shall be better than 5 µm. For (sub)micron precision positioning it is anticipated that a small dedicated stage needs to be installed on top of the coarse alignment stage. Two schemes are commonly used to accomplish this type of positioning; stacked linear and rotation stages or a parallel kinematic system. A note on our use of the terms; accuracy, precision, repeatability and resolution are available in Appendix C.

Stacked linear stages have the significant benefit that the motions are independent and, assuming the stages are mounted orthogonal to each other, the description in a Cartesian coordinate system is trivial. Such systems do, however, also have some drawbacks. The stiffness decreases as more axis are added as the stages themselves can have a significant weight and each stage will have some axial deviation when a force is applied. If rotation stages are implemented, the centre of rotation is fixed by the design of the stage, and it will move if the rotation stage is placed on top of a linear stage. In addition. A minor issue is that each axis will have a motor cable, and when the stack is moving, so will the cables, and thus the cable needs to be managed to avoid breakage.

A hexapod is a parallel kinematic system in which six actuators work in parallel to support the workload. The configuration is very stiff and also compact, thus increasing stability. The conversion from motor movement to Cartesian (laboratory) coordinates is not trivial. Commercial systems are delivered with a controller that handles the conversion. Another advantage of the hexapod is that the centre of rotation is a parameter specified in the software, thus increasing flexibility greatly. Most hexapods do only have one or a few cables, and these are mounted near the base, i.e. cable management is trivial. A drawback to the hexapods is that there is no 360-degree rotation around Y as is commonly implemented on stacked systems. This can, however, be added by installing a rotation stage on the top plate if needed, see section 4.2.1. The maximum travel and rotational ranges are also coupled, i.e. it is not possible to reach the specified maximum range in multiple direction simultaneously. Another issue is that even if the software enables movement along the Cartesian, the motion will always be an approximation based on multiple actuator movements. This means that while high precision sample raster scans are in principle possible, it is anticipated that the hexapod would mainly be used to align the SE. E.g. we predict that a small precision stacked stage would be needed for spatially resolved PXRD and tomographic PXRD experiments.

With regard to load and accuracy (and repeatability), both stacked stages and hexapod can deliver the desired specifications. However, all in all it is foreseen that the hexapod is the advantageous option. Especially the option of defining an off-center rotation point is desirable as the interaction point of the sample and beam can be moved downstream towards the detector for lighter SEs and thus decreasing the SDD enabling data collection to higher Q. The hexapod controller must be compatible with the TANGO[15] control system used at MAX IV to facilitate integration with the general control system. Hexapods are in use at MAX IV, and thus, software exists for some brands already.

The distance from the top plate of the hexapod to the beam needs to be large enough to accommodate bulky SEs. We estimate that up to 300 mm is sufficient. A hole through the top plate is advantageous as it will allow parts of the SE to extend further that 300 mm from the beam. It should be stressed that a large distance between the hexapod surface and the sample position will limit the rotation around X and Z. To alleviate this constraint, we suggest to prepare several spacers that can easily be placed under the hexapod to change the distance from the sample to hexapod distance. The SE will be mounted to a kinematic mount that will be permanently installed at the hexapod, see section 6.2 for more details. This will ensure that various SEs can be installed and will be pre-aligned once the previously used hexapod position has been dialed in. The use of a kinematic mount also allows for an easy description of the mounting point vs. beam position to help users design their bespoke SE.

Table 4 Specifications for four commercially available hexapods. Please note that here Z corresponds to the vertical directions, while XY are in the horizontal plane. This is different from the beamline coordinate system where Y is vertical and Z is along the beam.

	Symétrie[16] BREVA ST		PI[17] H-850.H2A		Aerotech[18] HEX500-350HL		Newport[19] HXP1000-MECA	
	X,Y	Z	X,Y	Z	X,Y	Z	X,Y	Z
Translation / mm	±75	50	±50	±25	±55	±54	±69	±39.5
Rotation / degree	±20	±22	±15	±30	±12	±20	±11	±19.5
Stiffness / N/µm	5	32	7	100	-	-	10	100
Translation speed / mm/s	0.8		0.3		50		9	
Rotation speed / degrees/s	0.25		0.17		10		2.8	
	X, Y, Z		X, Y	Z	X, Y	Z	X,Y	Z
Resolution translation / µm	0.5		0.3	0.2	0.02	0.02	0.1667	0.1667
Repeatability translation / µm	±1		±0.6	±0.2	±0.6	±0.35	±0.15	±0.08
Resolution rotation / µrad	2.5		3	5	0.2	0.2	1.0	1.7
Repeatability rotation / µrad	±5		±3	±9	±1	±1	±0.5	±0.8
Load / kg	200		250		200		450	
Central aperture diameter / mm	120		80		150		200	

The suitable and commercially available hexapods are approximately 350-400 mm high in the middle of their travel ranges, see Table 4. The floor at MAX IV is approximately 1320 mm below the beam

[15] http://www.tango-controls.org
[16] http://www.symetrie.fr/en/home/
[17] https://www.physikinstrumente.com/en/
[18] https://www.aerotech.com
[19] https://www.newport.com

and thus the hexapod will have to be placed on an approximately 600 mm high support. This support should be made from granite to ensure increased stability of the slits and pinhole during operation with highly focused beams. The sides of the support should have numerous anchors for mounting clamps and rails for various auxiliary equipment, e.g. fluorescence detectors[20], microscope cameras and beam stop. A potential design is shown in Figure 9.

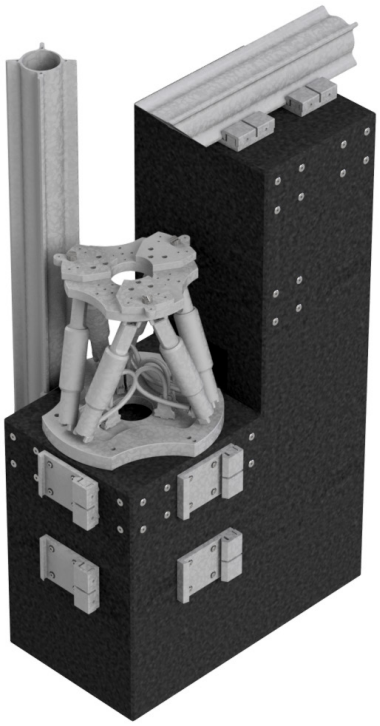

Figure 9 Potential design of a granite base for the hexapod and auxiliary equipment such as slits, ion chamber, pinhole, beam stop, fluorescence detector, etc. The hexapod shown is the H-850.H2A from Physik Instrumente GmbH. The beam direction is from the upper right corner above the X95 rail.

4.1. Detector Positioning

To facilitate the broad range of experiments expected at the beamline, is it essential that the detector positioning system is highly flexible, but at the same time; precise, accurate and stable. On one hand the set-up should be able to position the area detector very close to the sample to maximize the accessible Q range and on the other hand position the detector relatively far away to increase the angular resolution. It should also be able to vary the height of the detector to detect certain desired scattering angles at longer SDD and further increase the accessible Q range at low SDD. Finally, the mechanics should also be able to tilt the detector towards the sample as specifically requested by the user community during the second DanMAX users meeting. This tilt will increase the accessible Q range at low SDD and minimize systematic effects, such as parallax and oblique incidence effects. The stage will be used both for PXRD/TS and for dark field microscopy. The specs given here relates only to PXRD and may be further expanded due to the requirements for the imaging instrument.

[20] An XRF detector was recently funded by the Danish Carlsberg Foundation and will be implemented at DanMAX. PI: H. Birkedal, Aarhus University.

To be able to position the direct beam over the surface of the detector, it is necessary that the detector gantry can move down (-Y) and in-/out-board (±X) by a distance corresponding to at least half the height/width of the largest detector. The largest detector envisioned is the Varex 4343CT with a side length of 432 mm. This means. the -Y and ±X limits must be > 216 mm, assuming a zero point with the beam in the center of the detector. Preferably, the travel range along X should be larger than this to get access to scattering in the horizontal plane at larger SDD. Review panel suggestion: "[Long SSD] is especially useful in connection with off axis placement of the detector. [Horizontal detector translation perpendicular to the beam] is important both for diffraction and DF microscopy".

To facilitate high Q_{max}, the minimum SDD must be as low as possible. This is by no means trivial since the detector gantry must be very stiff to minimize vibrations (that are especially detrimental for imaging) while being strong enough to carry heavy detectors and have the required degrees of freedom. By careful design, it should be possible to enable a minimum SDD of 150 mm or even lower. By positioning the beam on the lower edge of the detector while keeping the normal of the detector surface parallel with the beam (ϕ=0°), this leads to a maximum 2θ angle of 62° (70°) for the PILATUS3 2M (Varex Imaging 4343CT) as shown in Figure 11.

As described above the detector must be able to tilt to increase the maximum scattering angle. The geometry for the tilt is illustrated in Figure 10, and the accessible angular (and Q) range for various SDDs are shown in Figure 11. The rotation axis of the detector tilt does not coincide with the sample position; thus, the tilt is not a proper constant SDD rotation (2θ) around the sample. However, by combining the motions along Y, Z and the tilt, it is possible to emulate this rotation. This operation will not be available initially, but could possibly be developed in the future.

By tilting the detector up to 45 degrees while keeping the SDD (as illustrated in Figure 10) at 150 mm, the maximum 2θ angle is 105° (115°) for the PILATUS3 2M (Varex Imaging 4343CT) corresponding to Q_{max} ~27.5 Å^{-1} (~29.5 Å^{-1}) at 35 keV. The effect is less pronounced when the SDD becomes larger than the detector dimension, but even in this case the angular range can be extended. We propose a tilt of up to 45° to ensure high flexibility.

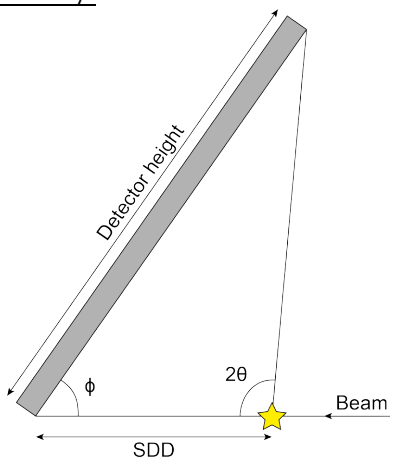

Figure 10 The detector tilt angle, ϕ, used here is the angle between the direct beam and the detector surface in the vertical scattering plane. Note that the SDD is measured from sample to the point where the direct beam hits the detector surface.

The maximum 2θ reachable as a function of SDD for the potential detectors are shown in the left side of Figure 12. The plot on the right shows the angular extent of a pixel at the beam position (2θ = 0°) and at $2\theta_{max}$ (upper edge of the detector). It is clear that while the attainable 2θ range is low at high SSD, the angular extent of a pixel is nearly constant over the detectors. This can be beneficial when studying small changes in, e.g. strain or symmetry changes. The maximum SSD should therefore be at least 1000 mm and preferably larger. **Review panel suggestion: "We recommend that at least 2000 mm is kept as an option for good angular resolution."** The height of the detector should approximately match this value, i.e. the detector should be able to be lifted 1000 mm above the beam.

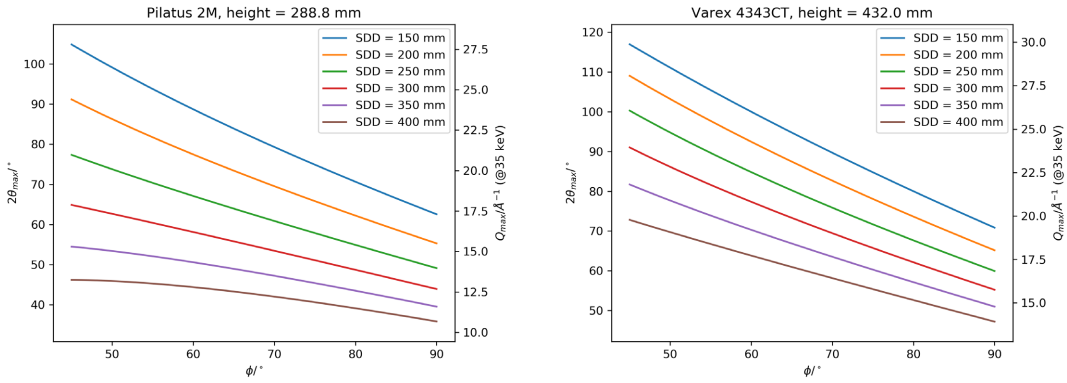

Figure 11 Maximum 2θ angle possible for the PILATUS3 2M (left) and the Varex 4343CT (right) as a function of detector tilt angle and SDD. The corresponding Q_{max} (at 35 keV) is shown on the right side of the graphs.

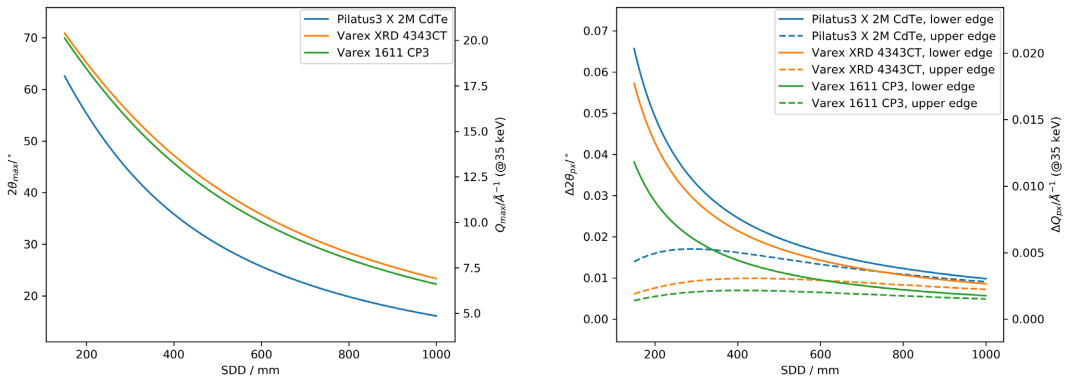

Figure 12 Left: Maximum 2θ angle of the detectors as a function of SDD at ϕ=0°. Right: Effective angular pixel size for the detectors as a function of SDD at ϕ=0°. Full lines are at low 2θ angle (at the direct beam, lower edge of the detector) and dashed lines are at the maximum 2θ angle (upper edge of the detector).

Some of the expected experiments will collect both total scattering data (short SDD) and conventional diffraction data on the same sample. The detector gantry must thus be able to reproducibly move the detector along the beam. To ensure this, it must be equipped with encoders. The standard mode of operation would be to collect data on a SRM at both positions. The absolute position of the detector is thus less important than accurate relative motion, i.e. both absolute and incremental encoders would work. However, an absolute is preferred. The design of the unit will be presented in the DDR for the imaging instrument.

4.2. Additional Instrumentation

4.2.1. Sample Rotation

One of the most basic sample environments, but essential for initial operation of the beamline, is the rotation stage. This stage should support a standard Huber goniometer head and be able to be installed such that it can rotate around either the horizontal (X) or the vertical (Y) axis. In some experiments a fast scanning speed is preferred, while in others, precise positioning is key in, e.g. tomographic experiments. We therefore propose two different rotation stages that potentially share a common interface to the hexapod; one simple direct drive stage for high speed and a standard rotation stage with an encoder for precise positioning. The combination of a goniometer head (e.g. Huber 1005) and goniometer base (e.g. Huber 1413) would be quite light, < 300 g, and the moment on the axle will be less than 0.2 Nm when mounted with a horizontal rotation axis.

The direct drive unit could consist of a standard IUCr goniometer base mounted directly to a stepper motor axle. However, to obtain a smaller sphere of confusion (SOC; see Appendix C) it is preferable to mount the goniometer head through a double ball bearing axle connected to the stepper motor. To dampen the motor vibrations, an inertial damper should be fitted to the motor shaft.

The rotation stage must have continuous 360-degree rotation and be able to withstand the moment, but otherwise the requirements for the rotary stage are less strict. A resolution an order of magnitude smaller than the expected increments should be enough. I.e. if a tomographic experiment requires measurements for every 0.5 degrees, a resolution of 0.05 degrees should be sufficient. In most experiments the increments are 1 degree. The resolution is somewhat tied to the rotation speed. It is preferable that the rotation speed is not too slow, e.g. > 40 °/s. Several stages fulfilling these requirements are available from various vendors.

An important feature of the stages is that the mounting system (or systems) must be flexible enough to mount the stages with the horizontal axis in both horizontal and vertical orientation. Change of orientation must be simple and fast to allow quick installation/adaptation.

4.2.2. Slits

Two sets of monochromatic slits are located in the OH (29.9 and 31.7 m from source) and will be used to define the unfocused beam and the collimated beam. A set of monochromatic slits close to the sample (~0.3 m upstream) will be used as guard slits to clean up any scattering introduced from the upstream components. The beam size at the sample positions will be approximately 1000 µm (FWHM) without focusing and 600 µm (FWHM) when collimating. The optics have been specified to allow for a stability corresponding to a maximal movement of 5% of the image of the undulator source at the sample position. By applying the same 5 %, it can be seen that the requirements for the slits dimension in this case can be quite relaxed, i.e. up to 30 µm.

Whereas the requirements for the unfocused and collimated beam is rather trivial, the requirements are much more stringent for the tightest focus. Using only the transfocator in the OH the smallest focal spots will be approximately 5-10 µm (FWHM) in the vertical direction. This leads to a slit accuracy and repeatability of 0.5 µm. This limit is below many commercial systems that promise 1-2 µm accuracy on the blade positions - and thus worse on the aperture size. In any case the slits must be equipped with absolute encoders on all blades to allow operation in closed loop, which should

increase the accuracy. Working with highly focused beams will require additional pinholes to shape the beam precisely. This is further discussed in section 7.1.

The support should be stiff and highly stable to minimize vibrations with amplitudes on the length scale of 0.5 µm and longer. It should be designed to minimize effects of temperature fluctuations. We therefore recommend a single granite, or synthetic granite, support for both the hexapod and auxiliary equipment as shown in Figure 9. The slits must be easily removable to increase the flexibility of the beamline. It is envisioned that the slits (and intensity monitor, see below) could be installed on an X95 optical rail mounted on the support along the beam axis. This would allow easy installation of the slits and other auxiliary components along the beam axis.

4.2.3. Intensity Monitor

To enable corrections for intensity variations, especially in time resolved experiments during e.g. decay mode operation, the incident intensity on the sample must be accurately recorded and written to either a log or preferably directly to the data frames. Even if the intensity data is not used for normalization, it can be a highly valuable piece of meta data for trouble-shooting beam during experiments.

Two types of detectors could be envisioned, either simple ion chambers or a scattering foil in combination with a scintillation detector. Either of these would work for the desired purpose and thus price will be a determining factor.

4.2.4. Pinhole (Unfocused or Collimated Beam)

When performing total scattering experiments, and many other precise experiments, it is essential to minimize the signal caused by scattering from air. It is therefore advantageous to have an absorbing pinhole as close to the sample as possible. For large (unfocused, collimated, or slightly focused) beams, the simplest solution is a plate made from a heavily absorbing metal with a hole. However, in most cases it cannot be placed very close to the sample.

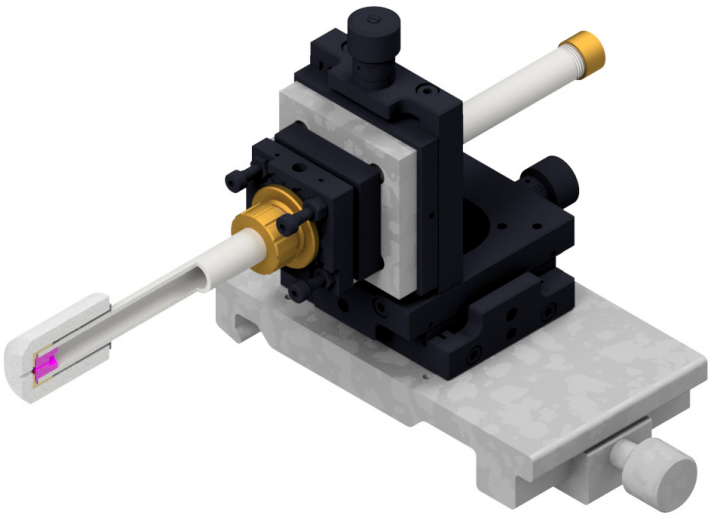

Figure 13 Pinhole setup with manual XYZ + $R_X R_Y$ adjustment. The pinhole is shown in magenta and can easily be changed to different sizes. It is possible to mount a pinhole in the upstream end for extra attenuation of the air scattering if needed. The assembly mounts to the beamline equipment via an X95 rail.

To position the pinhole as close to the sample as possible, it may be advantageous to mount it on the end of a flight tube aligned by at least XY translations, preferably motorized. A simple and versatile design developed at Aarhus University for in situ total scattering experiments is shown in Figure 13. Here the pinhole can easily be exchanged for different sizes depending on the beam size. This design allows for easy translation on a X95 rail and thus the pin hole can easily be placed very close to the sample. The pinhole will be very close to, e.g. heaters, and thus, the end of the flight tube may need to be protected by a heat shield made from a low heat conductivity material, e.g. Macor™. The design will be made once the larger pieces of equipment are known. For highly focused beams, this set-up will not suffice, and a more precise solution must be implemented. This is further discussed in section 7.1.

4.2.1. Beam Stop

To enable efficient use of the beamtime, it is essential to speed up alignment of auxiliary equipment, including beam stops. The beam stops at DanMAX must therefore be motorized in the directions perpendicular to the beam axis. Movement along the beam is preferred, but not essential.

To align the beam stops themselves, and potentially also the samples, in the beam the stops should have a diode incorporated. This feature has been developed for the CoSAXS beamline, and a suitable design is already available. The beam stops at CoSAXS are very small to facilitate data collection at very small Q. However, the design requirements at DanMAX are a lot less strict, and it is anticipated that beam stops of ~2 mm in diameter should be sufficient for most applications. The beam stop will have to be mounted on the inboard side or downstream end of the hexapod support structure. The final design will be completed once the design of the other equipment is known.

4.2.1. Sample Microscope

A high quality sample microscope is necessary for alignment of the samples and to give visual feedback during experiments. The samples at this instrument will vary quite a lot, and thus a microscope with a relatively large zoom range could be very handy. To accommodate bulky, SE the microscope should have a large working distance, e.g. 250 mm, or preferably longer.

In most cases the samples will be relatively large, i.e. >100 µm and thus the field of view (and depth of field; FoV, DoF) should be large enough to align the samples with an accuracy of approximately 10 µm or better. The resolution of the optics will determine the performance as the pixel size of a camera with a pixel resolution of, e.g. 1280x720 with a ~4 mm FoV corresponds to 3 µm and thus better than the required positioning resolution.

4.2.1. Patch Panels

The motor control units are all placed in racks near the control room, outside EH1. To make installation and cable routing easier (and more flexible), patch panels will be installed for each instrument. These patch panels will also have spare connections to connect user supplied equipment. Other patch panels with various common connections (Ethernet, BNC, RS232) will also be available to users.

4.3. Instrument Performance Simulations

The following section presents and discusses simulations based on the original sample location at 46.7 m from the source. The new proposed instrument location has a source to sample distance of only 43.5 m. The divergence of the natural beam is very low, <9 µrad (RMS) in both directions, and

thus the change in beam size between the two locations will be in the order of ~30 µm. This corresponds to a change in beam size of approx. 3% of the natural (unfocused) beam size. Due to this small change in beam size, and the fact that the beam size is adjusted with slits, the change will have a minimal effect for the all the simulations presented below. This can be confirmed in Figure 14 and Figure 15, where simulations of the new instrument location are compared to the original location. Since the changes are negligible, the time-consuming simulations of all parameters have not been repeated with the new instrument location. The flux numbers in section 4.3.2 have been updated to reflect the change in location.

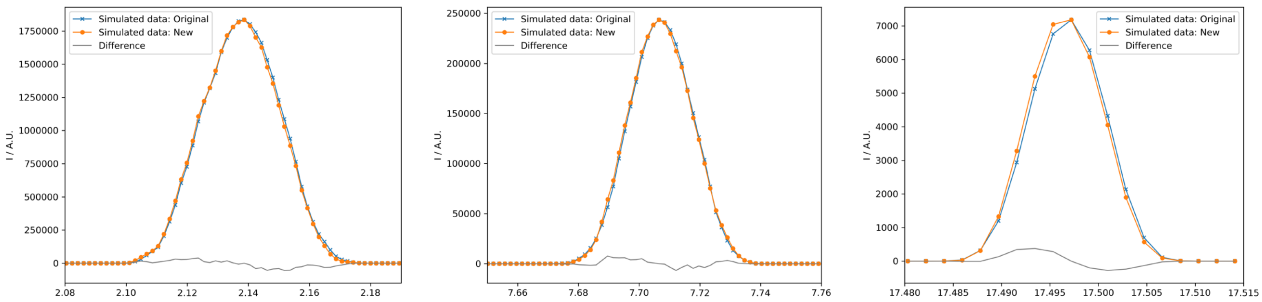

Figure 14 Single peaks from the simulated data at low, medium and high *Q* on the PILATUS3 2M detector. The simulations were performed for an unfocused 35 keV DCM beam on a ⌀200 µm capillary. The orange lines show the simulated data from the new instrument location, while the blue lines show the original. The data has been scaled using the peak height. The grey line shows the difference.

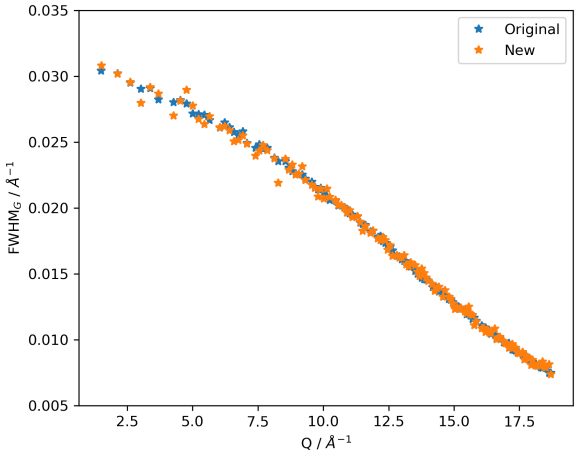

Figure 15 Gaussian FWHM extracted from single peak fits to the simulated data on the PILATUS3 2M detector from the new instrument location in orange and original location in blue. The simulations were performed for an unfocused 35 keV DCM beam on a ⌀200 µm capillary.

The full details of all the original simulations below are described in Appendix B. The simulations have been performed to study the expected performance of the instrument as a function of various parameters. In all cases the final slits before the sample was set at the sample diameter +50 µm. The peak profiles (for the thinnest capillaries, e.g. ≤300 µm, see Appendix C) are nearly Gaussian, however, there are indications of weak "shoulders" and the tails have less intensity than a Gaussian function. This is illustrated in Figure 16 where single peaks are fitted with a Gaussian.

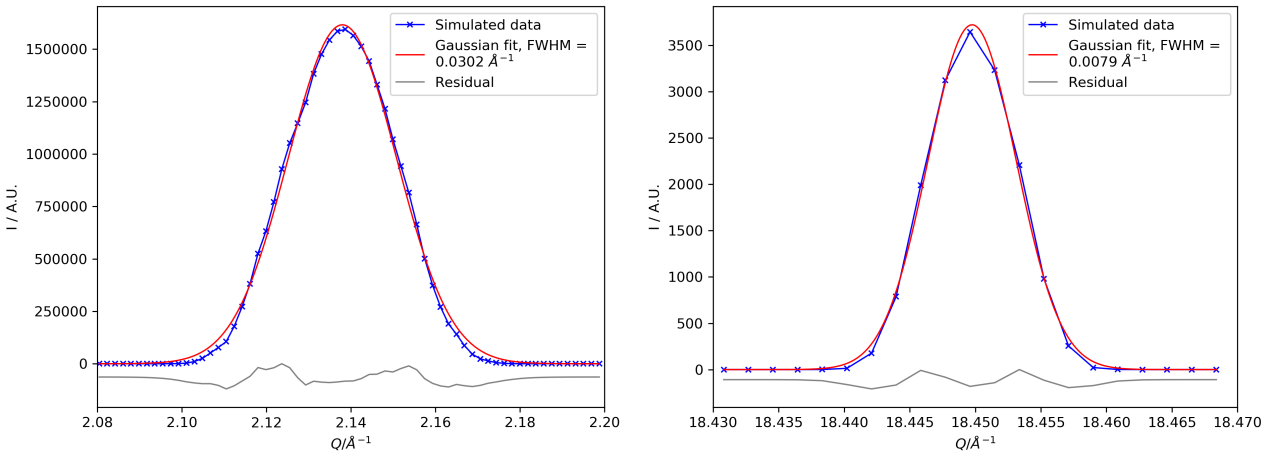

Figure 16: Single peaks fitted with a Gaussian function. Left: Low Q. Right: High Q. The simulation is performed for an unfocused 35 keV DCM beam on a ⌀200 µm capillary recorded on a PILATUS3 2M at 150 mm SDD.

It is not clear what causes the unexpected peak shape. However, it is likely that the source is the sample model used in the simulation. Data recorded on existing synchrotron PXRD instruments are commonly fitted well by a (pseudo-)Voight function with a large Lorentzian contribution (Thompson *et al.*, 1987). We have chosen to fit the simulated data with a Gaussian function to extract the FWHM for the various configurations. Despite the unexpected profile function, we believe that the trends in FWHM for the various configurations do give a rough indication of the instrument performance. The fits were performed using the SciPy library (Jones *et al.*, 2001) in Python (van Rossum & Drake, 2006). An automatic peak search and fitting routine was used and this does unfortunately lead to a few outliers caused primarily by poor segmentation of the data for the large diameter capillaries. The trend in the FWHMs are quite clear, and thus, the outliers have not been removed.

4.3.1. Detector

As described above, three detector models might be feasible for DanMAX: Dectris PILATUS3X 2M CdTe, Varex Imaging XRD1611CP and Varex Imaging XRD4343CT. In addition to different active areas a key difference is also the pixel size. The three detectors have pixel pitches of 172 µm, 100 µm and 150 µm, respectively. The three detectors were simulated with the direct beam intercepting the detector about 10 mm from the lower edge and centered on the detector in the horizontal (X) direction. All other settings were kept identical in the three simulations: ⌀200 µm capillary, 250 µm slits, 35 keV from the DCM, 150 mm SDD and no CRLs. The simulated data and the FWHMs from the three simulations are shown in Figure 17.

Comparing these results to the crude gematrical model shown in Figure 3, it is seen that the trend is similar, and that the resolution at low Q is as expected. The resolution at higher Q is, however, much better than expected. A part of this difference might be caused by the absorption in the sample, which effectively decreases the thickness of the sample. However, the µR value is only 0.12 and thus absorption is quite low.

It is immediately clear that the smaller pixel size of the VI1611 yields a superior angular resolution at low scattering angles, but the advantage diminishes at higher scattering angles. At low angels the angular resolution is normally not a problem due to a low number of reflections for reasonably sized unit cells.

Due to the superior SNR of the HPAD detector we recommend that the primary detector at DanMAX should be the PILATUS3X 2M CdTe, despite the larger pixel size – and thus lower angular resolution at low Q – of this detector. **Review panel suggestion: "We strongly support the choice of the Pilatus and the concept of additionally purchasing a flat panel detector, which will add flexibility and capability as well as ease initial testing/commissioning of the experiments."**

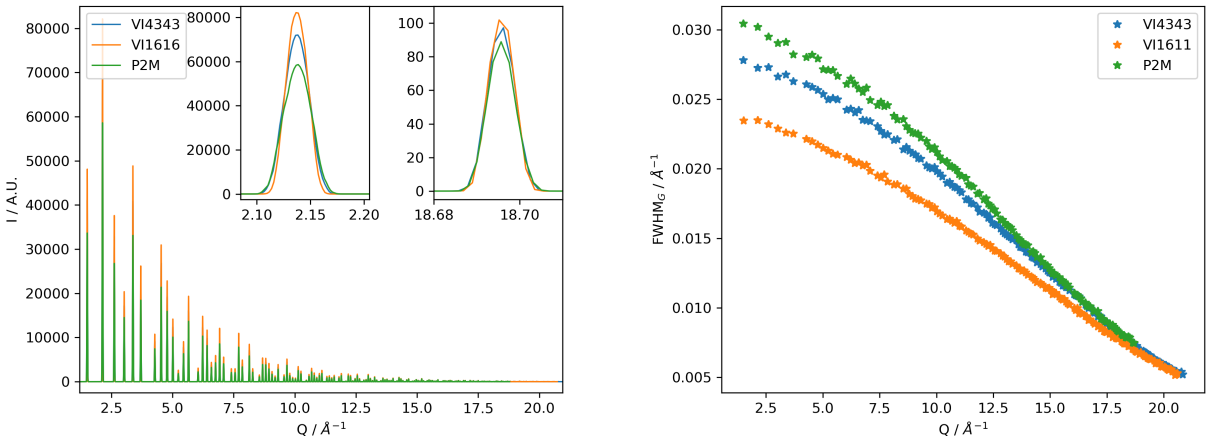

Figure 17 Comparison of simulated LaB_6 PXRD data on three different detector models. Simulation parameters: 35 keV, DCM, ⌀200 µm sample, 150 mm SDD, and no CRLs. Left: Simulated data. Right: Gaussian FWHM extracted from single peak fits.

4.3.2. Photon Energy and Sample to Detector Distance

Two sets of simulations were performed to explore how the angular resolution will improve at larger SDDs and at lower photon energies. The results are shown in Figure 18 and Figure 19. As expected, it is observed that the resolution is markedly improved by lowering the energy/increasing the SDD at the expense of limiting the accessible Q range. A more significant result is the indication that the angular resolution is improved more by increasing the SDD compared to lowering the energy. This suggests that experiments should be run at the highest photon energy possible and the SDD must be adjusted to suit the required resolution. This solution will also minimize systematic errors, e.g. absorption. However, the flux and scattering cross section will naturally be lower at higher energies.

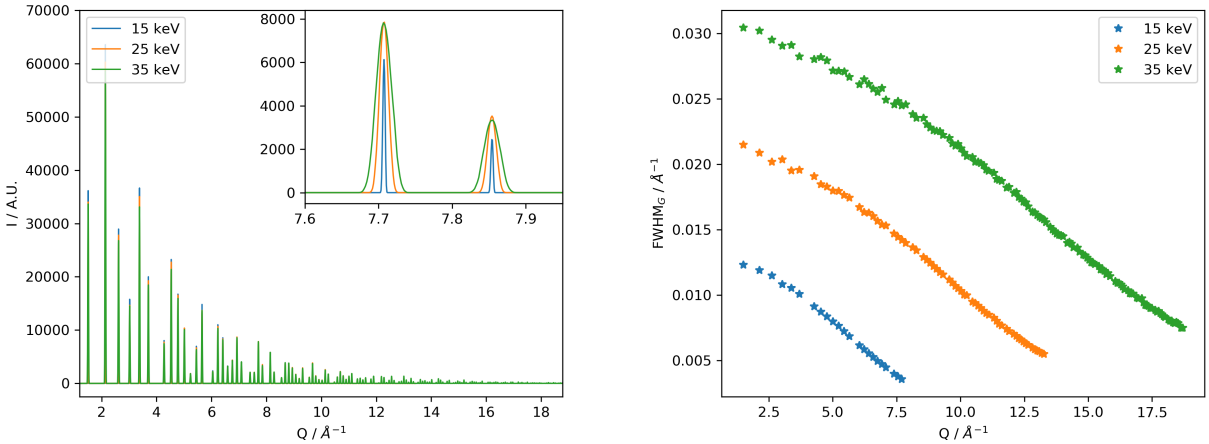

Figure 18 Simulated LaB_6 PXRD data on a PILATUS3 2M detector at three photon energies. Simulation parameters: DCM, ⌀200 µm sample, 150 mm SDD, and no CRLs. Left: Simulated data. Right: Gaussian FWHM extracted from single peak fits.

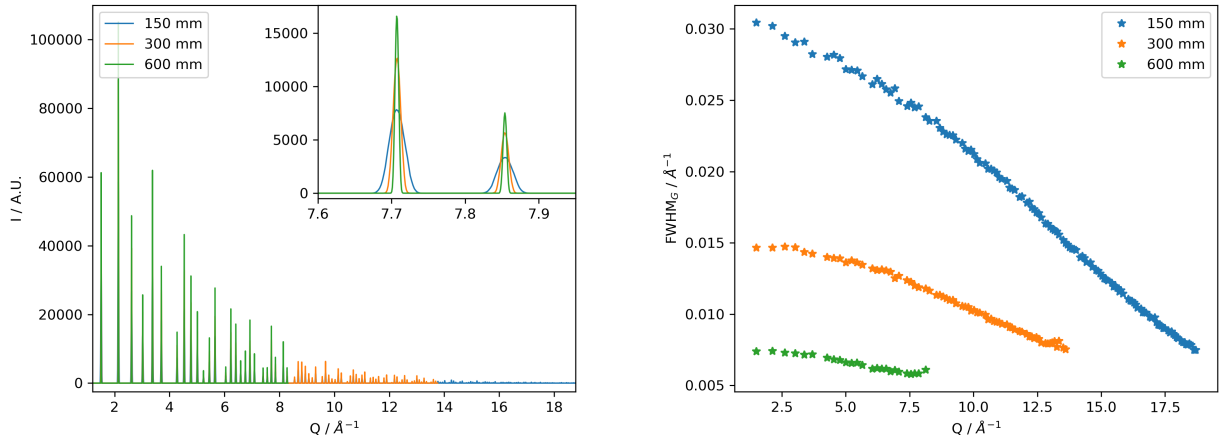

Figure 19 Simulated LaB_6 PXRD data on a PILATUS3 2M detector at three different sample to detector distances (SDD). Simulation parameters: 35 keV, DCM, ø200 µm sample, and no CRLs. Left: Simulated data. Right: Gaussian FWHM extracted from single peak fits.

4.3.1. Capillary Diameter and Sample Geometry

As seen in Figure 3 the sample diameter is one of the main contributions to the peak width. To explore this, a series of capillary diameters from ø100 µm to ø800 µm was simulated. The results are shown in Figure 20. As expected, the angular resolution is improved for the smaller diameter samples. It is also observed that the peaks become asymmetric at high Q as the diameter increases, see Figure 16 (ø200 µm) and Figure 21 (ø800 µm).

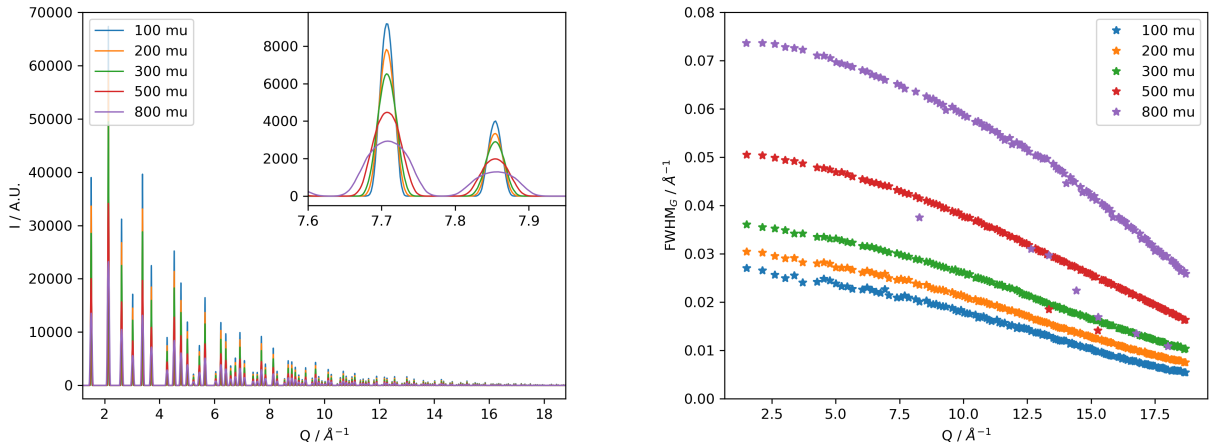

Figure 20 Simulated LaB_6 PXRD data on a PILATUS3 2M detector at various sample diameters. Simulation parameters: 35 keV, DCM, 150 mm SDD, and no CRLs. Left: Simulated data. Right: Gaussian FWHM extracted from single peak fits.

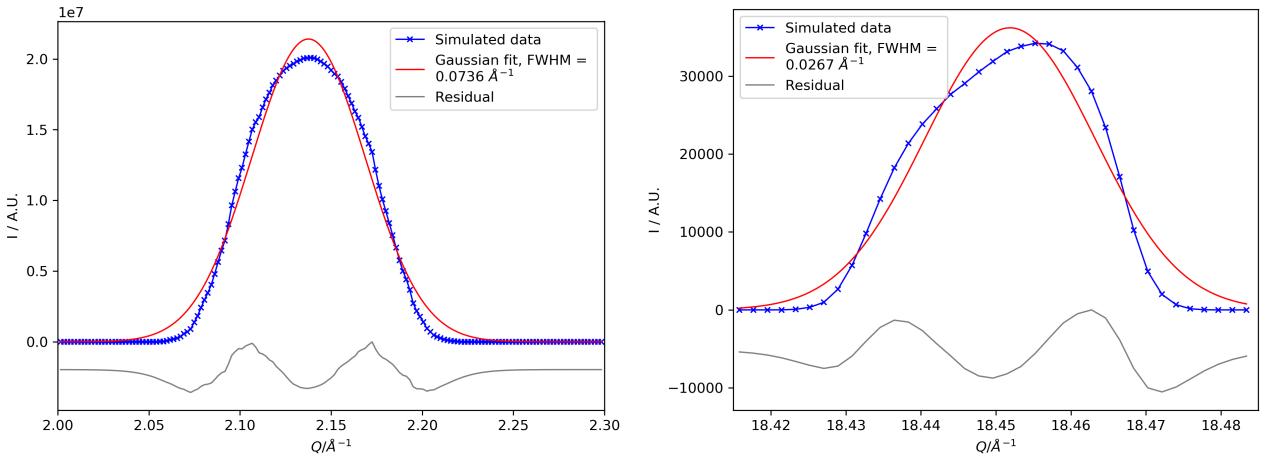

Figure 21 Single peaks fitted with a Gaussian function. Left: Low Q. Right: High Q. The simulation is performed for an unfocused 35 keV DCM beam on a ø800 µm capillary recorded on a PILATUS3 2M at 150 mm SDD.

All the simulations above presume that the sample is cylindrical, i.e. powder packed in a capillary. This will likely be the case for many samples, however, for various in situ sample environments and high throughput experiments the sample will be a plate measured in transmission. Two simulations were performed, one with a ø200 µm cylindrical sample and one with a 200 µm thick plate perpendicular to the incoming beam. In both cases the beam is defined by the slits set to an opening of 250x250 µm^2. The results are shown in Figure 22. The FWHMs are slightly lower for the cylindrical sample and this is presumably caused by the different sample cross sections probed by the beam, i.e. a ø200x250 µm^3 cylinder vs. a 200x250x250 µm^3 box. Nevertheless, it is clear that the performance is only slightly adversely affected by using a plate shaped sample.

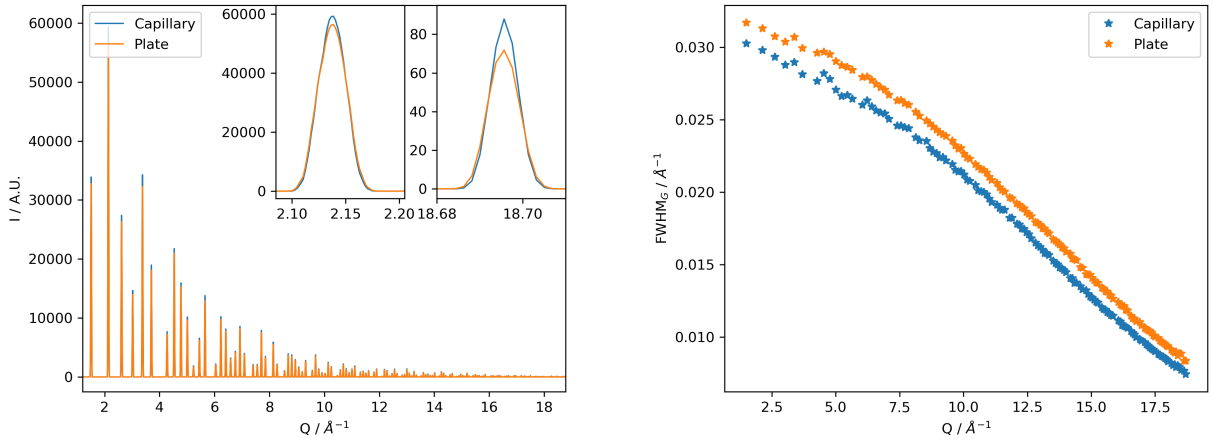

Figure 22 Simulated LaB_6 PXRD data on a PILATUS3 2M detector using two different sample geometries: ø200 µm cylinder/capillary and 200µm thick plate. Simulation parameters: 35 keV, DCM, 150 mm SDD, and collimating with 11 CRLs. Left: Simulated data. Right: Gaussian FWHM extracted from single peak fits.

4.3.2. Focusing

The beamline is designed with CRLs as the focusing element as this provides a fast and easy way of tailoring the beam size (and divergence). Since the focusing distance is quite long (~3/2 demagnification), the divergence is low even when focusing, and thus the resolution is not expected to be very affected. This is confirmed by the simulations as shown in Figure 23. At 35 keV, the natural (0 CRLs, divergence RMS, H: 7.7 µrad, V: 8.3 µrad) beam and collimated beam (11 CRLs, divergence

RMS, H: 1.6 µrad, V: 0.4 µrad) gives nearly identical performances. The beam focused on the sample (24 CRLs, 0 CRLs, divergence RMS, H: 5.2 µrad, V: 4.7 µrad) surprisingly yields slightly better performance at low Q, but slightly worse at the highest Q. This is probably caused by two effects; namely the beam intensity profile and the bandwidth of the photon energy, but not the slightly increased divergence. The energy bandwidth is discussed in more detail in section 5.5.3. The beam profiles of the natural and collimated beams have an almost perfect top-has profile covering the area intersected by the sample. The profile of the focused beam is more intense in the center of the beam.

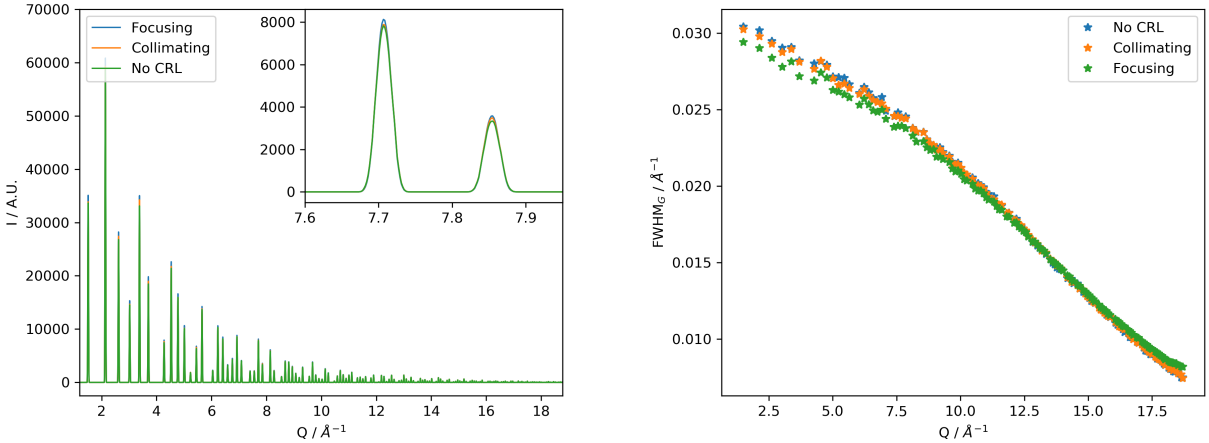

Figure 23 Simulated LaB_6 PXRD data on a PILATUS3 2M detector using three different focusing modes: no focusing, collimation, and focusing to match the sample diameter. Simulation parameters: 35 keV, DCM, ø200 µm sample, and 150 mm SDD. Left: Simulated data. Right: Gaussian FWHM extracted from single peak fits.

The flux through the 250x250 µm^2 slits in the three scenarios (35 keV) are 2.7x10^{11}, 5.1x10^{11}, and 1.4x10^{12} for the natural, collimated and focused beams, respectively[21]. It is therefore anticipated that the data collection time can be reduced by half by collimating the beam without sacrificing any resolution. By focusing on the sample, the flux is increased by more than a factor of 5, with only a slight worsening of the resolution at high Q.

4.3.3. Energy Bandwidth

The main mode of operation for PXRD will be the Si111 DCM monochromator, potentially in parallel with the multilayer monochromator (MLM) for higher harmonic rejection. It is, however, also an option to use the MLM for fast PXRD as the intensity is much higher than what is available from the DCM at the expense of a higher band width. The MLM will have two different multilayer coatings, B_4C/W and $B_4C/Ni_{0.93}/V_{0.07}$,designed to yield two different band widths. The ΔE/E from the B_4C/W coating varies from approximately 5 x 10^{-3} at 15 keV to 9 x 10^{-3} at 35 keV. The $B_4C/Ni_{0.93}/V_{0.07}$ coating yields ΔE/E of approximately 3 x 10^{-3} at 15 keV to 4 x 10^{-3} at 35 keV.

[21] The PXRD simulation are based on the original downstream instrument location. However, the flux number given here has been obtained with the new upstream location.

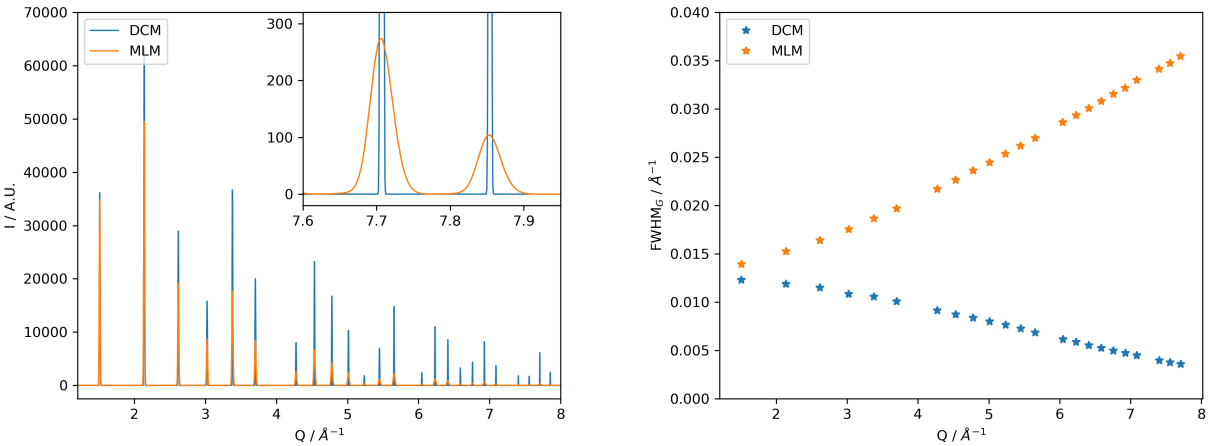

Figure 24 Simulated LaB_6 PXRD data on a PILATUS3 2M detector using the two different monochromators. Simulation parameters: 15 keV, ⌀200 µm sample and 150 mm SDD. The MLM (B_4C/W) beam was focused to match the sample diameter. No CRLs are used for the DCM simulation. Left: Simulated data. Right: Gaussian FWHM extracted from single peak fits.

Using the MLM the large bandwidth, $\Delta E/E \sim 10^{-3}$, quickly becomes the dominant contribution in the peak width and thus the peaks become very broad at moderate Q. This is shown in Figure 24 where the FWHM using the MLM is compared to the expected results using the DCM mode. The simulation was performed for the B_4C/W strip at 15 keV as this is where the flux is maximized, and the reciprocal space is less compressed, i.e. the most realistic user case. Despite peaks being very broad, this may be a useful option to obtain high time resolution.

4.4. Data Collection Strategies and Data Processing

As in situ and operando experiments are a key part of the science to be performed at DanMAX, it is essential that an efficient data pipeline is implemented to give operators (near) instant feedback on their experiments. The initial implementation must be able to acquire the RAW data frame, show the data on the screen and pack the data to a container format, i.e. NeXus/HDF5. It must also save as much meta data as possible to the combined file. These requirements are illustrated in Figure 25. In practice the data and calibration info, including geometry description, will be stored in one NeXus/HDF5 file and the reduced data in a corresponding file. This has the advantage that the raw data file can be protected against changes and can be given, e.g. a DOI for further reference. The user can manipulate the file containing the reduced data.

The raw data can give useful information to the operators, but often it is more useful to see the azimuthally integrated intensity, i.e. I vs. Q, plot. The integration should happen automatically, and the results should be saved in the NeXus file (while keeping the RAW data). It should furthermore save the integrated data in formats ready for various common PXRD refinement programs. This is proposed as 'Upgrade 1' in Figure 25, and is the most important upgrade and one that should preferably be available as early as possible. It is likely that many users will redo the integration with custom detector masks or other settings, but this will nevertheless give a better feedback during the experiment. A collaboration between MAX IV and University of Copenhagen aimed at using FPGA card attached directly to the detector data stream to perform this task is ongoing. However, recent benchmarking suggests that using heavy parallelization on a modern workstation with a high-end

consumer GPU may be sufficient to analyze the images even at the maximum speed of the detector, i.e. 250 Hz for the PILATUS3 X 2M (Kieffer *et al.*, 2018).

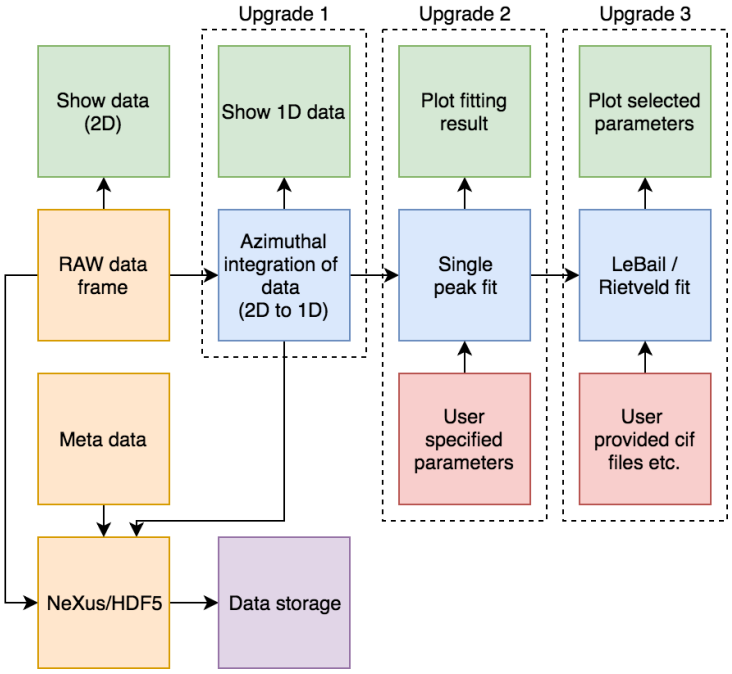

Figure 25 Data processing pipeline for area detector PRXD data. The initial pipeline must show and save the raw data, and preferably pack the data and metadata in a single NeXus/HDF5 file and store the file. The later additions are shown as 'Upgrades 1,2 & 3'.

The next upgrades will include single (multiple) peak fitting to, e.g. follow changes in scattering angle (i.e. unit cell) or phase fraction. The last of the upgrades proposed here would allow for an automatic LeBail (or potentially Rietveld) fit for each new frame. Much of this is already available in the DAWN software package developed by Diamond Light Source (Basham *et al.*, 2015; Filik *et al.*, 2017). However, it is presently not clear whether this software can be directly implemented at the DanMAX/MAX IV data pipeline. Software similar to the one described above is needed at, e.g. the CoSAXS and ForMAX beamlines as well, and thus, we are in discussion with the respective teams and the controls group (KITS) at MAX IV to develop software to be shared between the beamlines.

The internal timing of in situ experiments is very important, especially for fast experiments where a few seconds (or a fraction of a second) will make a large difference. In these cases, it is recommended to use a trigger from either the detector/externally to the SE or from the SE to the detector. In the case of the HPAD detectors both methods should work without issues. In case of the aSi detector it might be beneficial to trigger the detector at a constant rate and use this trigger timing for the SE, see section 4.1.2. It is therefore important that the software (SW) and hardware contain an interface to handle the trigger signals between detectors and SE. To ensure a common time for all meta data, it is proposed to use the local time server at MAX IV.

It may be beneficial to develop specific data widgets for special sample environments where several samples are studied in parallel. Examples are, e.g. battery cells where several cells are tested

electrochemically in parallel, but tested serially by PXRD[22]. In this particular case it would be helpful to immediately show the electrochemical data for a particular cell along with the I vs. Q data, e.g. as a function of time. Another example is for spatially resolved PXRD where a sample is raster scanned through the focused beam. In this case it would be beneficial to immediately show a map of each point scanned and be able to show the I vs. Q data for each pixel in this map.

The basic data pipeline described in the beginning of this section is essential to run the instrument. However, the efficiency of the beamline should improve significantly if the upgrades are implemented. Review panel suggestion: "We recommend that the dataflow includes delivery of data in a choice of standard Rietveld/PDF software data formats to accelerate use of the data". The specific widget for the various sample environments must be implemented in collaboration with the expert user groups performing experiments with the specific SEs.

4.5. Summary

In summary, we propose to build an instrument utilizing a sturdy hexapod placed on a stable granite base to position sample and sample environments in the beam. The diffracted intensities will be recorded on a Dectris PILATUS3 X 2M CdTe detector. This detector will be placed on a stable, but highly flexible gantry (shared with the imaging set-up), allowing for translation in three directions and detector tilt.

[22] A fully equipped AMPIX battery SE has been funded by the Danish Carlsberg Foundation and will be implemented at DanMAX. PI: P. Norby, Technical University of Denmark.

5. High Resolution Instrument, PXRD 1D

One of the primary goals for DanMAX is to be able to measure high quality PXRD data with both high angular resolution and high time resolution. These requirements are coupled as the highest angular/peak resolution possible would warrant a crystal analyzer setup. This would have to be scanned over a certain range depending on the number of channels available. The time resolution for a full diffraction pattern is several minutes and often half an hour or longer in many cases. This time resolution is too low. At the second DanMAX Users Meeting it was decided that DanMAX should *not* have a crystal analyzer setup, nor was it necessary to have an extra axis on the goniometer for a future addition of a crystal analyzer. A modern area detector can provide very good temporal resolution and collect high statistics due to the large active area. However, the attainable maximum Q range while maintaining a high peak resolution, i.e. large SDD, is too limited for many high resolution PXRD applications. The optimal choice therefore seems to be a 1D detector with high angular resolution while maintaining a large angular coverage. As illustrated in Figure 3, this set-up, largely due to its large SDD and small pixels, provides a peak resolution that is superior to an area detector and with higher angular coverage. The read-out time of this type of detector matches that of the area detectors, but as the active area is smaller, the signal to noise ratio will be lower for a fixed exposure time. However, the time resolution is expected to be in the range of only a few seconds to tens of seconds for many routine sample. The instrument including detector and auxiliary equipment is described in detail below.

5.1. Microstrip Detector

Microstrip detectors are based on the same principles as hybrid pixel array detectors and offer high dynamic range with low noise and fast readout. These detectors are described in detail in section 4.1.1. To our knowledge only one microstrip detector system is available commercially, namely the MYTHEN (version 1 and 2) from Dectris, and thus the specifications given below are for these particular detectors.

Both the MYTHEN systems are based on a Si sensor with a thickness of up to 1000 µm. The efficiency is approximately 90% at 15 keV, however, at 35 keV it is significantly reduced to approximately 17%. Various facilities are making developments to use Ge, GaAs and CdTe in these microstrip detectors, however, to our knowledge no commercial solutions are available at this time (Ruat *et al.*, 2018), and it is unlikely that a solution is ready in time for implementation at DanMAX. Since the microstrip detector is a photon counting detectors, it suffers from dead time effects at high count rates, see section 4.1 for further details. The count rate of the MYTEH2 X 1K system is quoted at >10^6 cps/pixel, and the readout time of a module is 89 µs.

The MYTHEN detector is constructed from individual modules with 1280 pixels, each 8 mm wide and 50 µm pitch. By using several modules, it is possible to approximate a cylindrical detector. The SDD will determine the effective angular resolution, and in turn the total angular coverage. A commonly used system utilizing 24 first generation modules with a SDD of 760 mm yields a coverage of ~120° in two theta. The intrinsic resolution is $\Delta\theta_{px} = \tan^{-1} d_{px}/SDD = \tan^{-1} 0.050/760 \sim 0.004°$. However, due to charge sharing the point spread function is approximately 10% larger that the theoretical value (Bergamaschi *et al.*, 2010). It is possible to increase the angular coverage by decreasing the SDD, and in turn sacrificing angular resolution. This, however, defeats the purpose of the high resolution detector, and thus further discussion assumes a SSD of 760 mm. Review panel

suggestion: "[A SDD of 760 mm] …seems adequate and a good compromise between angular resolution and angular coverage."

The origin of the specific SDD value (760 mm) is not known to us, but it is sufficient to get a good number of data points across diffraction peaks from most real samples, while maintaining a large angular coverage for 24 modules. In samples with very narrow peaks, e.g. LaB_6, it may be necessary to sample the peaks with finer detector angle increments than the intrinsic angular pixel-resolution and subsequently merge the data. The goniometer therefore has to be able to move reliably in steps significantly smaller than the 0.004° resolution. A factor of ~10 between angular steps and detector pixels is estimated to be needed.

The deviation from cylindrical geometry is up to 0.7 mm at a SDD of 760 mm, i.e. <0.1% deviation. The experience at the MS beamline at SLS is that this causes small, but significant, parallax effects and non-uniform effective pixel size across individual modules that have to be dealt with in the data reduction. The first-generation modules are delivered without individual protective housings and the Si sensor is exposed. These are normally mounted end to end from either the inboard or the outboard side. The configuration leaves a small blind region of ~0.17° between active surfaces (Bergamaschi *et al.*, 2010, Gozzo *et al.*, 2010). The modules are prone to spurious counts near the ends of the modules which are also susceptible to higher parallax effects and thus these channels are often omitted, effectively increasing the width of the gap. The second generation modules, MYTEH2, are delivered in separate enclosures which are not removable (without voiding the warranty and potentially damaging the module). This feature increases the gap between modules to approximately 0.45°.

Dectris can deliver a MYTHEN 24K system using the first generation modules. However, the frame rate is restricted to about 10 Hz at the highest dynamic range (24 bit). The MYTEH2 X system can deliver a frame rate of 1000 Hz at 24 bit. There is no commercially available 24 K system with the MYTEH2, i.e. the design will have to custom-made. The MYTEH2 read-out electronics, DCS4, can read out 4 modules per unit, thus the design should ideally use 4N modules, where N is an integer. The advantage of a custom-made design is that the weight can be kept lower than the first generation (>100 kg), which will relax the requirements for the goniometer capacity. The conceptual design, shown in Figure 26, weighs approx. 40 kg, thus a total weight below 50 kg should be possible. The modules are designed to work under ambient conditions, but can also work in, e.g. He. However, it might be advantageous to position the modules in air for easy access and add a light He filled (or evacuated) box to avoid attenuation of the diffracted signal. The box would need both entrance and exit windows made from e.g. Kapton™. By making the box removable, it would be possible to have two or more with varying inner radius to match the sample environment in use.

To obtain a full diffraction pattern without gaps, it is normally necessary to collect data with two (or more) detector settings and merge the two (or more) data sets. To reliably merge the data sets, it is essential to have an accurate measure of the detector angle (2θ axis), see section 5.4.1. The goniometer, described in detail in section 5.2, must therefore move the detector between two (or more) angles and return to the position with great precision and accuracy. To ensure a good time resolution, the goniometer should be able to perform the movement rapidly. The movement may be sped up by the fact that the experiment is not sensitive to the actual detector angle, as long as the

angle is known with high precision and is accurate, e.g. it does not matter whether the detector is a 5.0000° or 5.1234°. This means that the settling time or the axis can be significantly reduced.

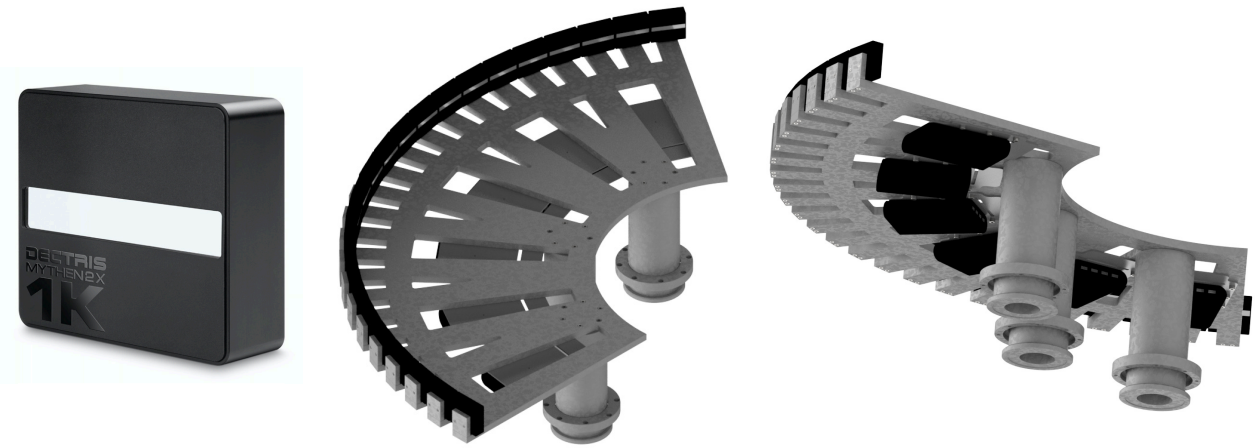

Figure 26 Left: A single Dectris MYTEH2 X 1K module. Middle & right: MYTEH2 24K concept, front wiev (middle) and backside (right) showing the DCS4 readout electronics modules.

In a number of studies, it may be possible to perform the experiment without moving the detector, i.e. accepting gaps in the data and positioning the detector such that no intense peaks coincide with the gaps. Experiments such as this would have high angular coverage, albeit with gaps, but have good time resolution. A MYTEH2 system has been installed at the BL02B2 beamline at Spring8 (Kawaguchi *et al.*, 2017). Here the gaps between the modules are intentionally made larger than in most other systems. Using this approach, it is possible to obtain a high angular coverage with a lower number of modules, i.e. reducing the total cost of the detector system. However, in this set-up it is likely not possible to collect data to high angles using only one detector setting, thus decreasing the time resolution of the experiment. Another MYTHEN system, based on the original version, has recently been installed and commissioned at another SPring8 beamline BL44B2 (Kato *et al.*, 2019). In this system the modules are mounted alternating from the inboard and the outboard sides and overlapping partially in 2θ. In this way data for all 2θ values can be collected in one exposure. However, this type of setup can only be realized with the original MYTHEN detectors, and additionally it must be expected that the effects of axial divergence (see below) is higher as the modules are not cutting the Debye-Scherrer cones in the vertical plane where their angle is minimal.

5.1.1. Aberrations

Due to the lack of angular discrimination the proposed setup is susceptible to a range of aberrations. These aberrations are similar to the 2D instrument, but are more severe due to the high resolution of the detector. The aberrations have been discussed in detail in the literature (Bergamaschi *et al.*, 2010, Gozzo *et al.*, 2010, Du *et al.*, 2016, Kawaguchi *et al.*, 2017), however, a brief and non-exhaustive summary is given here.

Sample size. The Gaussian FWHM from the sample size, or equivalently the capillary diameter, can approximately be expressed as (Gozzo *et al.*, 2010):

$$\mathrm{FWHM}_{\mathrm{cap}} = 2\sqrt{2\ln 2}\ \sigma_{\mathrm{cap}} = 2\sqrt{2\ln 2}\left(\frac{45}{\pi}\right)\left(\frac{d_{\mathrm{cap}}}{SDD}\right) \qquad \text{Eq. 1}$$

Here $d_{\mathrm{cap}}$is the capillary diameter. For a 0.2 mm perfectly, centered capillary this effect amounts to < 10 mdeg. However, with a 0.4 mm capillary it increases to approximately 20 mdeg. For larger capillaries the Gaussian approximation is no longer valid and a better model must be used to describe the peaks, but it is clear that the resolution will largely be determined by the sample diameter.

Linear displacement of sample. If the sample is displaced from the center of the detector, it will cause a nonlinear angular shift of the peaks according to (Gozzo *et al.*, 2010):

$$\Delta 2\theta = \arcsin\left(\frac{d_Z}{SDD}\sin 2\theta_{hkl}\right) - \arcsin\left(\frac{d_Y}{SDD}\cos 2\theta_{hkl}\right) \quad \text{Eq. 2}$$

Note that the notation Δ2θ signifies a shift in angle whereas in Figure 3 it was used for peak broadening. Assuming a displacement of 0.2 mm in both directions this effect leads to deviations of up to 20 mdeg at 120° in 2θ, signifying the need for precise alignment of the rotation center and detector center.

Poor sample centering. In the limit of small wobbling radius, $w < 0.25\ d_{\mathrm{cap}}$ can be reasonably well described as a Gaussian (Gozzo *et al.*, 2010):

$$\sigma_{\mathrm{wob}} = \sqrt{8}\frac{w}{d_{\mathrm{cap}}}\sigma_{\mathrm{cap}} \quad \text{Eq. 3}$$

For larger wobbling radius the peak shape changed and eventually becomes split, thus causing the Gaussian approximation to break down. It is thus highly important to center the sample well.

Axial divergence. In most existing installations there are no receiving slits to minimize asymmetry caused by axial divergence in the low angle range. The asymmetry is negligible for 2θ > 10° and for 2θ < 10° the effect can normally be modeled using the Finger-Cox-Jephcoat function (Finger *et al.*, 1994). The MYTEH2 system was recently installed at the BL02B2 beamline at Spring8. Here a 2.5 mm wide slit was installed to minimize this effect (Kawaguchi *et al.*, 2017). A permanently installed slit such as this installed on all modules will increase the exposure time by approximately a factor of three. If the slit is only mounted on the low angle modules, the exposure time is likely not changed due to the higher signals in this region, but the signals between modules with and without slits will have to be scaled. The design proposed above could easily be adapted to include a receiving slit in the future if it is turns out that a slit is desirable to avoid the axial divergence effects.

The original MYTHEN 24K system is a fully designed and tested unit. It has the advantage that the box is evacuated and thus there is only one Kapton™ window between the sample and the detector surface. Additionally, the gap between modules are narrower than what is possible with the second generation. It is, however, heavy, and thus, it is likely that movement will be slower. The biggest drawback is the frame rate which is a factor of 100 slower than the second generation. The MYTEH2, although requiring some design and engineering will allow us much more freedom in designing the detector setup. We thus recommend a detector constructed using the MYTEH2 X 1K modules. Review panel suggestion: "The Mythen II is lighter and faster and seem to be the better choice in spite of the slightly bigger gaps that are unavoidable even with the Mythen I. We prefer an end-to-end configuration of the panels rather than a staggered configuration, since the end-to-end configuration is tried-and-tested, uses the Debye-Scherrer cone optimally and is simpler."

5.2. Goniometer

The goniometer will have two circles; one for the MYTEH2 detector (2θ, TTH), and one for the sample / sample environment (ω, OM), see Figure 27. It is anticipated that during normal use the MYTEH2 detector will be located above the horizon, but in certain cases it may be advantageous to have it below the horizon, and thus the outer TTH axis must have full 360° rotation. The full rotation will also be needed during detector calibration. The inner OM axis will be used to align sample environments and will not need full 360° rotation. Each of the axis and the goniometer support/alignment is described in detail below.

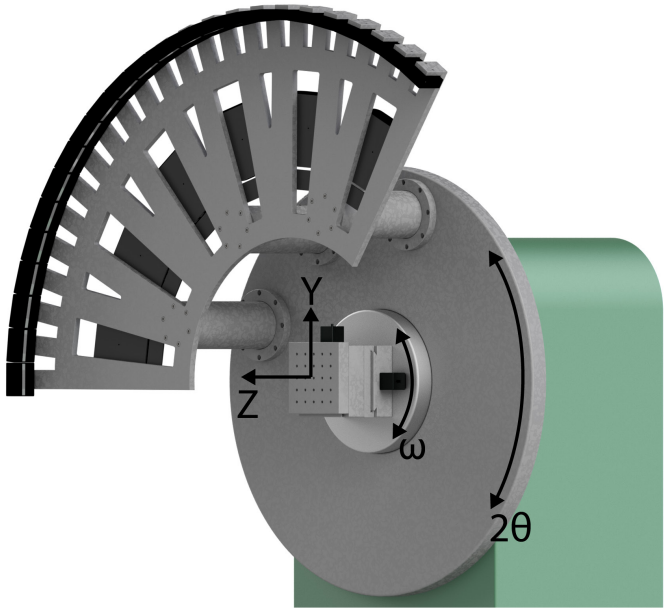

Figure 27 Sketch of the goniometer with indications of the axis. The X-ray beam is along the Z direction.

5.2.1. Two Theta Axis

The TTH axis will position the MYTEH2 detector and must be able to do so with an accuracy significantly better than the pixel size of the detector as described in section 5.1. The angular pixel size is approx. 66 µrad and thus an accuracy of ~7 µrad would be optimal. This is likely too small to be practically obtainable and a more realistic value is likely around 10 µrad. The repeatability must approximately be equal to the accuracy. The mechanical resolution must be smaller than the accuracy, i.e. ~2 µrad. The axis must have full 360° rotation. The SOC shall be smaller than 10 µm.

The distance from the OM axis mounting plate to the beam position (and center of the MYTEH2 detector) should be large enough to accommodate various sample environments. The detector will therefore be mounted on two or three posts. We propose a distance of ~250-300 mm from the OM plate to the beam position. The conceptual MYTEH2 design, Figure 26, weighs around 40 kg. This number will necessarily increase by adding a He filled box. However, it should be possible to design the whole assembly with a mass of less than 50 kg. This is, however, still a significant mass and will have to be balanced with a counterweight, thus, bringing the total load on the TTH axis up to >100 kg. The radial position of the mounting posts will be 350-400 mm, thus a TTH plate radius of ø800-1000 mm is needed. The final dimension will depend on the detailed design of the MYTEH2 assembly, as will the design of the mounting points on the plate. The radial position of the detector center of gravity will be approximately 450 mm from the axis.

As described above, the gaps in the detector (~0.5° wide) require that data is recorded at two or more angular positions. To maximize the time resolution of the instrument, the detector must be able to move between the settings quickly. A realistic speed is approximately 2°/s, which will mean in practice that the delay between the two settings will be about 1 second.

To prevent collisions between the detector and other beamline equipment, the goniometer must be equipped with manually adjustable limit switches.

5.2.2. Omega Axis

The omega axis will be used to hold SEs and samples in the beam. To increase the flexibility, we suggest having an axis which will allow the users to rotate the SE/sample if needed. In normal use an XY stage[23] will be mounted on the axis, and thus, the rotation will be restricted due to the cabling. It is suggested that the cables are routed through the OM axis and thus the main axis must be hollow with a bore wide enough to route the motor cables through, i.e. >50 mm.

Although the angular range is limited when the XY stage is mounted, a wide angular movement could nevertheless be advantageous in other applications and thus full rotational freedom will be evaluated positively in the procurement. If full rotation is not possible, the rotation range should be as large as possible.

The angular accuracy of this axis is much more relaxed that the TTH, and thus an accuracy of 200 µrad is sufficient. The repeatability must be similar to this value. The required SOC for this axis is the same as for TTH; ≤ 10 µm. The combined SOC (TTH and OM) must be smaller than 15 µm.

The diameter of the OM mounting plate is not critical, but is must be large enough to securely mount the XY stage with good reproducibility, i.e. ~⌀300 mm or larger. To facilitate this the plate must be equipped with a precision machined contact points, e.g. three pins that align the equipment. The detailed design of this system will be developed with the vendor. The load capacity of the axis should be high enough to support a range of SE. Thus, we propose a minimum limit of 50 kg.

5.2.3. Goniometer Support and Alignment

The goniometer needs to be aligned such that the goniometer axis (X direction) coincides with the beam (~1320 mm above the floor) and such that the goniometer axis is horizontal and perpendicular to the beam. Additionally, the goniometer should have a translation along the goniometer axis, e.g. to center the MYTEH2 detector in the beam. To perform these motions, the support must have a motorized axis along Y (height) and along X (in-/out-board). The roll and yaw angle of the goniometer must also be adjustable to fully align the goniometer. Review panel suggestion: "We advise that to motorize the roll and yaw for goniometer alignment it is little cost compared to the increase in ease-of-use."

The translations along the X and Y directions must have a travel rage of ±5-10 mm with an absolute accuracy of ~25 µm and a repeatability of < 5 µm. The pitch, roll and yaw of the goniometer should not change more than 25 µrad during movement over the full X and Y ranges. The mechanism must

[23] The stage will have translations in the YZ plan according to the coordinate system shown in Appendix B.

be stiff and not change the sample position more than half of the SOC when a load of 200 kg (sample environment and detector + counter weights) is added.

5.3. Table for Sample Environments

During the 2nd Users Meeting it was also agreed that the instrument must have a table to support various SE and the area detectors available at the beamline. The SE table will be designed around the goniometer. To enable easy access for the sample changing robot, see section 5.7, any SE blocking the access to the sample must be automatically moved away. This can either be performed on a translation stage on which the SE is mounted or by moving the whole table outboard on rails. The latter solution is commonly used and suggested here. By moving the table, it is also possible to move the microstrip detector below the horizon, which can be useful for certain experiments and in particular during calibration etc. The in/out-board movement must be motorized and fitted with encoders. The range of travel should be approximately 500 mm. The positioning of the table does not need to highly precise, but an accuracy of approximately 50-100 µm is preferred. The height of the table must also be motorized and fitted with encoders. The accuracy must be better than the inboard/outboard motion as this axis will be used to align the sample in the beam in some cases. An accuracy of ~10 µm or less is required to position the smallest samples precisely in the beam.

The option to accommodate area detectors on the SE table was discussed at length at the review and the review panel advanced against designing around this option. Review panel suggestion: "We are not fully convinced that the possibilities offered by this 2D detector balance the associated complications. With the new proposed placement of this instrument, the need for using the SE table for such a detector is even less clear as it could be placed at the end of the hutch." Due to the downstream location of the instrument and the possibility to add a detector downstream, we agree with the review panel and propose a simple design to accommodate sample environments only, and not area detectors.

The height of the table with respect to the beam must allow for relatively large sample environments. It is estimated that around 400 mm is sufficient for most SE. The practical travel range of such a table is less that 400 mm in order to increase stability. A travel range of ±50 mm will be sufficient to align the samples / SE in the beam; however, more would be advantageous. To mount smaller SE at the beamline, it is necessary to have different spacers available. The spacers must be stable to not compromise stability significantly. The dimensions of the table surface must be large enough to securely and flexible mount various SE, i.e. dimensions of approximately 0.75 x 0.75 m^2. The table should be centered at the sample position along the beam, see Figure 5. The table surface will have a standard M6 25 mm pitch bread board pattern.

To accommodate various different SEs it is necessary to design the table to carry in excess of 100 kg. The speed of the table is not defined here, but it is advantageous if the inboard/outboard movements are fast (~cm/sec) as the table will likely move in connection with the robotic sample changer, and thus will be a limiting factor for high throughput experiments.

5.4. Additional Instrumentation

5.4.1. Slits, Intensity Monitor & Beam Stop

The requirements for the slits and intensity monitor are more or less identical to the requirements for PXRD 2D, and thus, it is proposed to use two identical units on the two instruments. This will also ensure redundancy in case one unit fails and/or need refurbishment.

The beam stop itself can be identical to the one used at the other instrument. However, due to the geometry the mounting point and the alignment motorized mechanism will be different. The mechanism will likely be mounted on the base of the goniometer with motorized axis along X, Y. The beam stop should also be able to move along Z; however, this could be a manual translation. The final design will be made once the geometry of the remaining items is known.

5.4.2. Pinhole

As for the area detector instrument a pinhole near the sample is needed to decrease the background signal caused by scattering from air. The design proposed in section 4.2.4 could be used here as well, but since the equipment around the sample position at PXRD 1D will likely not change as frequently as for the other instruments. It is therefore possible to design a pinhole that is more rigid, but less flexible. This will have to be designed once the larger equipment is in place.

5.4.3. Temperature control

One of the key sample environments used in high resolution PXRD is high and low temperature. As this environment is often used, we suggest acquiring a dedicated nitrogen heating/cooling setup for this instrument. Ideally, we could implement a system similar/identical to the one used at the SPring8 PXRD beamlines BL02B2 and BL44B2. This system can seamlessly be used from 100 – 1000 K. At the time of writing, it is not known whether this system is commercially available.

5.5. Instrument Performance Simulations

The following section presents and discusses simulations based on the original sample location at 44.8 m from the source. The new proposed instrument location has a source to sample distance of 49.0 m. Due to the low divergence of the natural beam, <9 µrad (RMS) in both directions, the change in beam size between the two locations will be in the order of ~40 µm. This corresponds to a change in beam size of approx. 4% of the natural (unfocused) beam size. Due to this small change in beam size, and the fact that the beam size is adjusted with slits, the change is expected to have a minimal effect for the all simulations presented below. This statement can be confirmed in Figure 28 and Figure 29 where simulations of the new instrument location are compared to the original location. The peak width is slightly narrower with the new location, but overall the changes are minor and thus, the time-consuming simulations of all parameters have not been repeated with the new instrument location. The number of counts in the simulated diffraction patterns at the new location are only 55-60% of the number of counts in the original upstream location. To a high extend this can be alleviated by collimating or slightly focusing the beam.

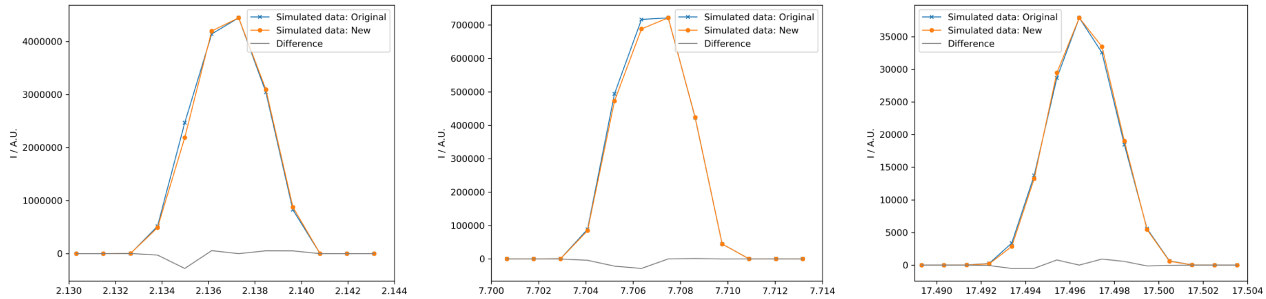

Figure 28 Single peaks from the simulated data at low, medium and high *Q* on the MYTHEN 24 k detector. The orange points and lines show the simulated data from the new instrument location, while the blue shows the original. The data has been scaled using the peak height. The grey line shows the difference. The simulations were performed for an unfocused 35 keV DCM beam on a ⌀200 µm capillary.

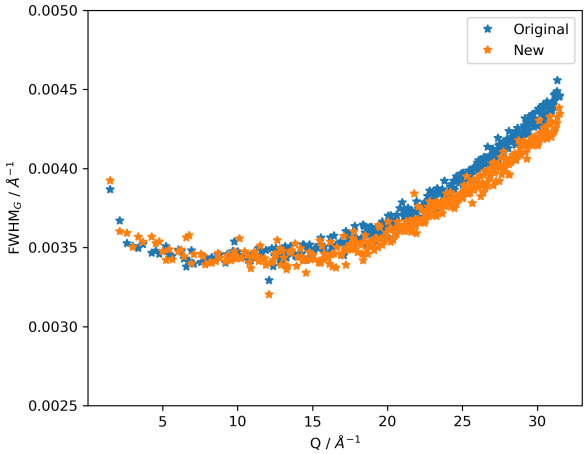

Figure 29 Gaussian FWHM extracted from single peak fits to the simulated data from the MYTHEN 24 k detector. The new instrument location in orange and original location in blue. The simulations were performed for an unfocused 35 keV DCM beam on a ⌀200 µm capillary.

A number of simulations have been performed, see Appendix B, to study the expected performance of the instrument as a function of various parameters. In all cases the final slits before the sample was set at the sample diameter +50 µm. As described above for the simulated area detector data, the peak profiles are not described well by the expected (pseudo-) Voight function. This is particularly the case for capillaries larger that ⌀200 µm, see Figure 30.

It should also be noted that the number of data points for low Q peaks is quite low for very crystalline samples in thin capillaries. E.g. for a ⌀100 µm capillary and 'perfect sample' only two points within FWHM. Thus, it is likely that two or more 2θ settings are necessary to describe the peak well, and this also confirms that the large SDD of 760 mm is preferable to smaller radii detector systems.

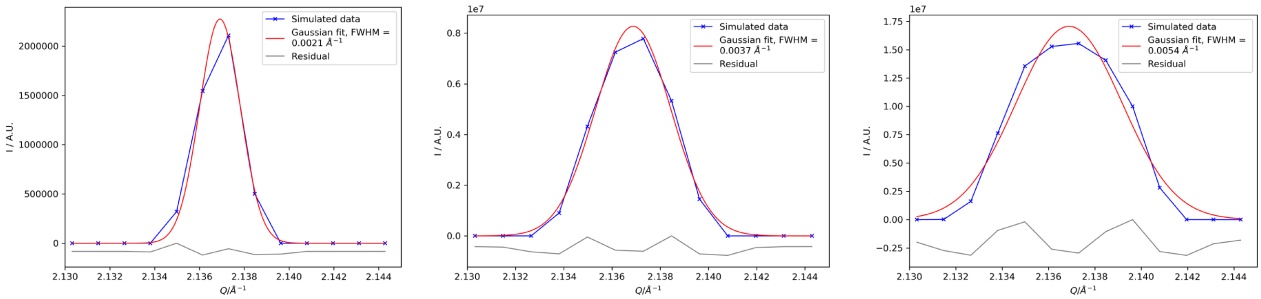

Figure 30 Single peak from simulated for different capillary diameters fitted with a Gaussian function. Left: ø100 µm. Middle: ø200 µm. Right: ø300 µm. The simulations were performed for an unfocused 35 keV DCM beam.

5.5.1. Photon Energy

The only variable parameter for the detector is the 2θ setting, the rest of the geometry is fixed and thus it is only possible to change the peak resolution by adjusting the photon energy. Here three cases are simulated; 15 keV, 25 keV and 35 keV. The peak width in 2θ (i.e. number of data points recorded) for the same peak is nearly equal at the three energies, but the effective width in Q is naturally dependent on the energy as shown in Figure 31.

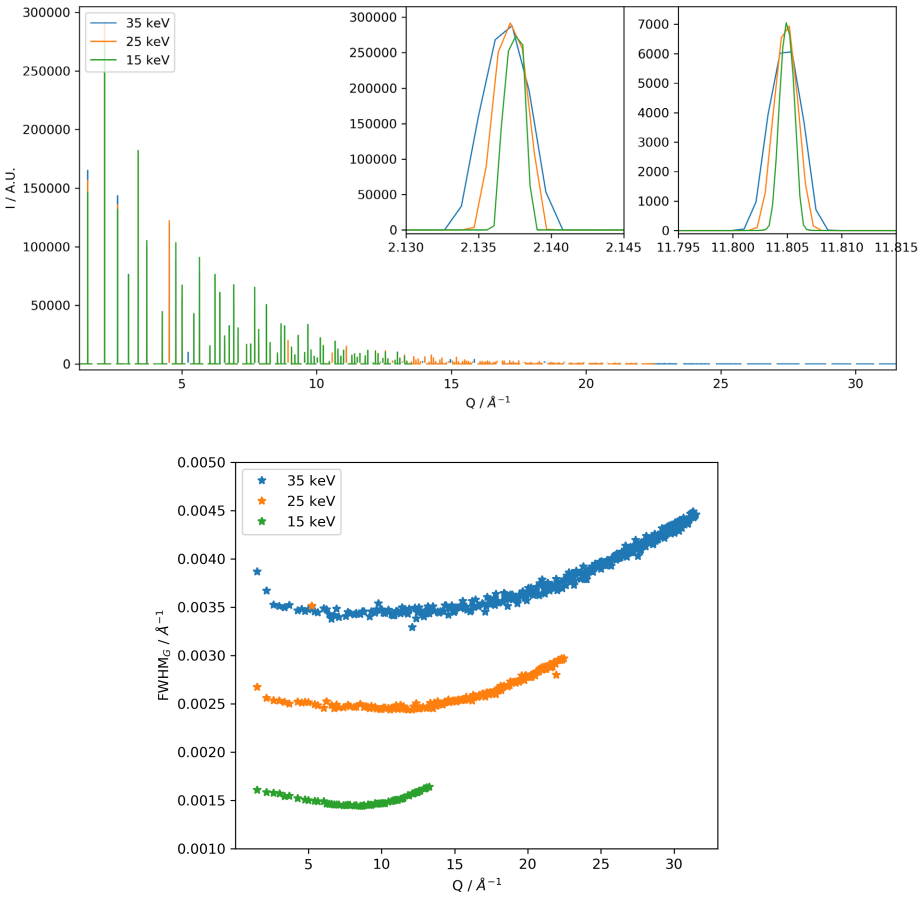

Figure 31 Comparison of simulated LaB_6 PXRD data on the MYTEH2 24k at three different photon energies. Simulation parameters: DCM, ø200 µm sample, and no CRLs. Top: Simulated data. Bottom: Gaussian FWHM extracted from single peak fits.

Interestingly, the peaks are displaced towards higher Q for the lower energies. This effect decreases as a function of Q. An example is shown in the inserts in Figure 31. Absorption will give a peak shift,

but this effect increases up to 2θ = 90° (Sabine *et al.*, 1998), and should be relatively small for the μR values of 1.28, 0.31 and 0.12 for the 15, 25 and 35 keV simulations, respectively. Additionally, no such effect is seen for the larger capillary diameter samples, discussed below, where absorption is a larger effect. Currently, we do not have an explanation for this peak shift.

5.5.2. Capillary Diameter

According to equation 1 above, it is expected that the resolution, i.e. peak FWHM, of the instrument is proportional to the diameter of the sample capillary. A range of sample diameters was simulated to study the effect, see Figure 32.

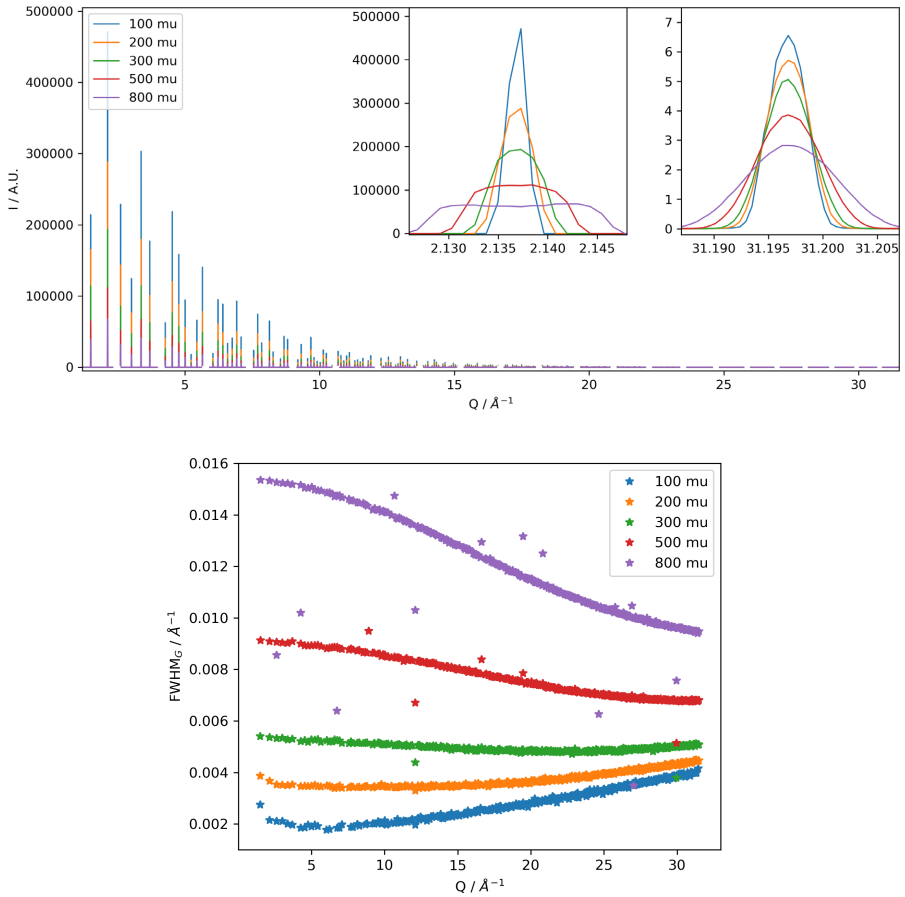

Figure 32 Comparison of simulated LaB_6 PXRD data on the MYTEH2 24k for different capillary diameters. Simulation parameters: 35 keV, DCM, and no CRLs. Top: Simulated data. Bottom: Gaussian FWHM extracted from single peak fits.

In the Q range up to ~12Å^{-1} the ratio of FWHM and capillary thickness is nearly equal and relatively constant for all simulations, except the thinnest sample, ø100 μm. Here the ΔE/E effect starts to dominate at Q ~7 Å^{-1}. Another observation is the peculiar peak shape for the thickest capillaries at low Q where the peaks develop a broad maxima and for the ø800 μm even has a double maxima. This effect decreases at higher Q where the peaks gradually become more Gaussian. It is surprising that the FWHM decreases as a function of Q for the thickest capillaries, as the geometrical contributions to broadening should be largely constant. Part of the effect is probably due to absorption where the effective width of the sample is smaller than the diameter. This will create

larger aberrations at low Q that decrease to a minimum at 2θ = 90°. At higher angles these should increase again. However, this effect is not seen in the simulation.

It is clear that the peak resolution is superior to the area detector instrument even for large diameter samples. However, it is also clear that the full potential of the strip detector is only used for thin capillaries where the peak shape is expected to be 'well behaved'.

5.5.3. Beam Focusing

As seen above for the area detector instrument, a large increase in flux can be obtained by collimating and focusing with little penalty in resolution. The superior resolution of the strip detector is more susceptible to these aberrations and thus simulations were performed to study the effects, see Figure 33.

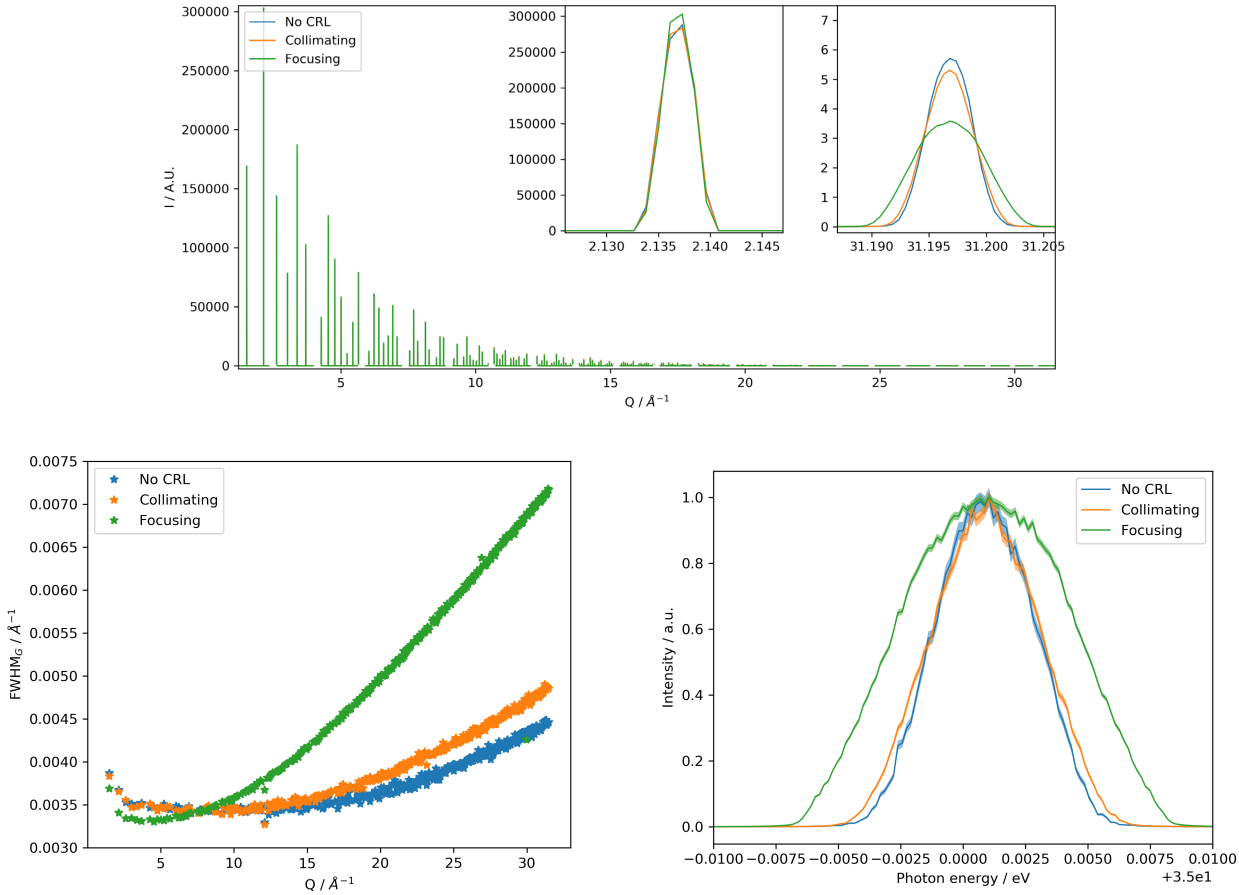

Figure 33 Comparison of simulated LaB_6 PXRD data on the MYTEH2 24k for focusing modes. Simulation parameters: 35 keV, DCM, 0/11/25 CRLs, and ⌀200 µm sample. Top: Simulated data. Bottom left: Gaussian FWHM extracted from single peak fits. Bottom right: Normalized photon energy spectrum at the sample position. The line thickness shows the estimated errors.

It is seen that the natural and collimated beams show nearly similar performance over the full range, with the natural beam having a slightly better resolution at high Q. The difference is quite small and will likely only be significant for highly crystalline samples. The peak width of the focused beam is slightly better below 7.5 $Å^{-1}$ above which it increases more rapidly. This is mainly attributed to the bandwidth of the photon beam, see the lower right of Figure 33. The DCM is in an energy dispersive setting, and thus, a spatial variation of the energy exists in the beam. This way the energy bandpass

is partly defined by the slits (or sample size). By focusing (and collimating) more of the beam, and thus the spatial variations of energy, are transmitted through the slit and a larger bandwidth is observed.

It is expected that collimation can be used with no significant deterioration of resolution. Using a ⌀200 µm sample, the flux increases by a factor of 2.3. By focusing, the flux increases another factor of approx. 3.6. However; this result does come with the penalty of a significantly decreased resolution at high Q.

5.6. Data Collection Strategies and Data Processing

In experiments where large angular coverage and good time resolution are required the research team may decide to accept the small (~0.45°) gaps in the data and record data with only one detector setting. In this mode the detector angle should be chosen such that no intense diffraction peaks coincide with the gaps.

In other experiments the gaps may be unacceptable. Thus, data must be measured at a minimum of two detector angles. By measuring two angles, it is possible to merge the data and obtain a full (gap less) dataset. To merge the data, it is important that that the detector angles are known to a high precision and accuracy of the angle is high, however, the specific angle is not important. This can be used to speed up the experiment since the movement of a motor to an exact position requires time to settle, etc. By decreasing the demand for an exact position and relying on the encoder to read the actual position, it should be possible to increase the time resolution of the experiment.

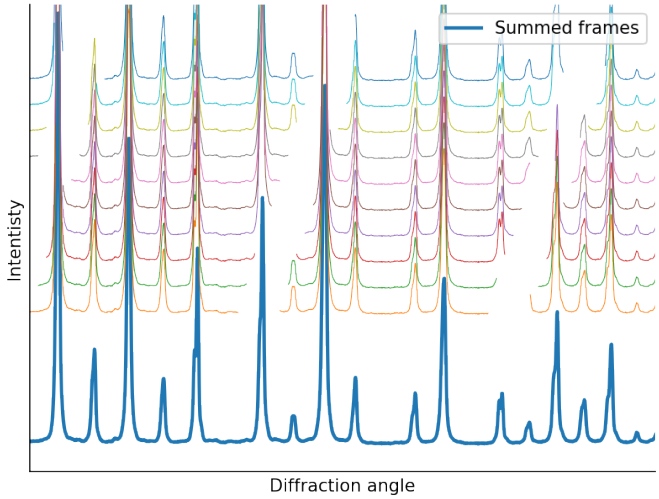

Figure 34 By scanning the MYTEH2 detector continuously while reading out frames at a suitable frame rate, it might be possible to obtain data without gaps. The data shown is not from a MYTEH2 detector, and the gaps shown have been added to the dataset to illustrate the concept.

Another option would be to take this idea further and perform an on-the-fly scan instead of the point-by-point scan described above. In this mode the detector would be scanned continuously (or oscillated) at low angular speed. By reading out the data at the highest frame rates and merging it, it is possible to obtain gapless data. This process is illustrated in Figure 34. The advantage of this method is that the effective time resolution can be varied during the merging process. The method

will necessarily blur the data, but if the intrinsic peak width is high, this might be a good tradeoff for increased speed.

For the ultimate time resolution, it is possible to position the detector such that both positive and negative angles in two theta are covered and the gaps are asymmetrically positioned to cover the two theta angle at once as reported by Katsuya et al. (2016), see Figure 35. In this setting the maximal diffraction angle is roughly reduced by half, and the diffracted signal must be equivalent for scattering above and below the beam. Experience gained at the MS beamline at SLS shows that it is unfortunately not possible to directly combine the region above and below the horizon into one diffraction pattern as the profile parameters are quite different due to the spatial distributions of wavelengths in the beam. At DanMAX we will employ a horizontal DCM which should minimize this problem. However, it is uncertain whether this mode will be useful.

The data processing pipeline for the two PXRD instruments has many of the same necessary features. Thus, there is a large overlap with the pipeline described for the area detector set-up in section 4.4. However, due to the different detector geometry a few specific issues are discussed here. For the 1D detector there is no need for an azimuthal integration. However, a number of corrections to reduce the raw detector data to a useful diffraction pattern is necessary. First the data must be flat-field corrected and bad pixels must be omitted. Then each pixel position must be corrected to diffraction angle and potentially merged with data measured at another 2θ setting. Finally, it is necessary to convert the data to equidistant points in 2θ (or Q) as some programs cannot handle the varying step size. The resulting data should be saved in a range of common data formats ready for use in standard Rietveld/PDF software packages.

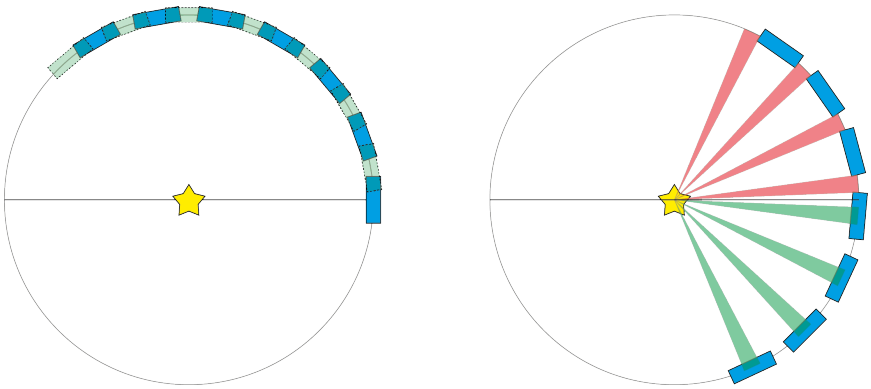

Figure 35 Illustration of the two modes of operation for the microstrip detector, the sample is shown as a yellow star and the individual detector modules are shown in blue. Left: Maximal angular coverage in two settings. The blind regions are recorded in a second exposure with a different detector angle shown in light green. Right: High time resolution. The detector is positioned such that the blind regions are offset in angle and data at the two theta angles are captured at once. The blind regions shown in red have been mirrored through the beam axis.

Each of these steps should be saved in the NeXus/HDF5 file along with the meta data, see Figure 36. In this case it is possible to redo the reduction if something went wrong or a new geometry calibration is performed. Similar to the area detector data pipeline, the raw data and calibration info, including geometry description will be stored in one HDF5 file and the reduced data in a corresponding file. The automatic fitting features described as ‘upgrade 2’ and ‘upgrade 3’ in section 4.4 and Figure 25 should be implemented for this pipeline as well.

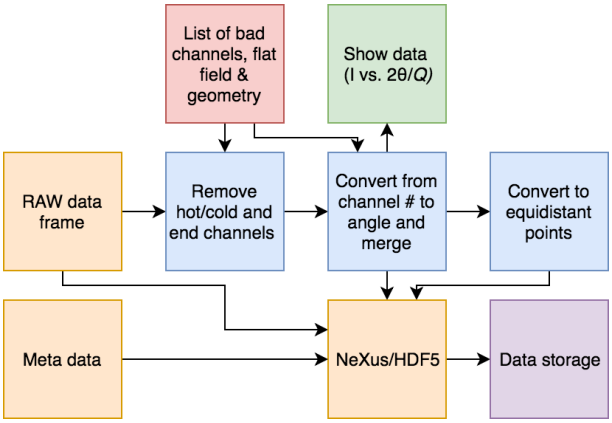

Figure 36 Data processing pipeline for 1D detector PRXD data. The initial pipeline must show the partly reduced data and save the data at several steps along with the metadata in a single NeXus/HDF5 file.

5.7. Robot and Auto Sample Alignment

In many cases the exposure time for an average data set will be much less (seconds to a few minutes) than a manual sample change including alignment and hutch search procedure (several minutes). To ensure an efficient use of the beam, a robotic sample changer will be installed on the high resolution instrument. The sample changer will handle capillary samples mounted in standard magnetic sample holders. The sample will be transferred from a sample tray/grid and placed on a motorized goniometer head equipped with a magnetic base. It will be possible to use non-contact SE with the sample changer, e.g. open flow cryostats or hot air blowers mounted on the breadboard table as described above. The full sample changer scheme is illustrated in Figure 37.

To increase the flexibility and the safety of both users and equipment, we suggest using a collaborative robot as a sample changer. These robots are designed to work in collaboration with people and do not require a safety cage, as in case of collisions the robot simply stops. Depending on the final design of the griper (tool) mounted on the robot it may be necessary to integrate the robot with the PSS system to increase the personal safety even further. It is important that the robot can be reprogrammed easily by the beamline staff, e.g. when a cryostat is moved or an additional detector is added. Some commercially available robots, e.g. from the company Universal Robots[24], have a special teaching mode where the operator can simply move the robot arm by hand along the desired trajectory, i.e. making reconfiguration fast and easy.

The robot must be positioned such that it has a lot of flexibility when reaching the goniometer, i.e. the arm must not be fully extended once at the sample position, as the robot arm would have only one possible trajectory near the goniometer. The final position can only be decided once the detailed design of the goniometer, including SE table and detector, and the imaging stage is known. A possible placement of the robot is shown in Figure 5, assuming a reach of 850 mm. A longer reach may be considered advantageous. However, the price and size of the robots are correlated.

[24] https://www.universal-robots.com/

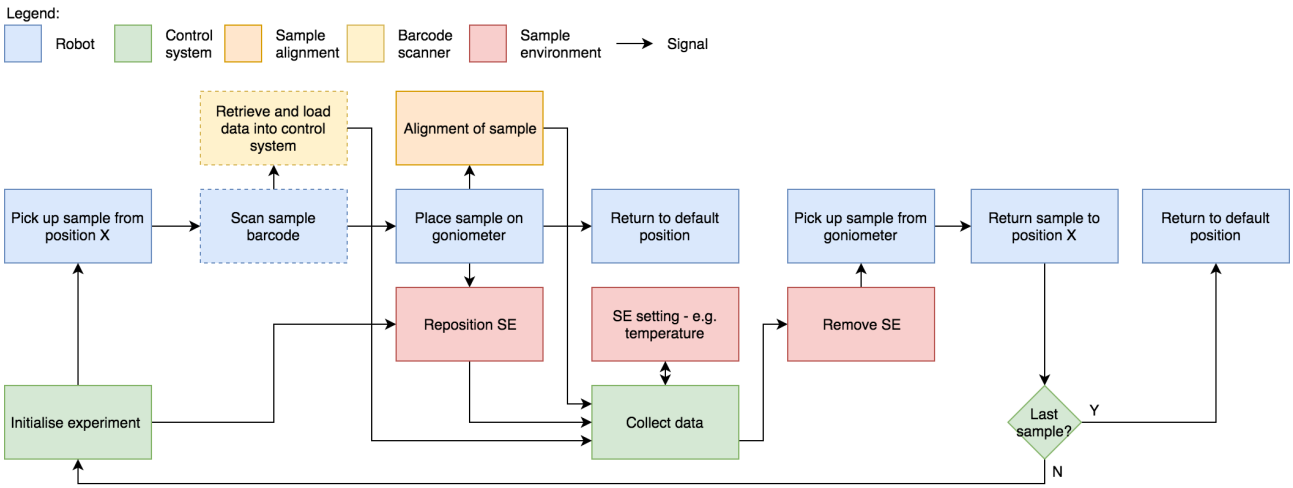

Figure 37 Block diagram for the automatic sample changer. Signals are represented by arrows and all signals to a certain block must be received before a signal is transmitted from the block in question. Safety checks, e.g. no sample at goniometer, are not shown here. The blocks with dashed lines are potential upgrades to facilitate a mail-in program and will not necessarily be implemented initially.

As described in section 5.1, it is very important that the sample is well centered with respect to the detector in order to obtain the highest data quality. This can be ensured in two ways, either pre-aligning the capillaries in self-centering sample holders, or mounting the samples in a simple sample holder and align the sample on the goniometer. Pre-alignment of the samples is obviously a tedious task, especially in the case of high throughput screening experiments. It is also likely that the self-centering mounts will be more expensive that simple magnetic mounts. A significant advantage of this scheme is that the sample spinner itself is very simple.

To align the capillary samples on the goniometer, it is necessary to have a motorized alignment mechanism with at least two translations and two rotations perpendicular to the rotation axis and a high quality microscope camera. The alignment itself will be performed automatically using image analysis according to the algorithm (or similar) illustrated in Figure 38. The samples will be >100 µm in diameter and the alignment should be better than ~10 µm, especially for the thinnest capillaries. This can be implemented such that the system estimates the capillary thickness and adjusts the thresholds relatively to the diameter to ensure that the wobbling/diameter ratio is sensible, see equation 3. The FoV (and DoF) should be large enough to frame the sample once it is positioned on the goniometer head, i.e. a ~2-3 mm FoV is required. The working distance of the microscope should be relatively long, e.g. 300 mm, or preferably longer. The resolution of the optics will determine the performance as the pixel size of a camera with a pixel resolution of, e.g. 1280x720 with a ~2 mm FoV corresponding to 1.6 µm, and thus better than the required positioning resolution. The numerical aperture (NA) of the lens can be relatively small, ~0.05, to ensure a good compromise between resolving power and DoF.

The alignment mechanism must have sufficient range of travel, both on the linear and the rotation axis, to facilitate the alignment. Linear ranges of ±3 mm or more and rotational ranges ±5° or more are required, see section 5.7.1. The mechanism should ideally be equipped with limit switches, or potentially encoders. In either case it is important that the motors allow for fast reproducible movement. The cables will have to be routed through a slip ring to facilitate continuous rotation of the sample during the experiment.

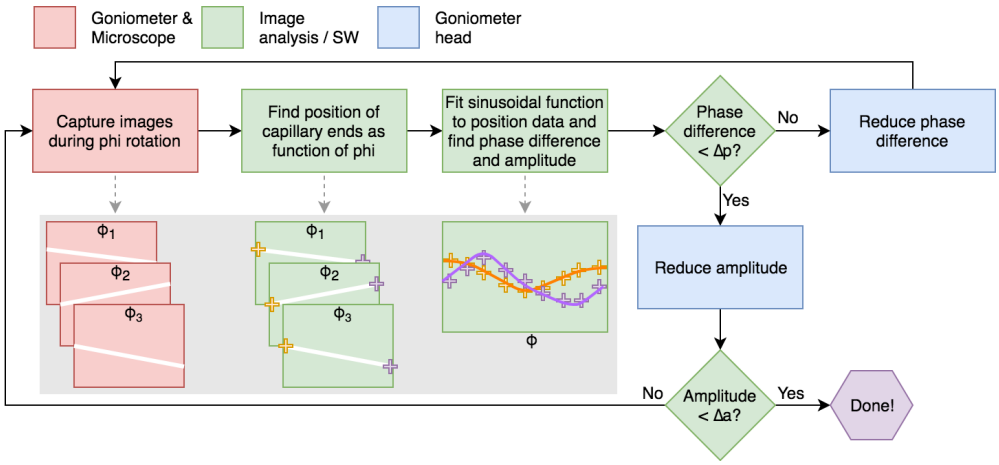

Figure 38 Block diagram for the automatic sample alignment. Δp and Δa are definable thresholds. The maximal number of iterations will be limited, and thus, if the system cannot center the sample properly it will proceed with the next sample. The grey box illustrates the individual steps graphically. The algorithm shown is based on the system at the MS beamline at SLS.

The classic way of aligning the sample is a motorized goniometer head with two linear and two rotational degrees of freedom. This solution is in use at the Powder Diffraction beamline at the Australian Synchrotron[25]. The experience, however, is that the goniometer heads from Huber[26] (when used in a horizontal rotation axis) wear out over a period of 'several months' and thus lead to poor centering. This is partly due to the weight of the goniometer head itself and the materials used. The wear of the goniometer head is necessarily dependent on the torque and thus, the distance from the top of the goniometer head to the sample position is a factor. Similarly, by restricting the use to only capillaries and avoiding any heavier SE the life time may be increased. However, it must be assumed that the goniometer heads must be exchanged/refurbished at least a few times a year. It will, thus, be necessary to have a spare goniometer head available at all times. The team in Australia is designing a sturdier goniometer head, and we are following the development. An alternative is to build a goniometer of an XY stage and a R_xR_y goniometer. This feature has been implemented at the BL02B2 beamline at Spring8. However, we do not know of their experiences with this system, nor the technical specifications. The system is rather bulky, and thus the rotation speed is likely rather low.

An alternative solution could be to use a small hexapod (for a detailed description of these devices see section 4.2). Commercial models with specifications suited for this application are available. The maximum load is approx. 2.5 kg, i.e. this solution will be limited to relatively light SEs. The connection between the hexapod and the controller will also have to be routed through a slip ring. However, available hexapods have many (>60!) connections, and thus a larger slip ring is needed. We are not aware of any PXRD instrument using a hexapod for this purpose. The price of the hexapod implementation would be approximately 10 times higher than the motorized goniometer head. A hexapod with suitable specs, H-811.I2 Physik Instrumente GmbH, is being implemented at the BALDER beamline with promising initial results. This set-up does not include a rotation stage. The implementation into the TANGO control system is nearly ready and is expected to be mature once DanMAX is ready for commissioning. The lifetime of the hexapod for this application is, however, not

[25] http://synchrotron.org.au/aussyncbeamlines/powder-diffraction/technical-information
[26] http://www.xhuber.de/

known, and this option would therefore be a high risk one. In addition, due to the complicated slip ring, it is likely that the spinner frequency would be quite low.

A final, and preferred, solution has been developed and implemented at the MS beamline at SLS. Here the spinner assembly is mounted on a XY stage on the goniometer. The whole spinner can move along the rotation axis. A small XYR_xR_y stage is mounted on the spinner itself and has a range of ±3 mm of translation and ±5° of rotation. The spinner itself is able to spin at speeds of up to 8 Hz. The spinner bearings and the slip ring do wear out over time (~2 years at the MS beamline), however these components can easily be exchanged. A benefit of this solution is that the XY stage at the base can be used for other SEs. A memorandum of understanding about sharing various developments has been signed between PSI and MAX IV. This agreement includes a technical annex about using this design at DanMAX. The PSI solution will be cheaper than the hexapod, but it will be more expensive than the solution with the goniometer head. However, the stability and lower running cost (compared to exchanging goniometer heads) is favoring this solution. Review panel suggestion: "[About the MS spinner] It is a perfectly good option."

5.7.1. Sample Holders

In a future mail in system it is important that the sample holders are cheap and traceable. A system that fulfills this requirement is the SPINE sample holders developed for macromolecular crystallography (Cipriani *et al.*, 2006). The sample holder attaches to a magnetic base and has been developed with robotic sample changers in mind, see Figure 39. The clearance between the magnetic base and sample holder is approximately 50 µm. This is comparable or smaller than the accuracy of the sample robot. However, the 1mm chamfer on the magnetic base will help guide the holder onto the base, see upper left panel in Figure 39. These bases are commercially available at prices below 3€ (without protective vial or transport box) and are delivered with a 2D barcode – a Q-code – and a corresponding human readable code, thus ensuring easy and streamlined sample management. In addition to PXRD the bases can also be used for imaging samples.

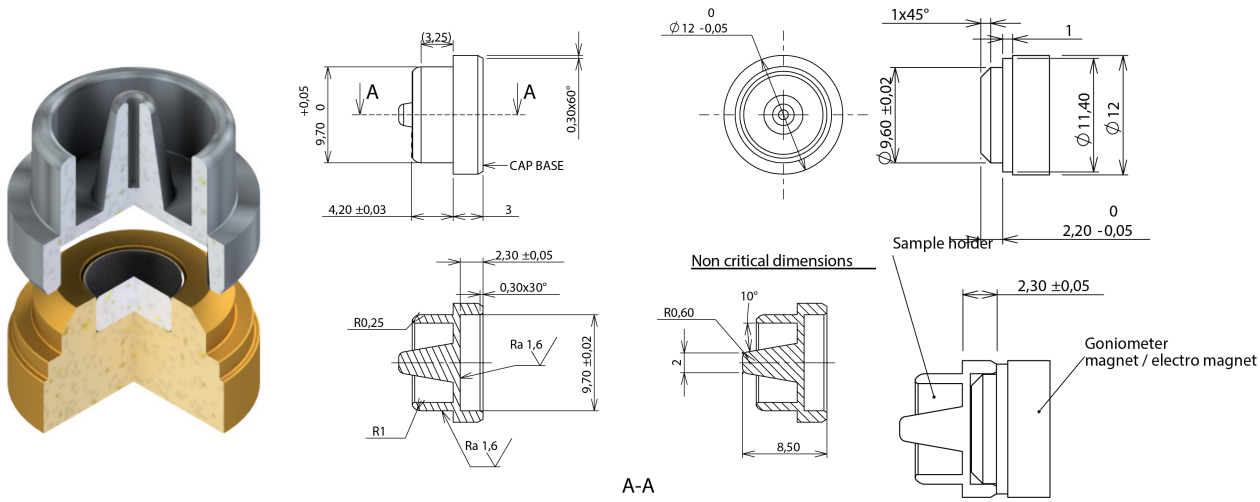

Figure 39 The SPINE sample holder. Left rendering showing a cut through the sample holder. Middle and right: Dimensions of the sample holder and magnetic base adapted from Cipriani *et al.* (2006).

The hole for mounting capillaries in the CrystalCap™ SPINE HT from Hampton Research[27] is 0.7 mm and has a depth of ~4.5 mm. Assuming a perfectly cylindrical 0.1 mm capillary with a 10 µm wall thickness, the worst case mounting error will be 7.3°. Assuming a distance of 25 mm from the top of the base to the beam this leads to a linear offset of ~3 mm. Capillaries with larger diameters will of course give smaller deviations from concentricity. For capillaries larger than 0.6 mm the sample holder will have to be drilled out. This is a simple operation as the existing hole works as a pilot hole. These numbers are worst case scenarios and ranges of ±3 mm and ±5 degrees would be sufficient for all but the worst mounted samples. To aid in the process, a very simple alignment tool can help achieve the alignment of the capillary within acceptable limits, and in addition ensure the correct sample height, see Figure 40.

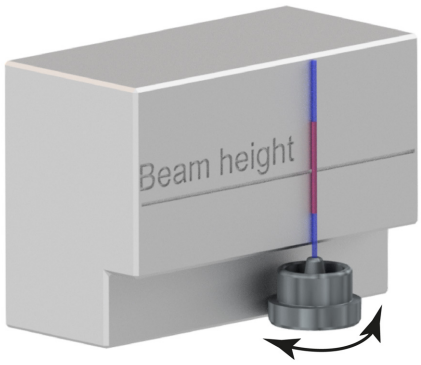

Figure 40 Simple tool for capillary alignment in the SPINE sample holder.

Commercial grippers are available for the SPINE sample holders. However, these are made for retrieving samples from a liquid nitrogen Dewar and may be over-engineered for the task at hand. Instead we propose using a commercial gripper, e.g. the Gripkit-E1 from Weiss Robotics,[28] which has been developed for collaborative robots. The sample tray will be stationary and consists of a grid of cylindrical posts milled from an aluminum plate. The top of each post will be similar to the magnetic base on the goniometer head, albeit with a larger chamfer, and a recessed magnet to hold the sample holder in place. The proposed scheme will allow for high throughput. However, the sample change will nevertheless take some time (~30s) and will be longer than some of the experiments. To speed up the process, we could envision to, e.g. measure data on samples mounted on a grid and raster scan the various positions or use the robot to hold the sample. This solution would avoid some of the sample handling and thus speed up the process. In cases where the sample temperature is changed by an open flow cryostat, this is largely a theoretical discussion as the temperature change will be much slower than the sample change. Any of the measures to speed up the process will have to be studied carefully to ensure that the data quality and reliability do not suffer and to estimate how large the real gain will be.

With a robotic sample changer and a barcode scanner in place the necessary infrastructure for a mail-in service is in place, however, the hardware must be complemented with good software (SW). The SW must move the burden of, e.g. sample registration and tracking from the BL staff to the users. Highly automated systems exist for the MX beamlines, and we will work with the control software

[27] http://hamptonresearch.com/
[28] https://www.weiss-robotics.com/

group at MAX IV, KITS, to investigate whether it is possible to port the database used at BioMAX to be used at DanMAX. The desired workflow is illustrated in Figure 41. In this scheme, the workload of the BL staff is minimal, and the main tasks are to approve the proposals, ship the sample holders, physically place the samples on the sample trays, and dispose of samples after the measurement. The users will pack their samples in capillaries and mount the capillaries in the bases. They must register the compositions, temperatures, wavelengths[29], and the base reference code in the DUO proposal system, along with safety information. Only samples which are recognized (with complete information) based on scanning the barcode will be measured. In the most efficient cases users and BL staff will not be in direct contact and the users will be able to download their data (and reference data on SRMs, e.g. LaB_6 and/or CeO_2) within weeks after submitting their proposal.

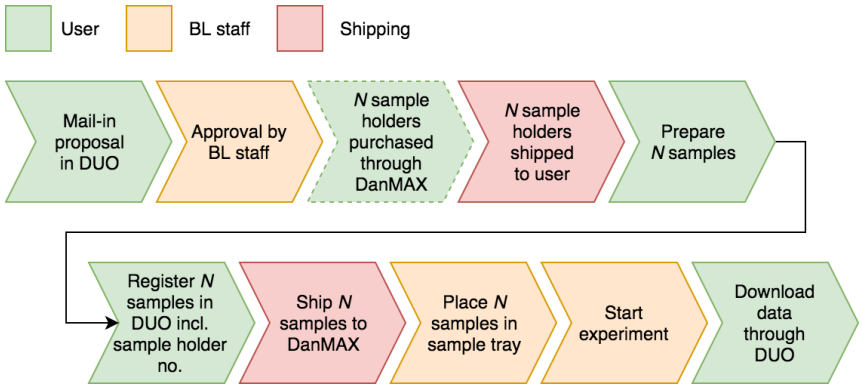

Figure 41 Flow diagram illustrating the envisioned mail-in program at DanMAX.

It should be noted that there, to our best knowledge, are no current plans for a common MAX IV mail in system. Furthermore, there is the concern that the DUO system will not be easily reconfigurable as one of the fundamental decisions is that a shift is 4 hours, and these are allocated to a specific proposal. I.e. running multiple proposals in one shift is currently not possible. It is therefore anticipated that we will have to implement a less automated, and thus more labor intensive, system as a full implementation of the ideas above would require common MAX IV resources.

5.8. Summary

In summary, we propose to build a high resolution instrument around a two circle goniometer, utilizing a 1D detector built from Dectris MYTEH2 1K modules. We propose to construct a detector with a SDD of 760 mm were 24 modules will cover approx. 125 degrees. The goniometer must be able to hold sample environments weighing up to ~50 kg. A motorized table for larger sample environments will be installed in front of the instrument.

Capillary samples will be mounted using the SPINE magnetic caps, commonly used by the MX community. Sample will be aligned using a system developed at the MS beamline at SLS. This will be combined with a robotic sample changer to facilitate high throughput experiments.

[29] It is anticipated that only select energies will be available to ensure that proper reference data can be supplied.

6. Standardized Kinematic Mounts

Kinematic mounts will be used to reliable place detectors, sample environments and samples. The final design of the mounts will be performed once the detector models and the hexapod has been procured.

6.1. Kinematic Mounts for Detectors

To increase flexibility at the beamline a kinematic mounting system, will be available for detectors and cameras, thus allowing easy and reproducible, relocation of detectors to other mounting points at the beamline. If this scheme is adopted by other beamlines at MAX IV, it will be a step to facilitate shared detectors among beamlines in an efficient manner. The realization of a standard detector mount could also be implemented using a standardized hole pattern with, e.g. pins to align the detectors. This implementation would have a smaller height. It would, however, be less precise overall and require greater precision when lowering detectors into position.

The base plates will have three v-shaped groves at 120 degree angles between them in an equilateral triangle. The detector plate will have three balls matching the mounting plate. The base plate will have two sets of fixtures to accommodate both large detector plates for the large detectors, e.g. area detectors and smaller detector plates for the detectors with smaller footprint, e.g. the imaging cameras. This is illustrated in Figure 42. The detector mounting plates will be secured to the base plate using screws. To avoid damaging threads and the kinematic bases, the screws will be knurled to allow tightening them without tools and they will be locked in the mounting plate to avoid exchange to regular screws.

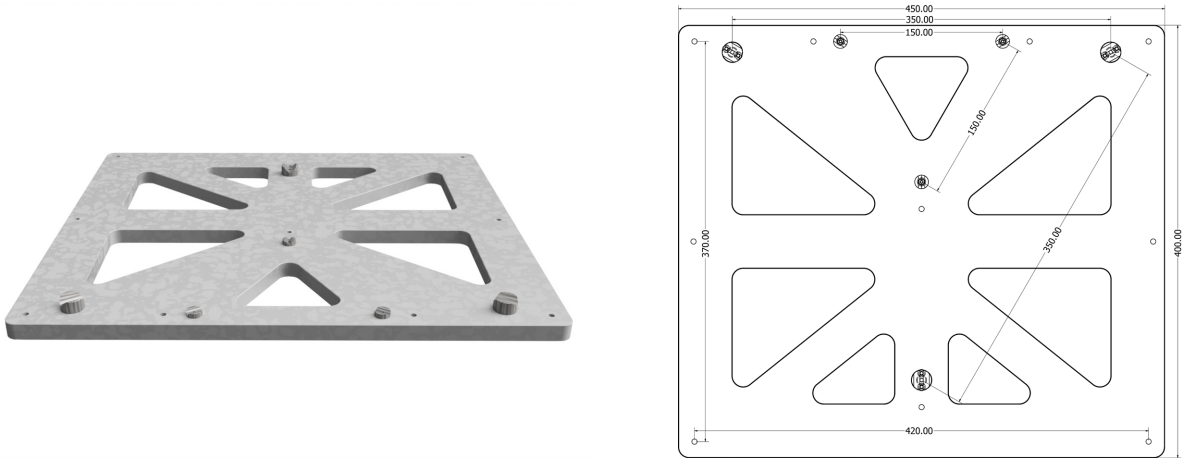

Figure 42 Left: Rendering of the DanMAX detector base plate. Right: Schematic drawing of the base plate (not final dimensions). Holes for mounting the base plate to the support are not shown. For the illustration, the following components were used: V-mount and ball: VB-187-CPM (VB-375-SM), 250-TBR-T (500-TBR-T) from Bal-tec[30]

The kinematic components are available commercially, and the large set can accommodate weights of 100 kg or more. The base plate will be designed to match the size of the largest detector (Dectris PILATUS3 2M). The detector plates themselves will be custom-made and be tailored to each detector model, however, matching the universal layout of the kinematic bases. The large detectors will use ½" (or 12 mm) balls, while the small footprint ones will use ¼" (or 6 mm) balls. We anticipate that a

[30] http://precisionballs.com

detector base plate will be installed on the imaging instrument and on the large detector gantry (section 4.1).

6.2. Kinematic Mounts for Sample Environments

The SE for PXRD can be placed at either the hexapod or on the high resolution instrument. Alignment of the sample position (and SE) with respect to the beam and the area detector is performed with a diffraction standard reference material (SRM). The pitch and yaw angles of the detectors are also refined using the SRM data. This is routinely done and should not cause problems.

The kinematic mount for SEs on the hexapod will be mounted directly to the top circle of the hexapod, see Figure 43. Each SE will be equipped with its own mounting plate fitted with three ½" steel balls (or alternatively 12 mm) mounted in an equilateral triangle arrangement. The plate will be secured by screws into the kinematic bases in a similar way as the detector mounting plates. The mounts themselves are identical to the large detector mounts described above and can support SE with weights up to at least 100 kg. 3D drawings and documentation will be made available on the beamline website[31] for users to implement it in their designs.

Adaptor plates from the mount on the hexapod to smaller commercially available kinematic bases from Newport[32] will be available at the beamline to facilitate smaller SE. These kinematic mounts can also be used at the high resolution setup. The documentation about type and distance to the beam will be made available on the beamline website. A breadboard plate with M6 threads (in a 25 mm pitch pattern) interfacing the kinematic mount on the hexapod will also be available to ensure maximum flexibility.

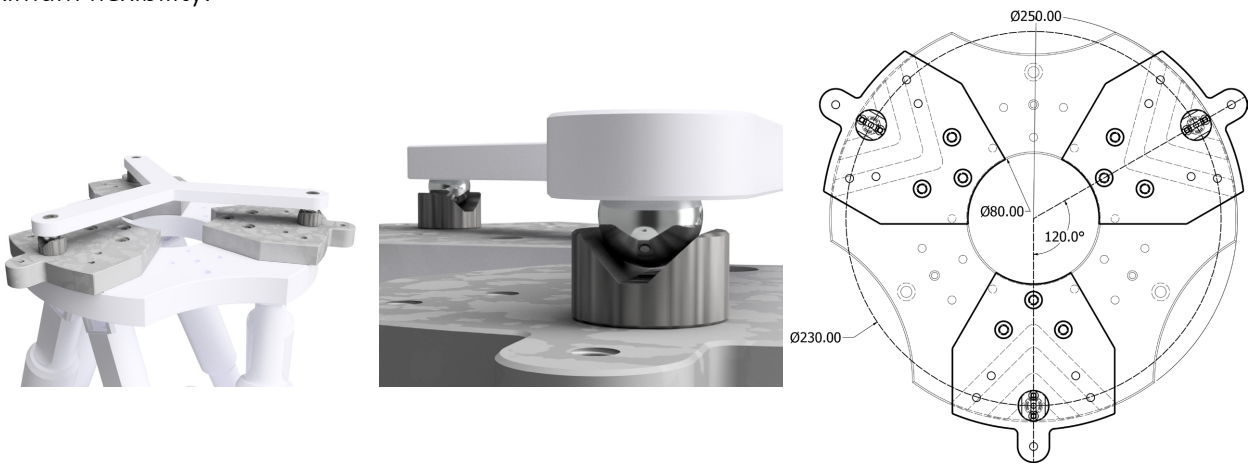

Figure 43 Left and middle: Rendering of the kinematic mount on the hexapod top plate. The hexapod and SE mounting plates are shown in neutral white to distinguish them from the kinematic components. The SE mounting plate does not have holes for securing it to the base plates. Right: Schematic drawing of the mount. The dimensions shown here are not final. For the illustration, the following components were used: Hexapod, H-850.H2A from Physik Instrumente GmbH, V-mount and ball: VB-375-SM, 500-TBR-T from Bal-tec.

[31] https://www.maxiv.lu.se/danmax
[32] www.newport.com

Figure 44 Kinematic bases for smaller sample environments. Left: Newport BK-1A-B, 25.4x25.4 mm^2, magnetic base. Right: Newport M-BKL-4, 88.9 x 101.6 mm^2, with locking thread. Photo credit: www.Newport.com.

If the SE is installed at PXRD 1D, the SE can be mounted on either the table or on the goniometer itself. To obtain data of the highest quality, it is important that the sample is located exactly in the center of detector, see section 5.1. If the sample is not visible, and thus cannot be optically aligned, it will have to be aligned by diffraction. The vertical (along Y) alignment is trivial, but the alignment along the beam (Z) is much more complicated and will likely require an iterative process of 1) translating the SRM sample, 2) collect diffraction data, and 3) subsequent refinement to find the estimated offset using equation 2, see Figure 45. Some SEs, e.g. open flow cryostats, use the capillary spinner on the goniometer for sample alignment and do not require very precise positioning and can be mounted on the breadboard hole pattern in the goniometer table. The SE will be mounted on the goniometer via a vertical face and use the precise pins on the goniometer, see section 5.2.

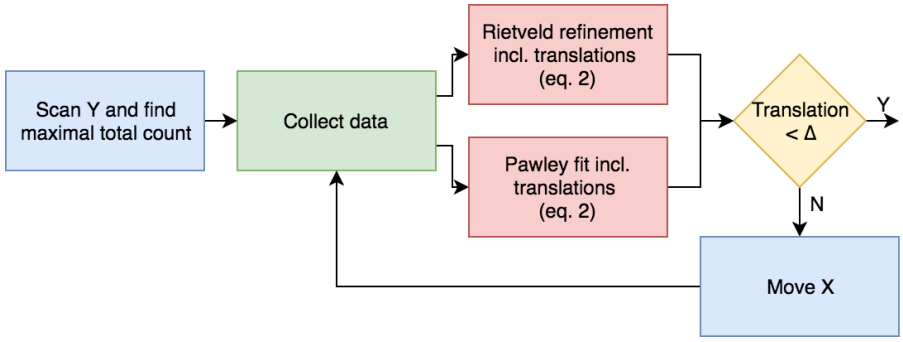

Figure 45 Centering procedure for sample environments at the high resolution instrument when visual alignment is not possible. Δ is a manually definable threshold.

It is anticipated that most SE will be used on the hexapod, and thus no general kinematic mount will be designed for PXRD 1D at this time. If the need for a large standard mount arise, it will be implemented.

This page is intentionally left blank

7. Secondary CRL Focusing

The best focus possible using the transfocator in the OH leads to beam sizes down to approximately 50 x 5 µm (FWHM) at the PXRD 2D sample position (at ~34.8 keV). The spot size is largely determined by the demagnification ratio and is limited due to the relatively large distance from the sample position to the transfocator. For most applications a beam size between the unfocused (~1 mm FWHM) to focused is sufficient. The focused beam size is, however, too large for e.g. high-pressure experiments utilizing diamond anvil cells with small apertures. A more 'circular' beam is also useful for e.g. spatially resolved and tomographic PXRD. It is therefore necessary to examine the performance of a secondary focusing device closer to the sample position in order to obtain a tighter focus.

For high pressure diamond anvil cell (DAC) experiments a 3 x 3 µm (FWHM) beam is desired. For positionally resolved and tomographic PXRD a slightly larger beam (~10 x 10 µm, FWMH) is desired to ensure a good powder average. The tightest focus will only be available for select energies. For DAC experiments a higher energy is preferred to avoid absorption in the diamond and to have access to a larger part of the reciprocal space. Similarly, for tomographic experiments, higher energies are generally preferred to minimize absorption in the sample, and thus the analysis below is performed for 35 keV. To ensure a high 2θ resolution, the divergence should be kept reasonably low, i.e. the focusing device needs to have a long working distance, i.e. Fresnel Zone Plates and Multi-Layer Laue lenses can be excluded. Ideally, the focusing device shall be an in-line component which ensures rapid installation and alignment, thus excluding KB mirrors. CRLs fulfill the requirements and is thus explored further. Since focusing will only be available for select energies and beam sizes, we will use simple lens cassettes and not an actual transfocator unit.

The focal length of CRLs is proportional to the curvature at the apex and inversely proportional to the number of lenses in the cassette. Thus, the design of the lens cassette will be a compromise between the minimal R (and thus minimal number of lenses) and overall transmission, including the geometrical effect of the limited aperture and X-ray absorption. The smallest focus it obtained with the shortest distance between the CRLs and the sample. However, this in turn requires a larger number of lenses.

In all cases the lenses would be mounted on a stage with at least X and Y translations in addition to pitch and yaw rotations to facilitate alignment. A potential solution for alignment is to use a small hexapod. The dark field imaging setup will also use CRLs as an objective, and thus the CRLs should be shared between the two instruments. The final specifications of this unit are not complete at this time, and thus the final location can only be determined once the design of the imaging has been completed. It is estimated that the imaging set-up will use around 70 lenses with a 50 µm apex radius. To focus on the PXRD 2D samples, the CRLs can be positioned on the area detector stage on the imaging instrument. This stage has a long translation along the beam (Z), and thus it will be possible to easily finetune the focal spot size by leveraging this translation.

Several schemes to obtain a tighter focus using 2D CRLs can be imagined as shown in Figure 46. The performance of the focusing schemes are evaluated based on the FWHM of the beam at the sample position and the flux through a 10 x 10 μm^2 and a 3 x 3 μm^2 *square aperture*. The FWHM is obtained by fitting a Gaussian profile to the ray tracing results on a larger monitor. To obtain better statistics,

the data is summed along the vertical direction of the virtual monitor to obtain the horizontal profile, and vice versa. The flux values are compared to the flux through the same apertures for the beam focused at the sample position using the CRLs in the optical hutch only. The gain is calculated as the ratio of the flux for the current simulation and the reference, i.e. OH CRLs only. All simulations have been performed at 35 keV using the DCM only. It should be noted that magnetic phase errors have been neglected, meaning that the flux numbers presented here are likely overestimated by 30-35%.

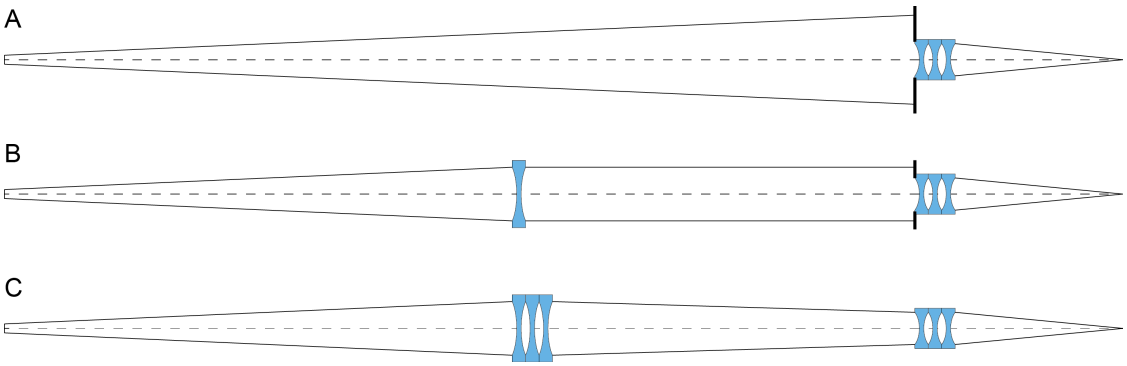

Figure 46 Possible schemes for secondary focusing using CRLs. A: Direct focusing by CRLs in EH1. B: Collimation of the beam using the CRLs in the OH and secondary focusing in EH1. C: Focusing the beam using the CRLs in the OH to match the aperture of the CRLs in EH1.

A comprehensive analysis of the expected performance of secondary focusing using CRLs was performed for the original instrument location. This analysis can be found in Appendix E. The demagnification factor in the new instrument location is higher as the sample is now closer to the CRLs in the optics hutch compared to the original proposal. Some of the main conclusions from the original analysis are assumed to be true with the new instrument location:

- The best gain is obtained for CRLs with a larger radius at the apex. This, however requires an increase number of lenses and is thus not economically viable.
- By comparing two CRL stacks with 50 and 70 lenses, both with R=50µm, it was found the gain was similar or higher using the stack with only 50 lenses.
- The best overall performance was found for scheme C, i.e. focusing with the OH CRLs to better illuminate the CRL aperture in EH1.

Based on these conclusions, we investigated the performance of 50 CRLs with R=50µm using scheme C for the new instrument location.

As shown in Table 5, it is possible to gain a factor of 2 in a 10 x 10 μm^2 aperture, and in practice one may choose to only use the OH CRLs to decrease complexity. For a 3 x 3 μm^2 aperture the gain is close to 8 and is probably worth the extra complexity in the experimental setup. Review panel suggestion: "The options for secondary focusing are very good and a small investment to keep an interesting option."

The gains presented in Table 5 are somewhat lower than in the original simulation (Appendix E). This is to a large extent caused by the higher reference flux facilitated by to the shorter distance from the OH CRL and the sample positions. The actual flux in the 10 x 10 μm^2 and 3 x 3 μm^2 apertures are

approximately 10% lower than in the original position. This is likely caused by how well the OH CLR focus the beam on the EH CRL aperture at 35 keV. By tuning the beam energy slightly, it should be possible to obtain an even higher flux. This has not been attempted in this study.

Table 5 Focusing performance using lenses in either the OH and/or in EH1 at 35 keV. Both cassettes have been translated along the beam in 1 mm increments to find the best position to yield a ~10 x 10 μm^2 (FWHM), a ~3 x 3 μm^2 (FWHM) focus and best possible focus, respectively. The gain is calculated against the focus using only the CRLs in the OH (row no. 2). Bold typeface indicates the values intended for the particular configuration.

Scheme Figure 46	# CRL in OH	# CRL in EH1	EH CRL apex radius [µm]	EH CRL - sample [m]	Focus (FWHM) [µm]		10 x 10 μm^2 aperture		3 x 3 μm^2 aperture	
					Hor.	Ver.	Flux [ph/s]	Gain	Flux [ph/s]	Gain
-	0	0	-	-	798	1135	$4x10^8$	$9x10^{-4}$	$5x10^6$	$1x10^{-4}$
-	40	0	-	-	49.9	9.8	$4.0x10^{11}$	1.00	$3.9x10^{10}$	1.00
C	30	50	50	1.582	15.7	10.0	**$8.1x10^{11}$**	**2.02**	$9.4x10^{10}$	2.43
C	30	50	50	1.534	14.0	2.9	$1.1x10^{12}$	2.83	**$3.0x10^{11}$**	**7.78**
C	30	50	50	1.516	13.6	1.1	$1.1x10^{12}$	2.86	$3.8x10^{11}$	9.88

Since the imaging setup requires 70 lenses in total, we recommended that the CRL objective for the imaging instrument is split into two lens cassettes, one with 50 lenses for focusing of 35 keV radiation and the remaining 20 lenses in another cassette. Detailed simulations for 20 CRLs have not been performed. However, initial calculations show that the cassettes should be useful for focusing a ~23 keV beam in a similar fashion as described above for 35 keV.

The EH CRL unit must be easy to align and reconfigure. Thus, the individual lenses have to be pre-aligned in the two cassettes. Furthermore, the cassettes must be aligned relative to each other when both in use. We are not aware of an existing design that would allow for easy manipulation of the cassettes (except for a dedicated transfocator). The unit does not need to be in vacuum, but could instead be kept under a flow of N_2 or He, which would greatly reduce the complexity. Any design must of course consider the safety aspects of handling Be lenses.

7.1. Pinhole for Focused Beam

Both the 10 x 10 μm^2 (FWHM) and 3 x 3 μm^2 (FWHM) focused beams are not round and show larger widths than height, see Figure 47 and Figure 49. The horizontal direction shows a nearly Gaussian profile with significant tails for both focusing options. To avoid these tails, we suggest installing a pinhole of dimensions matching the desired beam size. A pinhole of ⌀10 µm should be possible to manufacture. However, due to the penetration depth of 35 keV X-rays the pinhole must be made from heavy materials, and even so the aspect ratio will be rather large. This will require very high accuracy in aligning the pinhole axis and the beam. A ⌀3 µm pinhole seems not to be feasible in practice, however, ⌀5 µm seems to be possible (van der Veen *et al.*, 1997).

To have a stable foundation we propose to extend the granite base for the hexapod upstream and increase the height of a section to ~150-200 mm under the beam. This is illustrated in Figure 9. The pinhole support and XY translation would be fitted on this base. The precision requirements are quite strict due to the small beam and a sub-micron positioning capability is needed. This could, e.g. be performed using piezo motors.

The pinhole will need to be quite close to the sample to effectively shape the beam. This is most critical for the smaller focus. In Figure 48 and Figure 50 we show the beam profile for the 3 µm focus with a ⌀5 µm pinhole and the 10 µm focus with a ⌀10 µm pinhole, respectively. Both pinholes are located 20 mm upstream of the sample position.

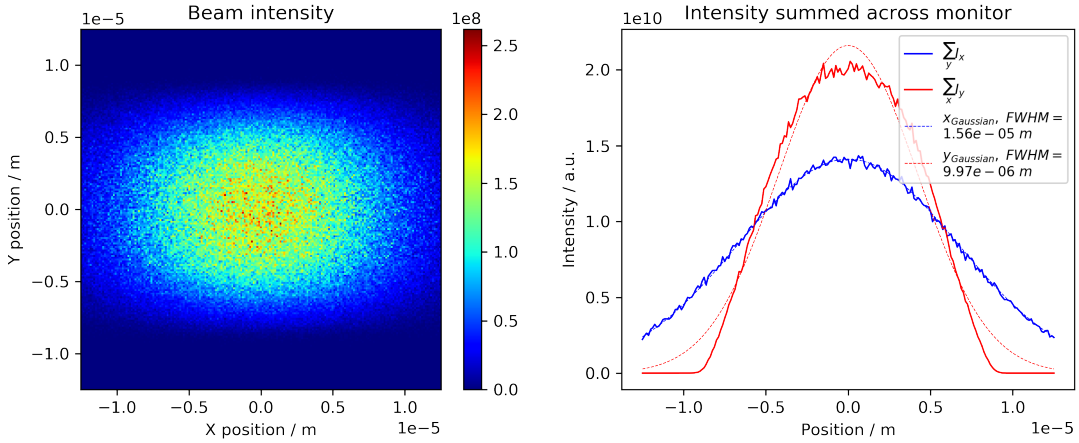

Figure 47 Beam profile at 35 keV using 30 CRLs in the OH, 50 CRLs in the at 1.582 m from the sample position. The total flux in the monitor (25 x 25 µm^2) is 1.8 x 10^{12} ph/s of which 1.1 x 10^{12} are within a rectangle defined by the FWHMs.

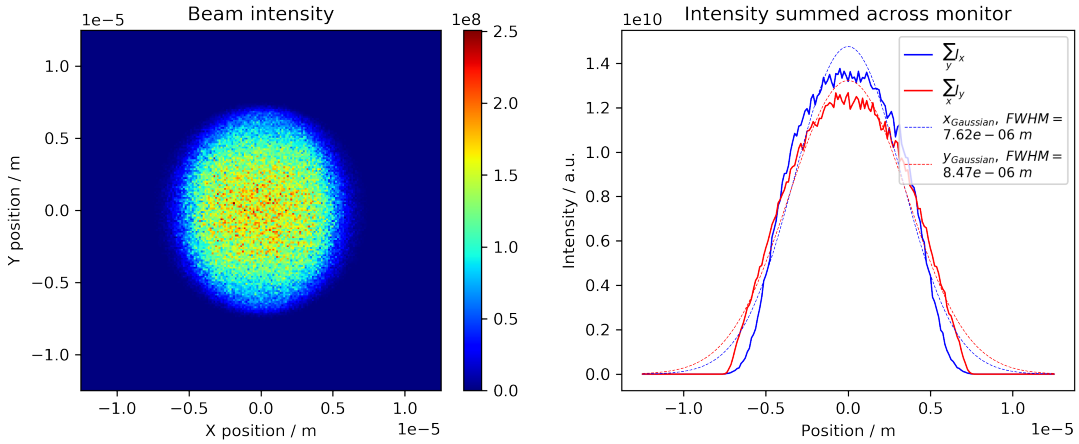

Figure 48 Beam profile at 35 keV using 30 CRLs in the OH, 50 CRLs in the at 1.582 m from the sample position., and a ⌀10 µm pinhole 20 mm upstream of the sample. The total flux in the monitor (25 x 25 µm^2) is 9.2 x 10^{11} ph/s of which 5.6 x 10^{11} are within a rectangle defined by the FWHMs.

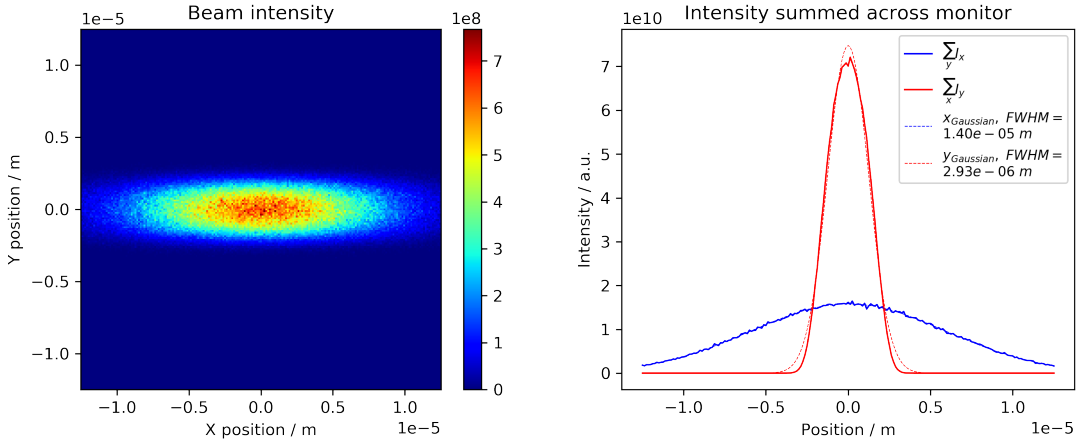

Figure 49 Beam profile at 35 keV using 30 CRLs in the OH, 50 CRLs in the at 1.534 m from the sample position. The total flux in the monitor (25 x 25 μm^2) is 1.8 x 10^{12} ph/s of which 1.1 x 10^{12} are within a rectangle defined by the FWHMs.

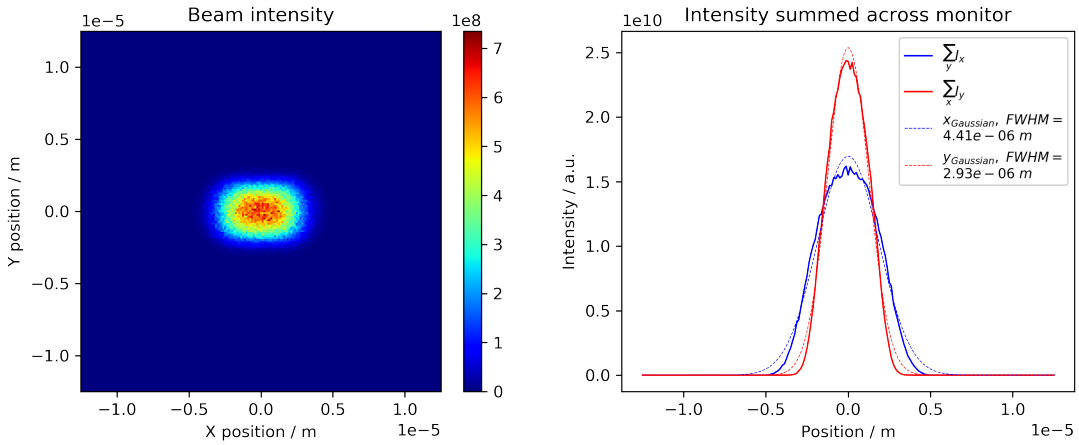

Figure 50 Beam profile at 35 keV using 30 CRLs in the OH, 50 CRLs in the at 1.534 m from the sample position., and a ø10 μm pinhole 20 mm upstream of the sample. The total flux in the monitor (25 x 25 μm^2) is 6.2 x 10^{11} ph/s of which 3.6 x 10^{11} are within a rectangle defined by the FWHMs.

This page is intentionally left blank

8. Gas System

To be adequately equipped to perform the required experiments, we have specified two separate gas rooms at the beamline, one for oxidizing/inert gases (e.g. O_2, CO_2, NO_2, NO, He, N_2, Ar, Kr, Xe, Ne) and one for reducing/toxic gases (e.g. H_2, CHx, NH_3, CO, H_2S[33], SO_2, 3% H_2 in Ar). In total we will be able to store 15-20 bottles in the two rooms. The delivered pressure will depend on the type of gas, but will be around 40 bars for the inert/oxidizing gases and 2-40 for the reducing/toxic gases. Building the gas systems at MAX IV have proven to be very expensive due to the tight but necessary safety regulations (e.g. ATEX classification). We therefore propose to run pipes from all possible bottle positions in the gas rooms through the chicane into EH1. However, we propose to equip only a subset of the bottle positions, e.g. 2-3 in each room, with reduction valves and purge lines, etc. This way we will have a lot of capability early on and can easily upgrade the system when needed. The process ventilation system in EH1 will be fully equipped from day 1 with point extraction at all three experimental stations.

We also propose to keep the initial mixing system simple and add capability (and complexity) when needed. The initial system, an in-kind delivery from Aarhus University[34], will be able to mix two gases and purge with vacuum. This simple system must be interfaced to the beamline control software. Future upgrades to the system would be the addition of more gases to be mixed automatically and the addition of mass flow controllers for a large selection of gases. These must also be interfaced to the control software such that flow and type of gas can be recorded in the meta data.

[33] Sulfur containing gases might have to be placed in a smaller ventilated cabinet inside EH1.

[34] The system will be developed by Prof. Torben Jensen's group at the Department of Chemistry, Aarhus University.

This page is intentionally left blank

9. Installation Considerations

As a number of beamlines at MAX IV are constructed and commissioned in parallel, shared resources are in very high demand. This will affect the installation plan of the end station instruments, which will have to be installed sequentially and spaced in time. We anticipate that only one of the two PXRD instruments can be installed to be ready for the commissioning in Q2 2020. The imaging instrument will then be installed in Q4 of 2020, and subsequently the second PXRD instrument will be installed in Q2 in 2021. The dates given here are the best current estimates based on lab wide prioritization considerations.

We propose to install and commission the area detector and large sample environment instrument (Section 4, PXRD2) first as this is the most versatile instrument. The large detector will allow users to quickly obtain good statistics even if the beamline is not ready to run at the maximum flux, e.g. if the undulator gap is restricted, etc. This instrument will also allow for many experiments using bespoke sample environments although it is foreseen that automatic metadata collection will not be implemented for all sample environments in the initial operation phase. This decision was also recommended by the review committee and by the DanMAX steering group.

9.1. Day one capabilities

To facilitate the initial expert user experiments, i.e. final part of the commissioning, we need to be able to control at least the ID, hDCM, slits, shutters and end station HW. We must also have functioning beam viewers in order to align and monitor the beam. The interface to the optics control may initially be via a command line interface as we need to learn the most used workflows before developing a GUI. The MLM and CLR units are preferably also commissioned and ready. However, these are not essential for the initial operation. If these are not available, harmonic rejection nor focusing will not be available, i.e. experiments would have to be performed at high photon energy and slits would have to be used to define the beam size.

In the upstream end of EH1, we need to have the attenuator and the shutter in place, and have full control over these.

The granite stage and hexapod also need to be in place and interfaced to the control system. The granite stage will not be under grouted, as it will likely have to be moved during installation of the imaging instrument. Initially, a breadboard can be mounted on the hexapod, but preferably, we can have the kinematic mounting system ready. On the granite base we need to have slits, a beam intensity monitor, a sample microscope, and a motorized beam stop. All of these devices must be interfaced to the control system.

An area detector must also be available, ideally the final one, i.e. the PILATUS3 X 2M CdTe. However, if this detector is not yet ready it is possible to use a temporary detector, borrowed either at MAX IV or from Dectris. It is preferable to have access to a Piltus3 detector as no changes to the data pipeline would be needed once the final detector arrives.

As the imaging instrument will not be installed in the commissioning and initial operations phase, the detector positioning system will also not be available. As a temporary solution, we will use a sturdy

table and mount the detector on a translation stage to vary the SDD. The motion will be quite limited and the detector will be perpendicular to the beam.

The user interface for the end station will, as for the optics, initially be a command line interface. Later on, when workflows are more defined, we will develop a GUI to make the instrument more user friendly. It is, however, important that a simple data pipeline is available to be able to take advantage of the archiving system at MAX IV, as the data is then directly available to the users and to the computing cluster that can be used to reduce the data (i.e. azimuthal integration).

The range of sample environments available from day one will be rather limited. However, we will have the sample spinners described in section 4.2.1 ready. We will also prioritize that an open flow nitrogen cryostream is available for low temperature work. Furthermore, we anticipate that the chemical reactors, and in-kind delivery from Aarhus University will be ready early on. One of these include a small heater that can heat to approximately 800 °C.

Some of the later commissioning experiments will aim at expanding the SE portfolio, i.e. making the AMPIX battery setup[22] ready for user operations, and similarly for the X-ray fluorescence detector.[20]

9.2. Timeline

Both the insertion device (ID) and front end (FE) have passed their site acceptance tests. The FE has been installed, and remaining work will be completed during the fall of 2019. The ID was installed during the summer of 2019 and remaining installation work will be completed during the fall. Before commissioning of the ID and FE can start, a radiation safety permit is needed. The radiation safety team is responsible for this work and performs the necessary simulations. This is one of the current bottlenecks at MAX IV and the MAX IV management controls prioritization. It is unlikely that the permit will be granted before February-March 2020. Thus, commissioning with beam can probably not start before March 2020. We therefore aim to have the X-ray optics installed and functional by this time. The remaining major milestones for the project are shown in the Gantt chart in Figure 51.

The X-ray optics will be delivered in two parts, the diagnostics and CRL in September and the monochromators in the third week of October 2019. Preparations for installation is underway to facilitate installation as soon as possible, e.g. motor controls, survey and alignment, floor preparations, etc. To protect both personnel, equipment and machine, a PLC system is needed. This system will primarily monitor temperature and vacuum level. The PLC group is another bottleneck resource and thus presents another risk for potential delays. The MAX IV management determines the prioritization of the PLC group. We foresee that the site acceptance test for the X-ray optics can be performed without the PLC system. However, it needs to be implemented fully before starting the real commissioning with beam.

The immediate future will be spent on designing/procuring the equipment with long lead time for the PXRD 2D, namely hexapod and detector. It is anticipated that this can be completed during the fall. Procurement of the imaging setup will take place in parallel. However, more design work is needed, and thus contracts are not expected to ready before the end of 2019.

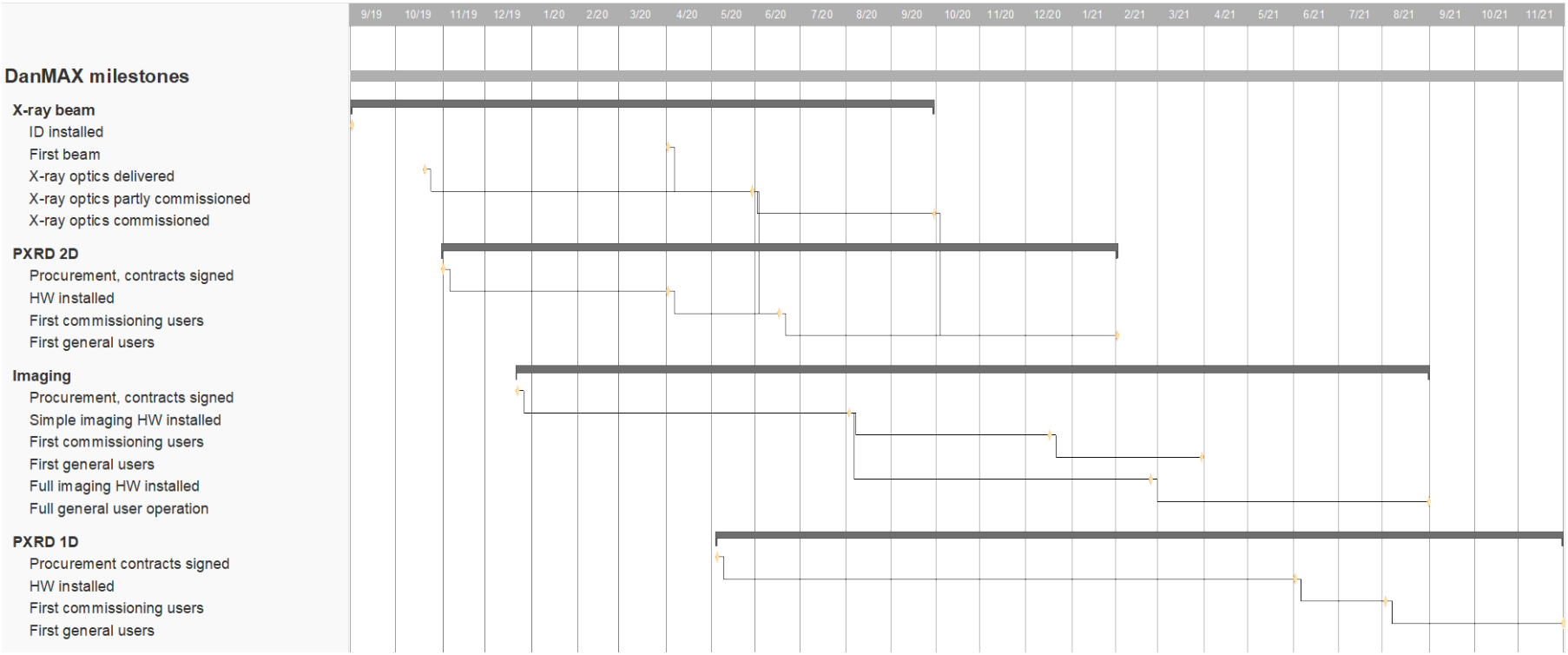

Figure 51 Gantt diagram showing the major remaining milestones in the project. The project has been divided into X-ray beam and the three instruments.

The PXRD 2D instrument follows a simple linear plan with little interdependencies to the following pieces of instrumentation. The instrument will use the large detector gantry that will be installed in the second phase of the imaging instrument installation during the spring of 2021. This will cause some disruptions to the user operations. To minimize disruptions, we hope to keep the temporary detector set-up as long as possible. Initial operations with the detector gantry may also be limited to e.g. SDD changes until all motions have been fully tested. General user operation of PXRD 2D is expected in March 2021.

The imaging set-up installation and commissioning are slightly more complex tasks as the instrument will be implemented in two major phases. Phase I will consist of a simple set-up that will allow for commissioning of, e.g. the beamline's various modes, the detectors and the data pipeline. It will also be useful for simple projection imaging and tomography, i.e. absorption and phase contrast. We thus anticipate that the phase I instrument will be used for both commissioning and experiments by general users while the phase II instrument is being installed. Naturally, major disruptions will happen during the installation of the imaging sample stage. However, we anticipate that the PXRD 2D instrument can remain in operation during most of the installation period. General users on the phase I imaging instrument are expected in April 2021, and general users on the phase II instrument in September 2021.

The PXRD 1D instrument will be procured in the first half of 2020, but it is not anticipated that it will be installed until the summer of 2021. By having the hardware on-site early, it may be possible to accelerate the installation by doing it whenever there are available resources. The installation of the PXRD 1D should not cause disruptions to either of the other instruments. General users on the PXRD 1D are expected at the end of 2021.

10. References

Basham, M., Filik, J., Wharmby, M.T., Chang, P.C.Y., El Kassaby, B., Gerring, M., Aishima, J., Levik, K., Pulford, B.C.A., Sikharulidze, I., Sneddon, D., Webber, M., Dhesi, S. S., Maccherozzi, F., Svensson, O., Brockhausser, S., Nàray, G. & Ashton, A. W. (2015). *J. Synchrotron Rad.* **22**, 853-858.

Bergamaschi, A., Cervellino, A., Dinapoli, R., Gozzo, F., Henrich, B., Johnson, I., Kraft, P., Mozzanica, A., Schmitt, B. & Shi, X. (2010). *J. Sychotron. Rad.* **17**, 653-668.

Brönnimann, C. & Trüb, P. "Hybrid Pixel Photon Counting X-ray Detectors for Synchrotron Radiation" in Jaeschke, E. J. *et al.* (Eds.) "Synchrotron Light Sources and Free-Electron Lasers". Springer International Publishing, Switzerland, 2016.

Cipriani, F., Felisaz, F., Launer, L., Aksoy, J.-S., Caserotto, H., Cusack, S., Dallery, M., di-Chiaro, F., Guijarro, M., Huet, J., Larsen, S., Lentini, M, McCarthy, J., McSweeney, S., Ravelli, R., Renier, M., Taffut, C., Thompson, A., Leonard, G. A. & Walsh, M. A. (2006). *Acta Cryst.* D**62**, 1251-1259

Coelho, A. A. (2018). *J. Appl.Cryst.* **51**, 210-218.

Dippel, A.-C., Liermann, H.-P., Delitz, J. T., Walter, P., Schulte-Schrepping, H., Seeck, O. H. & Franz, H. (2015). *J. Synchrotron Rad.*, **22**, 675-687.

Du, R., Cai, Q., Chen, Z., Gong, Y., Liu, H. & Wu, Z. (2016). *Instrum. Sci. Technol.* **44**, 1-11.

Filik, J., Ashton, A. W., Chang, P. C. Y., Chater, P. A., Day, S. J., Drakopoulos, M., Gerring, M. W., Hart, M. L., Magdysyuk, O. V., Michalik, S., Smith, A., Tang, C. C., Terrill, N. J., Wharmby, M. T. & Wilhelm, H. (2017). *J. Appl. Cryst.*, **50**, 959-966.

Finger, L. W., Cox, D. E. & Jephcoat, A. P. (1994). *J. Appl. Cryst.* **27**, 892-900.

Gozzo, F., Cervellino, A., Leoni, M., Scardi, P., Bergamaschi, A. & Schmitt, B. (2010). *Z. Kristallogr.* **22**, 616-624.

Gundlach, C., Poulsen, H. F., Jørgensen, M. R. V. & Iversen B. B. (2014). "Conceptual Design Report for DANMAX –In situ materials studies in the 10-35 keV range using powder X-ray diffraction and full field imaging", Nov. 2014. https://www.maxiv.lu.se/wp-content/plugins/alfresco-plugin/ajax/downloadFile.php?object_id=ebf5bcc4-5971-488e-a704-616bca0aa735

Hülsen, G., Brönnimann, C. & Eikenberry, E. F. (2005). *Nucl. Instr. Meth. Phys. Res. A* **548**, 540-554.

Jones, E., Oliphant, T. & Peterson, P. (2001) SciPy: Open Source Scientific Tools for Python, www.scipy.org.

Kiefer, J., Petitdemange, S. & Vincent, T. (2018). *J. Synchrotron Rad.*, **25**, 612-617.

Kantor, I., Knudsen, E. B. & Jørgensen, M. R. V.: "Detailed Design Report for DanMAX: *In situ* materials studies in the 15-35 keV range using powder X-ray diffraction and full field imaging at MAX IV." Version 2.0, December 2017. https://www.maxiv.lu.se/wp-content/plugins/alfresco-plugin/ajax/downloadFile.php?object_id=de5d7143-953e-4972-8b7d-1c89de16e995

Kato, K., Tanaka, Y., Yamauchi, M., Ohara, K. & Hatsui, T. (2019). *J. Synchrotron Rad.*, **26**, 762-773.

Katsuya, Y., Song, C., Tanaka, M., Ito, K., Kubo, Y. & Sakata, O. (2016). *Rev. Sci. Instrum.* **87**, 016106.

Kawaguchi, S., Takemoto, M., Osaka, K., Nishibori, E., Moriyoshi, C., Kubota, Y., Kuroiwa, Y. & Sugimoto, K. (2017). *Rev. Sci. Instrum.* **88**, 085111.

Kieffer, J. & Karkoulis, D. (2013), *J. Phys: Conf. Ser.*, **425**, 202012.

Knudsen, E. B., Prodi, A., Baltser, J., Thomsen, M., Willendrup, P. K., Sanchez del Rio, M., Ferrero, C., Farhi, E., Haldrup, K., Vickery, A., Feidenhans'l, R., Mortensen, K., Nielsen, M. M., Poulsen, H. F., Schmidt, S. & Lefmann, K. (2013). *J. Appl. Cryst.* **46**, 679-696.

Kraft, P., Bergamashi, A., Brönnimann, Ch., Dinapoil, R., Eikenberry, E. F., Graafsma, H., Henrich, B., Johnson, I., Kobas, M., Mozzanica, A., Schlepütz, C. M. & Schmitt, B. (2009). *Trans. Nucl. Sci.* **56**, 758-764.

Lee, J. H., Almer, J., Aydiner, C., Bernier, J., Chapman, K., Chupas, P., Haeffner, D., Kump, K., Lee, P. L., Lienert, U., Miceli, A. & Vera, G. (2007). *Nucl. Instr. Meth. Phys. Res. A* **582**, 182-184.

Rodriguez-Carvajal, J. & Gonzalez-Platas, J. CrysFML, ILL and ULL, Tenerife, Spain (LGPL 3.0): IUCr Newsletter (2003), 1, 50-58. https://forge.epn-campus.eu/projects/crysfml

Ruat, M., Andrä, M., Bergamaschi, A., Barten, R., Brückner, M., Dinapoli, R., Fröjdh, E., Greiffenberg, D., Lopez-Cuenca, C., Lozinskaya, A. D., Mezza, D. Mozzanica, A., Novikov, V. A., Ramilli, M, Redford, S., Ruder, C., Schmitt, B., Shi, X., Thattil, D., Tinti, G., Tolbanov, O. P., Tyazhev, A., Vetter, S., Zarubin, A. N. & Zhang, J. (2018). *JINST*, **13**, C01046.

Sabine, T. M., Hunter, B. A., Sabine, W. R. & Ball, C. J. (1998). *J. Appl. Cryst.* **31**, 47-51.

Thompson, P., Cox, D. E. & Hastings, J. B. (1987). *J. Appl. Cryst.* **20**, 79-83.

Tolborg, K., Jørgensen, M. R. V., Christensen, S., Kasai, H., Becker, J., Walter, P., Dippel, A.-C., Als-Nielsen, J. & Iversen, B. B. (2017). *Acta Cryst.* B**73**, 521-530.

Trueb, P., Dejoie, C., Kobas, M, Pattison, P., Peake, D. J., Radicci, V., Sobott, B. A., Walko, D. A. & Broennimann, C. (2015). *J. Synchrotron Rad.*, **19**, 347-351.

Trueb, P., Sobott, B. A., Schnyder, R., Loeliger, T., Schneebeli, M., Kobas, M, Rassool, R. P., Peake, D. J. & Broennimann, C. (2012). *J. Synchrotron Rad.*, **22**, 701-707.
van der Veen, J. F., Riemersma, A. J., Schlatter, H., Abernathy, D. L. & Grübel, G. (1997). *J. Synchrotron Rad.*, **4**, 64-66.
van Rossum, G. & Drake, F. L. (2006) Python Reference Manual, Python Software Foundation, www.python.org.
Willendrup, P., Filges, U., Keller, L., Farhi, E. & Lefmann, K. (2006). *Physica B Cond. Matt.* **385**, 1032-1034.

Appendix A. List of Abbreviations

aSi TFT	Amorphous silicon thin film transistor (detector)
CCD	Charge doupled device
CDR	Conceptual design report
CMOS	Complementary metal-oxide semiconductor
Cps	Counts per second
CRL	Compound refractive lens
CV	Computer vision
DAC	Diamond anvil cell
DCM	Double crystal monochromator
DoF	Depth of field
DDR	Detailed design report
EH1	Experimental hutch 1 (PXRD and Imaging instruments)
EH2	Experimental hutch 2 (Future development – not part of the current project)
FoV	Field of view
FWHM	Full width at half maximum
HH	Higher harmonics
HPAD	Hybrid pixel array detector
MLM	Multilayer monochromator
NA	Numerical aperture
OH	Optics hutch
OM	Omega, ω
PSS	Personnel safety system
PXRD	Powder X-ray diffraction
PXRD1	High resolution instrument with 1D detector
PXRD2	Area detector and large sample environment Instrument
Q	Momentum transfer [$Å^{-1}$], $Q = 4\pi \sin(\theta) / \lambda$
SDD	Sample to detector distance
SE	Sample environment
SNR	Signal-to-noise ratio
SOC	Sphere of confusion
SRM	Standard reference material
SW	Software
TTH	Two theta, 2θ
TS	Total scattering
UHV	Ultra high vacuum

Appendix B. Details of the Simulations

The simulations presented in this report were performed using the McXtrace (Knudsen *et al.*, 2013) model developed during the design of the optical layout. Details about this model can be found in the DDR (Kantor *et al.*, 2017). In general, the virtual beamline is perfectly aligned and slits/apertures are perfect absorbers.

The coordinate system used throughout this report is compliant with the MAX IV and McXtrace convention, as illustrated in Figure B.1.

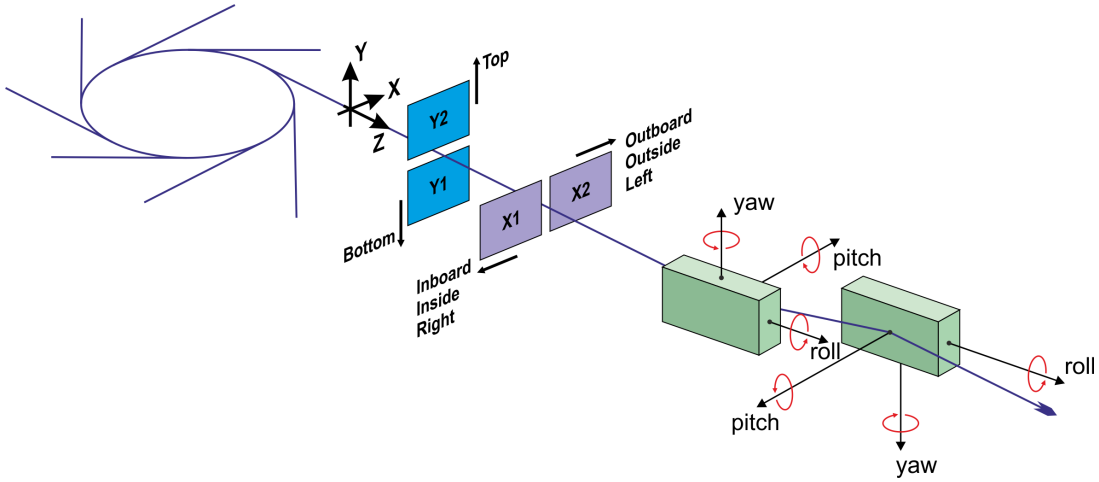

Figure B.1 Coordinate system used in this report. Not shown: 'Downstream' = +Z, 'Upstream' = -Z. Figure adapted from original by Peter Sjöblom and Antonio Bartalesi (MAX IV).

To test the performance of the instruments at different settings, the following standard reference material (SRM) was simulated:

LaB_6 (NIST SRM 660b): Measured on the Aarhus Vacuum Imaging plate Diffractometer (Tolborg et al., 2017) at the P02.1 beamline at PETRAIII, DESY, Germany (Dippel *et al.*, 2015): Space group: Pm-3m (#221), Lattice parameter: 4.15689 Å

Atom name	Atom type	X	Y	Z	B_{iso}	Occupancy
La1	La	0	0	0	0.4232	1
B1	B	0.1975	0.5	0.5	0.3166	0.1667

The simulation of the sample scattering is based on the McXtrace component; PowderN (Willendrup et al., 2006). This component uses tabulated crystallographic input, in this case prepared with the CIF2HKL program, which uses the CrysFML library (Rodriguez-Carvajal & Javier Gonzalez-Platas). This library uses the independent atom model, i.e. neglecting bonding effects and/or electron transfer.

In all cases the sample is modeled as a cylinder to emulate a capillary.[35] The packing fraction of the capillary is set to 60%. Thermal diffuse scattering is not modelled. Here we assume an ideal powder, i.e. perfect crystallite averaging and no broadening due to size and stain effects. This means that the

[35] A plate shaped sample is simulated in one case.

only source of broadening is from the instrument, incoming beam and sample diameter. The keyword SPLIT is used to retrace each 'photon' reaching the sample multiple times, in order to improve the statistics.

Scattering from the capillary and air scattering is not included in the simulation. Similarly, Compton scattering has not been included in the simulation, thus there is no background signal. In the real experiments air scattering and scattering from the sample holder (and/or sample environment) will naturally increase the background level.

Detector Simulation

To our best knowledge, the detectors discussed and used as models in the simulations throughout this document are the best of the available technologies at this time. Furthermore, they are commercially available and potentially within the budget of the beamline. Most of, if not all, the detectors for the beamline have to be procured through an open tender procedure, and thus, the detectors (and models) discussed here may not be the models implemented at the beamline.

The detectors have been modeled using the PSD_MONITOR component. This component has no point spread and has an efficiency of 100%. Modern hybrid pixel array detectors (HPAD) and microstrip detectors have point spread functions of approximately one pixel, i.e. a similar performance to the MCXTRACE implementation. Real detectors have a finite thickness and do not have an efficiency of 100%, which can lead to, e.g. parallaxes effects at high oblique incident angles. This effect and other detector effects are not included in the simulations, but are discussed further in section 4.1. The detector models have been based on commercially available detectors as described in sections 5.1 and 4.1. However, for the 2D HPAD, detector, *vide infra*, the gaps have been omitted and the detector is modelled as a continuous active area. The pixel size corresponds to the actual detector, leading to a slightly smaller area overall. The microstrip has been modelled with gaps between the modules.

Modeling of Simulated Data

Since there is no texture in the simulated samples, the resulting (simulated) data is converted to intensity vs. scattering angle for both instruments. For the microstrip detector, the data is already available as one-dimensional data, but a script was used to convert from pixel number to 2θ (and to include the blind regions in-between the separate modules). The simulated data from the area detectors is azimuthally averaged to yield 1D data using the PYFAI library (Kieffer & Karkoulis, 2013). As shown in section 4.3 the simulated peak shape is close to Gaussian, but with indications of small shoulders and less intensity in the tails. This means it is quite different from the expected, quite Lorentzian, (pseudo) Voight function. We believe that this is an artefact from the simulation of the sample and not an indication of poor instrument performance.

It was attempted to model the reduced 1D data in the TOPAS-ACADEMIC V6 (Coelho, 2018) using a Gaussian profile function. However, this approach led to a rather poor fit with large residuals. Additionally, the Thompson-Cox-Hastings parametrization (Thompson *et al.*, 1987) does not seem to be able to describe the profile well. An example is shown in Appendix C. However, we believe that the FWHM of the peaks gives a rough indication of the instrument performance, and thus, these have been extracted from the data using single peak fitting with Gaussian functions.

Appendix C. Rietveld Refinement Against Simulated Data

A simulation was performed with a ⌀ 200 µm capillary with LaB_6 at 60% packing density, 35 keV radiation from the DCM and 250 µm slits. The detector was a PILATUS3 2M[36] at 150 mm SDD. The simulated 2D data was azimuthally integrated using the PyFAI library (Kieffer & Karkoulis, 2013). The resulting reduced 1D data was used for Rietveld refinement in the TOPAS-Academic V6 (Coelho, 2018). Here a Gaussian profile was used. The unit cell was kept fixed, while the wavelength was allowed to vary. All positional parameters were kept fixed, but the isotropic thermal was varied along with the scale factor and the profile parameters. The resulting fit is shown in Figure C.1. It is immediately clear that the fit is quite poor, which is also reflected in the R-values; R_{wp} = 19.3 and R_{Bragg} = 44.4. The refined thermal parameters B_{eq}(La) = 0.499(3) and B_{eq}(B) = 0.33(3), are reasonably close to the expected values of 0.42 and 0.31, respectively. The refined wavelength does not change significantly.

It is apparent that the peaks in the full range are fitted poorly with the parametrization of the peak width. To compare to the Gaussian fit to a single peak, see Figure C.2, which is directly comparable to the lower left panel of Figure C.1.

The fitted profiles are too narrow up to around $2\theta \lesssim 40°$ where all have residuals approximately the same shape (+-+). At higher angles the profile gradually matches the simulated data better and from $2\theta \approx 40°$ the negative central peak disappears (++). At $2\theta \gtrsim 50°$ the profiles are too wide and the residuals generally become a single negative peak (-), see lower right panel of Figure C.1. It therefore seems that the combination of low flexibility (few parameters) and parametrization of the peak profile prevents a good fit. The same trend is observed for the simulated data on the high resolution instrument.

We believe that the unexpected profile is caused by the sample description used in the simulation code and is not an indication of the instrument design. Instruments similar to the proposed design exist and the recorded data are commonly fitted well with the Thompson-Cox-Hastings parameterized pseudo-Voight function (Thompson *et al.*, 1987). However, it unfortunately means that the results of the simulation, i.e. the single peaks fits presented in sections 4.3 and 5.5 can probably only be considered as a rough indicator of the instrument performance.

[36] The detector is modeled as a continuous module, i.e. without gaps

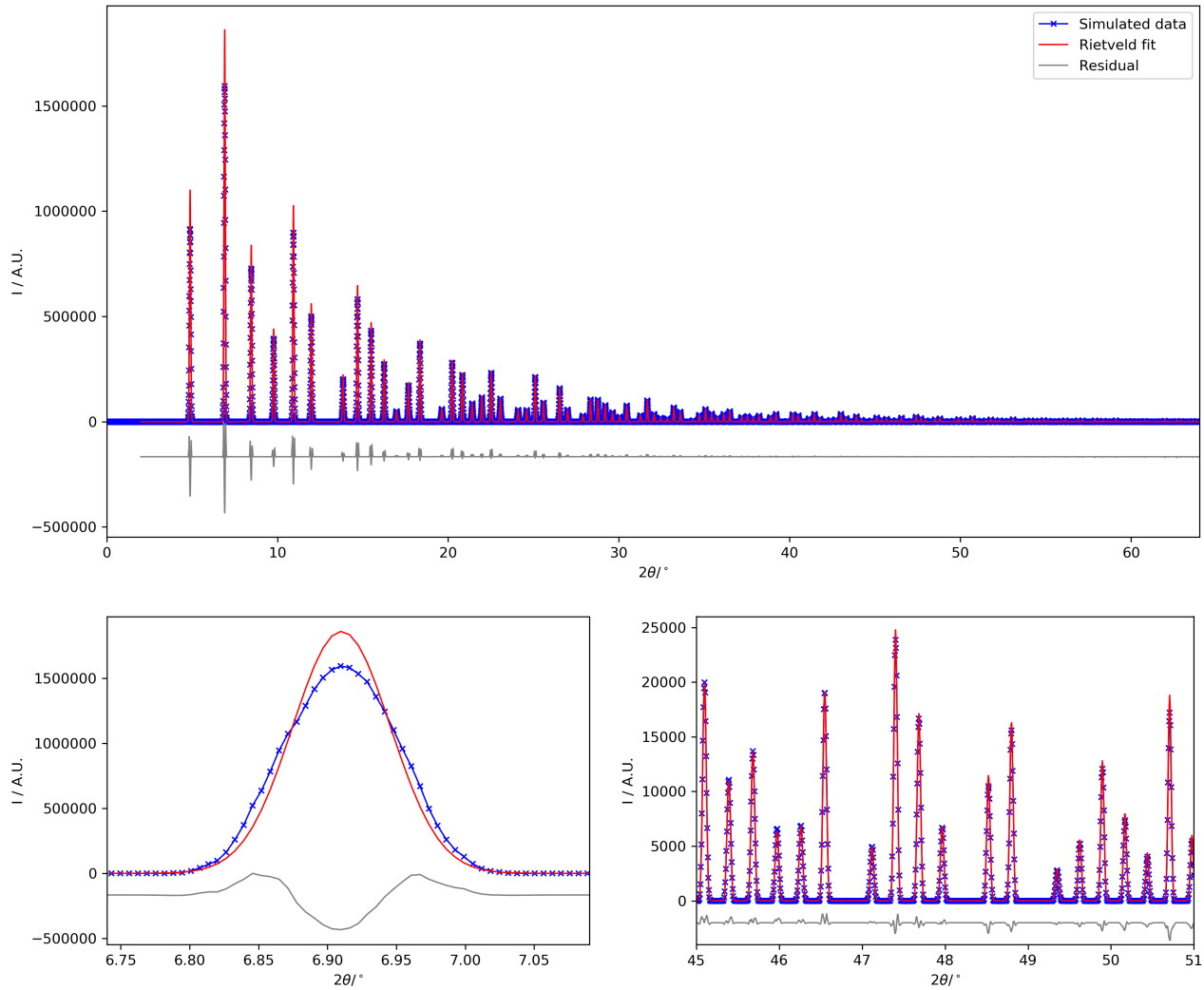

Figure C.1 Rietveld fit against simulated data on a ⌀200 µm LaB_6 capillary using a 35 keV DCM beam and a PILATUS3 2M detector at 150 mm SDD. A Gaussian peak profile was used. Blue line and crosses show the simulated data, the red line show the Rietveld model, and the grey line shows the residual (and an arbitrary offset).

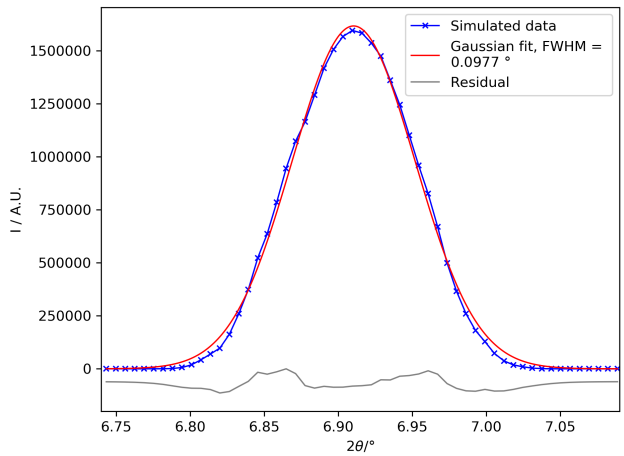

Figure C.2 Gaussian single peak fit against simulated data as shown in Figure C.1. This figure is directly comparable to the lover left panel in Figure C.1.

Appendix D. Accuracy, Precision, Repeatability & Resolution

In this design report we will use accuracy, precision, repeatability and resolution to describe mechanical motion in the following way:

Accuracy:
The accuracy is the measure of the difference between the absolute position of the axis or stage and the position measured by the encoder (peak to peak). The accuracy can only be determined via external (calibrated) measurements. The accuracy can thus be dependent on (and or improved with) a calibration table.

Precision:
The precision is a measure of the spread of the positional readings from the encoder. It is in principle not linked to accuracy nor repeatability.

Encoder resolution:
The encoder resolution describes the minimum increment detectable by the encoder.

Mechanical resolution:
The mechanical resolution is the minimum mechanical increment of a motion based on a motor step (by either full step or micro-stepping).

Repeatability:
The repeatability is the absolute (peak to peak) deviation of the actual position from the target value while repeating the same motion. In other words, it is the variance of several accuracy measurements.

Sphere of Confusion (SOC):
The SOC is defined as the maximum deviation of the sample position from its reference value when a single axis or an arbitrary combination of axis is rotated. This distance corresponds to the radius of the SOC.

Appendix E. Secondary Focusing - Original Instrument Location

The following section shows the complete analysis of how secondary focusing can be used to further focus the beam onto the original, downstream, PXRD 2D sample position. A similar analysis for the new instrument location, leveraging the main conclusions from this section, can be found in section 7.

The CRLs can be positioned on the SE table at the PXRD 1D instrument (~44.8 m from the source), i.e. ~1.9 m upstream of the 2D PXRD instrument, leading to a theoretical demagnification of approximately 24. On the table there is a lot of flexibility to move the CRLs, e.g. near the sample position or up to ~1 m further downstream, if needed. The simulations performed here focus on two cases: 1) 1.9 m distance between CRLs and sample and 2) 70 lenses in a cassette with an shorter working distance. These examples serve to illustrate the possibilities and how different focus schemes compare.

Several schemes to obtain a tighter focus using 2D CRLs can be imagined as shown in Figure E.1. The performance of the focusing schemes are evaluated based on the FWHM of the beam at the sample position and the flux through a 10 x 10 µm^2 and a 3 x 3 µm^2 *square aperture*. The FWHM has been obtained by fitting a Gaussian profile to the ray tracing results on a larger monitor. To obtain better statistics, the data is summed along the vertical direction of the virtual monitor to obtain the horizontal profile, and vice versa. The flux values are compared to the flux through the same apertures for the beam focused at the sample position using the CRLs in the optical hutch only. The gain is calculated as the ratio of the flux for the current simulation and the reference, i.e. OH CRLs only. All simulations have been performed at 35 keV using the DCM only. It should be noted that magnetic phase errors have been neglected, meaning that the flux numbers presented here are likely overestimated by 30-35%.

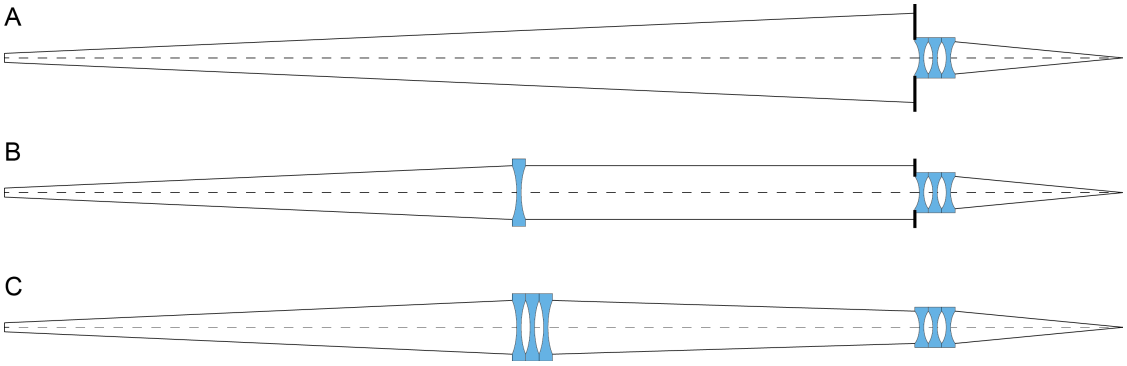

Figure E.1 Possible schemes for secondary focusing using CRLs. A: Direct focusing by CRLs in EH1. B: Collimation of the beam using the CRLs in the OH and secondary focusing in EH1. C: Focusing the beam using the CRLs in the OH to match the aperture of the CRLs in EH1.

E.1. Focusing Using CRLs in the Experimental Hutch Only

A single focusing element (scheme A) is normally expected given the tightest focus. However, the geometrical aperture of the CRLs will limit the throughput since a large proportion of the beam will not reach aperture of the CRLs. To increase the fraction of photons, it is possible to increase the apex radius and thereby the aperture. If using lenses with a radius of 200 µm (identical to the OH transfocator), 214 lenses are needed to focus the beam 1.9 m downstream. The expected best focus

performance is listed in Table E.1. The 214 lenses will yield a beam with dimensions down to ~5 x 1 μm^2 (FWHM) and a gain factor, relative to the OH focused beam, of 1.36 and 7.76 in a 10 x 10 μm^2 (FWHM) and 3 x 3 μm^2 (FWHM) square aperture, respectively.

Table E.1 Focusing performance using one cassette of lenses in either the OH or in EH1 at 35 keV. The gain is calculated against the focus using only the CRLs in the OH.

Scheme Figure E.1	# CRL in OH	# CRL in EH1	EH CRL apex radius [µm]	EH CRL position [m]	Focus (FWHM) [µm]		10 x 10 μm^2 aperture		3 x 3 μm^2 aperture	
					Hor.	Ver.	Flux [ph/s]	Gain	Flux [ph/s]	Gain
-	0	0	-	-	823	1190	$7.6x10^{6}$	$3x10^{-5}$	$2.4x10^{5}$	$1x10^{-5}$
-	34	0	-	-	64.7	13.6	$2.5x10^{11}$	1.00	$2.3x10^{10}$	1.00
A	0	214	200	44.8	5.2	1.2	$3.4x10^{11}$	1.36	$1.8x10^{11}$	7.76
A	0	50	50	44.8	5.3	0.7	$2.6x10^{11}$	1.05	$1.3x10^{11}$	5.68

The high number of lenses required represents a significant investment and is very different from the expected imaging objective. It is therefore necessary to evaluate the performance of the lenses with the smallest apex radius commercially available; 50 µm. The results are included in Table E.1. It is obvious that in terms of gain the performance is 30-40% lower than the 200 µm lenses. The focus spot is, however, quite similar, if not slightly better[37] than the larger aperture lenses. The divergence of the focused beams is nearly independent of the lens apex radius and has a value of 25 µrad (RMS) in both horizontal and vertical directions. Considering the difference in price (proportional to the number of lenses) and the compatibility with the imaging setup, it is clear that the 50 µm CRLs are the superior choice.

The best focus spot produced at the sample position is an image of the source and thus, has an oval shape, as illustrated in Figure E.2. The divergence of the unfocused beam is similar in the horizontal and vertical directions, namely 6.3 µrad (RMS) and 8.0 µrad (RMS). This causes the focal point in both the horizontal and vertical direction to coincide when the beam is focused using 2D CRLs, see Figure E.3. Consequently, the ideal 'round' beam can only be obtained outside the focus positions, e.g. by moving the CRLs closer to or further away from the sample position, as shown in Figure E.4, or equally by adjusting the number of lenses to change the focal length.

The beam shape is close to ideal for a 10 x 10 μm^2 (FWHM) beam when the CRL are moved 70 mm upstream, but the flux is only 75% of the flux in a 10 x 10 μm^2 section of the beam focused from the OH CRLs. However, by using this approach it might be possible to limit the amount of scattering from the pinhole needed to shape the beam focused using the OH CRLs. This approach will have to be tested at the beamline to find the best practical solution.

[37] The distance between CRL and sample position has not been optimized for the 200 µm CRLs. However, considering the large number of lenses this effect should be minimal.

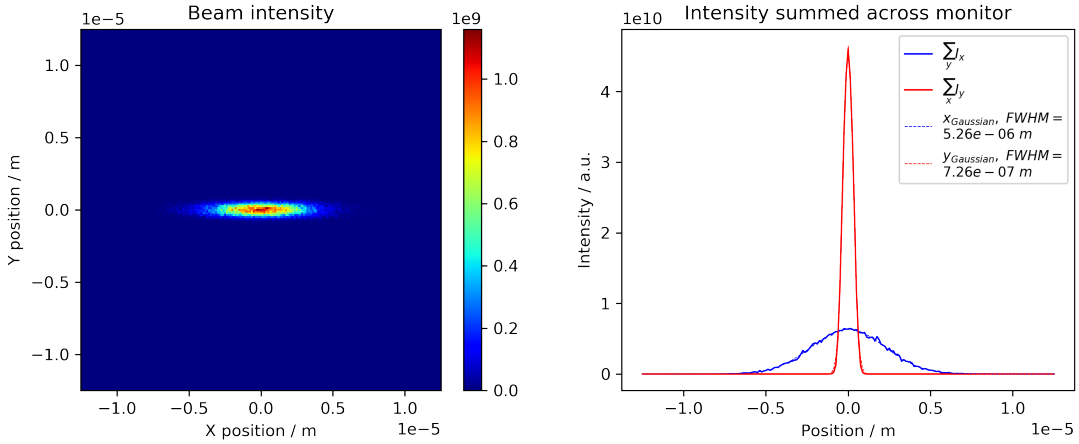

Figure E.2 Beam shape at the 2D PXRD instrument using 50 CRLs with 50 µm apex at 1900 mm upstream of the focus. The simulation was performed at 35 keV using the DCM only. The flux and gain are listed in Table 5.

In principle it is possible to insert 1D focusing lenses close to the sample to decrease the horizontal profile of the beam, but the gain is expected to be quite low compared to the added cost for implementing this solution, and the added complexity in, e.g. alignment of another lens cassette. This approach is thus not explored further in this report.

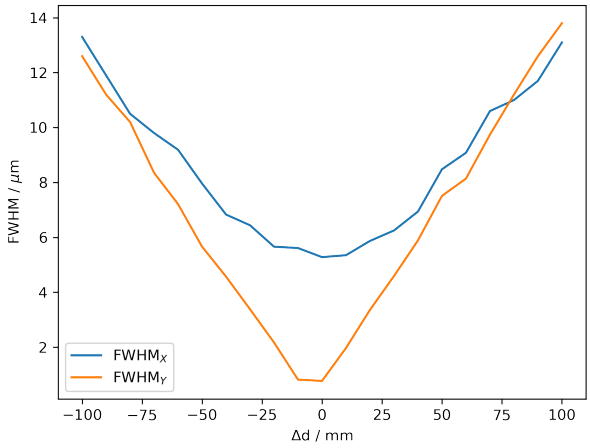

Figure E.3 Beam size as a function of distance between 50 CRLs (50 µm) and sample position. The simulation was performed at 35 keV using the DCM only. Δd = 0 corresponds to the simulation in Table 5, i.e. a CRL position of 44.8 m from the source.

It is likely that the objective necessary for dark field imaging will require more than 50 lenses. The performance of a 70 lens cassette is compared to the 50 lens cassette in Table E.2. Here two entries are listed for each cassette, namely with a distance optimized for a 10 x 10 µm^2 (FWHM) focal spot and a 3 x 3 µm^2 (FWHM) focal spot. Both configurations are capable of producing the desired spot size. However, the added absorption in the extra 20 lenses decreases the flux significantly.

All in all, we conclude that no significant gains can be achieved by using 2D CRLs in scheme A to obtain a 10 x 10 µm^2 (FWHM) beam. A gain of approximately 4 can be obtained for a 3 x 3 µm^2 (FWHM) beam. It can also be concluded that a cassette with 50 lenses is preferable to a larger cassette.

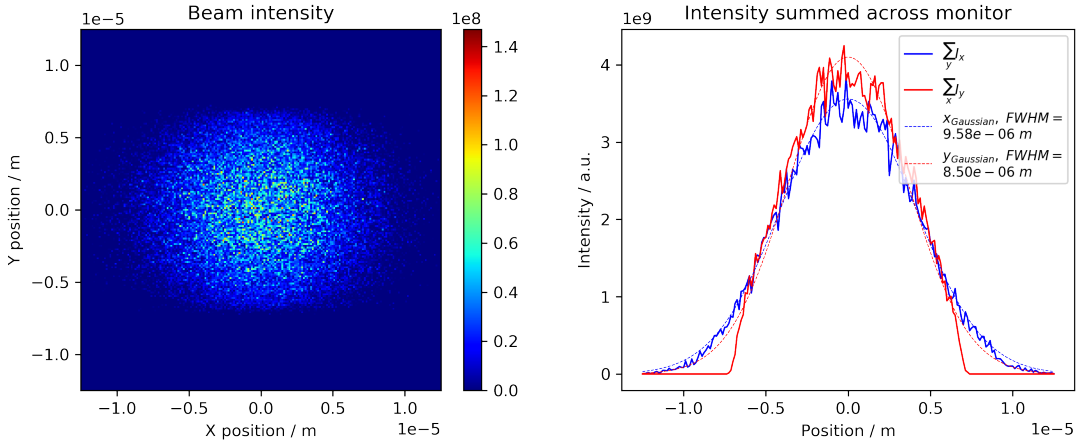

Figure E.4 Beam shape at the 2D PXRD instrument using 50 CRLs with 50 µm apex at 1970 mm upstream of the focus without pinholes. The simulation was performed at 35 keV using the DCM only.

Table E.2 Focusing performance using one cassette of lenses in EH1 at 35 keV. Two CRL cassettes are simulated, namely 50 lenses and 70 lenses. Both cassettes have been translated along the beam in 10 mm increments to find the best position to yield a 10 x 10 µm^2 (FWHM) and 3 x 3 µm^2 (FWHM) focus, respectively. The gain is calculated against the focus using only the CRLs in the OH. Bold typeface indicates the values intended for the particular configuration.

Scheme Figure E.1	# CRL in OH	# CRL in EH1	EH CRL apex radius [µm]	EH CRL position [m]	Focus (FWHM) [µm]		10 x 10 µm^2 aperture		3 x 3 µm^2 aperture	
					Hor.	Ver.	Flux [ph/s]	Gain	Flux [ph/s]	Gain
A	0	50	50	44.730	9.6	8.5	**2.0x10^{11}**	**0.81**	2.5x10^{10}	1.13
A	0	70	50	45.280	10.0	9.3	**1.4x10^{11}**	**0.59**	1.7x10^{10}	0.75
A	0	50	50	44.820	5.9	3.4	2.6x10^{11}	1.05	**9.5x10^{10}**	**4.16**
A	0	70	50	45.320	4.9	2.9	2.1x10^{11}	0.85	**8.3x10^{10}**	**3.66**

E.2. Focusing Using CRLs in Both the Optical and Experimental Hutch

In scheme A presented above, the CRL aperture is over illuminated, and thus photons are lost in the guard aperture in front of the CRLs. By using the transfocator in the OH, it is possible to either collimate the beam, scheme B, or focus the beam onto the EH1 CRL aperture, scheme C.

E.2.1. Scheme B

By inserting 11 of the CRLs in the OH, a nearly parallel 35 keV beam is obtained. The resulting beam has a horizontal divergence of 1.6 µrad and a vertical divergence of 0.4 µrad. The beam size at the EH1 CRL (PXRD1 sample position, 44.8 m from the source) is approx. 460 x 780 µm^2 (h x v, FWHM). The collimated beam is also over illuminating the ø400 µm geometric aperture of the CRLs. However, it is a better match compared to scheme A. The performance of the two 50 and 70 lens cassettes in the collimated beam is compared in Table E.3.

The gain for the 10 x 10 µm^2 aperture is almost doubled compared to scheme A in both cases, but is only marginally better than the focus obtained using the OH CRLs only. The CRL with 50 lenses is outperforming the cassette with 70 lenses as also seen above. For the 3 x 3 µm^2 aperture the gain is also significantly improved. Here both cassettes perform similarly. As the depth of field is quite

narrow and the sampling along the beam is coarse at 10 mm intervals, it is expected that the gain can be slightly improved to around 8 in both cases.

Table E.3 Focusing performance using a collimated 35 keV beam and one cassette of lenses in EH1. Two CRL cassettes are simulated, namely 50 lenses and 70 lenses. Both cassettes have been translated along the beam in 10 mm increments to find the best position to yield a 10 x 10 μm^2 (FWHM) and 3 x 3 μm^2. Bold typeface indicates the values intended for the particular configuration.

Scheme Figure E.1	# CRL in OH	# CRL in EH1	EH CRL apex radius [µm]	EH CRL position [m]	Focus (FWHM) [µm]		10 x 10 μm^2 aperture		3 x 3 μm^2 aperture	
					Hor.	Ver.	Flux [ph/s]	Gain	Flux [ph/s]	Gain
B	11	50	50	44.920	9.3	7.8	**$3.8x10^{11}$**	**1.55**	$4.4x10^{10}$	1.94
B	11	70	50	45.320	9.7	9.4	**$2.8x10^{11}$**	**1.15**	$3.6x10^{10}$	1.59
B	11	50	50	44.840	7.8	3.6	$4.8x10^{11}$	1.94	**$1.4x10^{11}$**	**6.32**
B	11	70	50	45.390	5.8	3.4	$4.4x10^{11}$	1.80	**$1.6x10^{10}$**	**6.95**

E.2.2. Scheme C

Due to the higher performance of the 50 lens cassette compared to the cassette of 70 lenses, only the case of 50 lenses is simulated for scheme C. In these simulations both the number of lenses in the OH transfocator and the position of the CRLs in the experimental hutch has been varied. The position of the CRLs is limited between the PXRD1 sample position and 1 m downstream to ensure that the unit will fit on the PXRD1 SE table. The resolution of the position scan was 10 mm. FWHM values and flux/gain values were extracted from these positional scans. For each configuration of the OH transfocator a simulation was selected where the height of the beam is approximately 3 µm (FWMH). A maximum gain of ~14 (in a 3 x 3 μm^2 aperture) is found at 27 lenses in the OH transfocator.

To investigate this configuration in detail, a series of simulations was performed with 1 mm resolution. The best result for 10 x 10 μm^2 and 3x 3 μm^2 focus is listed in Table E.4. It is obvious that scheme C, i.e. focusing on the EH2 CRL aperture, provides significant gain improvements over schemes A and B and it is recommended that this scheme is implemented at the beamline.

Table E.4 Focusing performance at 35 keV using 27 lenses in the OH and 50 lenses in EH1. The gain is calculated against the focus using only the CRLs in the OH. Bold typeface indicates the values intended for the particular configuration.

Scheme Figure E.1	# CRL in OH	# CRL in EH1	EH CRL apex radius [µm]	EH CRL position [m]	Focus (FWHM) [µm]		10 x 10 μm^2 aperture		3 x 3 μm^2 aperture	
					Hor.	Ver.	Flux [ph/s]	Gain	Flux [ph/s]	Gain
C	27	50	50	45.100	16.0	9.4	**$9.2x10^{11}$**	**3.74**	$1.1x10^{11}$	4.65
C	27	50	50	45.148	15.2	2.9	$1.2x10^{12}$	4.85	**$3.3x10^{11}$**	**14.39**

It is furthermore recommended that the CRL objective for the imaging instrument is split into two lens cassettes, one with 50 lenses for focusing of 35 keV radiation and the remaining ~20 lenses in another cassette. Detailed simulations for 20 CRLs have not been performed. However, initial calculations show that the cassettes should be useful for focusing a ~23 keV beam in a similar fashion as described above for 35 keV.

The EH CRL unit must be easy to align and reconfigure. Thus, the individual lenses have to be pre-aligned in the two cassettes. Furthermore, the cassettes must be aligned relative to each other when both in use. We are not aware of an existing design that would allow for easy manipulation of the cassettes (except for a dedicated transfocator). The unit does not need to be in vacuum, but could instead be kept under a flow of N_2 or He, which would greatly reduce the complexity. Any design must of course consider the safety aspects of handling Be lenses.

E.3. Pinhole for Focused Beam

While it is possible to obtain a 10 x 10 µm^2 (FWHM) with a nearly Gaussian profile, see Figure E.4, it is necessary to use a pinhole or a slit to obtain a 3 x 3 µm^2 (FWHM) beam. It might also be preferable to avoid part of the tails and use a pinhole to shape the 10 x 10 µm^2 beam.

To achieve a stable foundation, we propose to extend the granite base for the hexapod upstream and increase the height of a section to ~150-200 mm under the beam. This is illustrated in Figure 9. The pinhole support and XY translation would be fitted on this base. The precision requirements are quite strict due to the small beam and a sub-micron positioning capability is needed. This could e.g. be performed using piezo motors.

The pinhole will need to be quite close to the sample to effectively shape the beam, i.e. for ø3 µm pinhole the optimal position is ~20 mm upstream of the sample. The beam profiles for the focusing condition listed in Table E.4 using a ø3 µm and ø10 µm pinholes 20 mm upstream of the sample position are shown in Figure E.5 and Figure E.6, respectively.

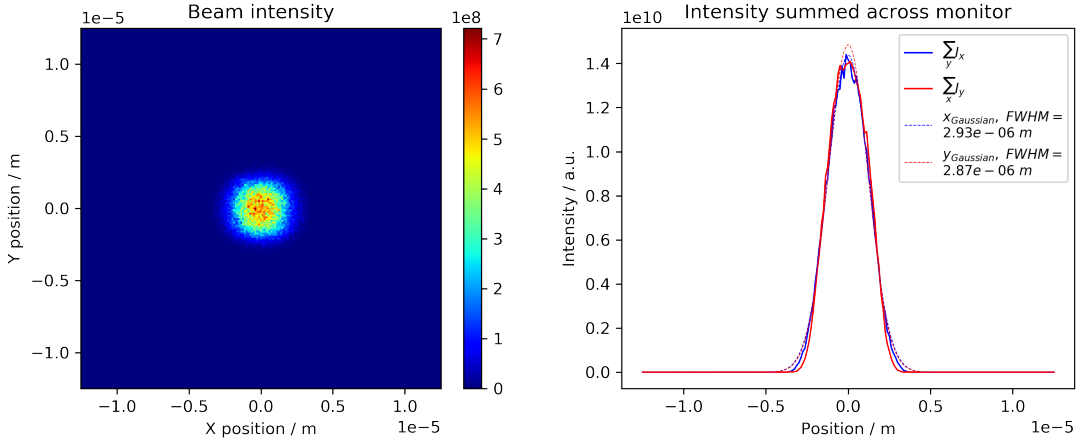

Figure E.5 Beam profile at 35 keV using 27 CRLs in the OH, 50 CRLs in the at 45.148 m from the source, and a ø3 µm pinhole 20 mm upstream of the sample. The total flux is 3.5 x 10^{11} ph/s of which 2.0 x 10^{11} are within a rectangle defined by the FWHMs.

The 3 µm (FWHM) beam is very symmetric and has a nearly Gaussian profile. The distance between the sample and pinhole (from 5 mm up to 75 mm) will mainly affect the horizontal profile. For the ø3 µm pinhole this effect starts to appear from above 20 mm and yields a profile with 6 µm FWHM at 50 mm upstream to the sample. As the profile is widened, the total flux is also decreased by approximately 55%. It might not be possible to acquire a ø3 µm pinhole with sufficient attenuation so a larger pinhole will have to be used (van der Veen *et al.*, 1997). The use of a ø5 µm pinhole at 20 mm upstream of the sample will lead to a beam size of 2.9 x 4.4 µm^2 (v x h, FWHM). The profile of the beam is less sensitive to the distance and increases to only 5 µm FWHM at 40 mm distance. The

sensitivity of the profile gradually becomes higher at longer distances. A ⌀10 µm pinhole will lead to an approximately 8 µm horizontal beam profile (FWHM).

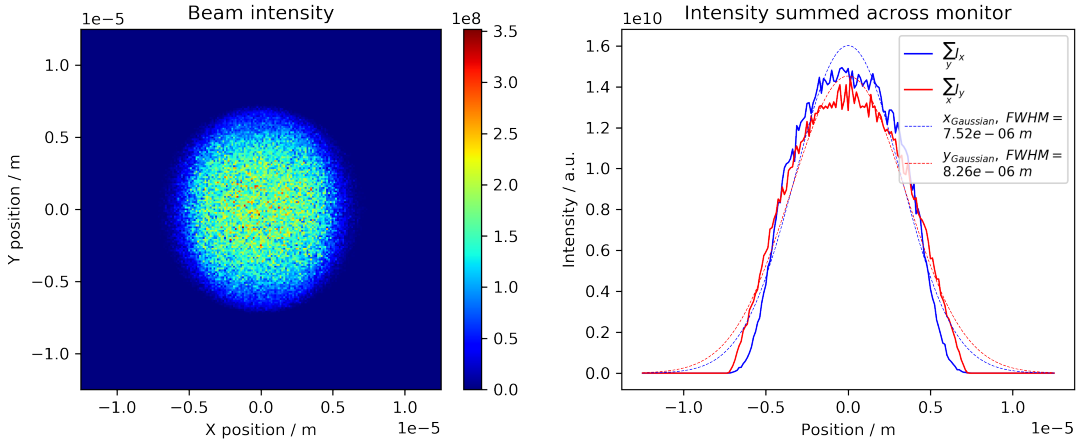

Figure E.6 Beam profile at 35 keV using 27 CRLs in the OH, 50 CRLs in the at 45.100 m from the source, and a ⌀10 µm pinhole 20 mm upstream of the sample. The total flux is 9.8 x 10^{11} ph/s of which 6.1 x 10^{11} are within a rectangle defined by the FWHMs.

The 10 µm beam is also very symmetric, but it is less Gaussian, especially in the tail regions where the intensity quickly drops off. The FWHM of the beam is largely invariant to the distance between the sample and the pinhole (up to 75 mm). However, more intensity does appear in the tails, yielding a more Gaussian profile.

Appendix F. External DDR review committee report

The original DDR was reviewed at MAX IV on March 27 to 28 2019. The panel consisted of:

- Henrik Birkedal (Aarhus University, Chair)
- Andy Fitch (ESRF)
- Andrew King (Soleil)
- Heinz Graafsma (DESY)

The committee's findings were compiled in the report enclosed on the following pages.

Report on DanMAX DDRs on the imaging and powder diffraction instruments

Henrik Birkedal (chair), Andy Fitch, Andrew King, Heinz Graafsma

The committee finds the two DDR reports very interesting. The two together provide a comprehensive suite of pxrd and imaging for the user community and will provide an excellent platform for modern material science. The proposed ideas are all sound and feasible and the analyses by raytracing analyses were highly valuable and informative.

During the discussions it was proposed to swap the position of the high resolution powder diffractometer and the imaging setup. This seems to be advantageous but we recommend that the team prior to a final decision reflect carefully on the possible consequences (raytracing, focusing, detector configurations, access and PSS system requirements etc) with the same thoroughness as the original report. This holds especially for the change of position for the gantry.

The beamline will deliver several types of experiments and we recommend that it be clearly communicated to the users in which order these can be expected to be operational together with information like expected resolutions, field of view etc. The planning should also include deliverables from MAX-IV.

The most expensive detector is the 2D area detector, which is very suitably proposed to be a Pilatus CdTe detector. An operational concern, caused by the multimodal nature of the beamline, is the danger of damage to the detector when moving it between setups. It will require care in planning to reduce this risk as well as the time overhead involved in reconfiguring the beamline. It might be worth considering having two sets of cables installed for the two experimental stations to reduce risks and time overhead when swapping the detector between setups. We strongly support the choice of the Pilatus and the concept of additionally purchasing a flat panel detector, which will add flexibility and capability as well as ease initial testing/commissioning of the experiments.
The team will also have to strike a delicate balance between user friendliness and flexibility given the multipurpose nature of the beamline especially on the imaging side.

User-brought equipment might require interfacing to the MAX-IV network. For long term equipment this is suitably planned but for development and/or one-off experiments it would be ideal to have access from the control room either through remote desktop, longer Ethernet cables, patch panel or the like.

We were encouraged by the presentation by the MAX-IV computing staff about the proposed support for data handling. Since there will be a lot of changing between setups, it will be important have as automated as possible data flows for standard experiments and the team is encouraged to solicit the support of the user community in optimizing the data processing .

Specific setups:
PXRD 1D (could be named Herd or Herdi)
The proposed 1D PXRD setup is very suitable for the intended use. The beamline staff posed the following specific questions

1. *Mythen I or II? I.e. end to end or overlapping modules?* The Mythen II is lighter and faster and seem to be the better choice in spite of the slightly bigger gaps that are unavoidable even with Mythen I. We prefer an end-to-end configuration of the panels rather than a staggered configuration, since the end-to-end configuration is tried-and-tested, uses the Debye-Scherrer cone optimally and is simpler.
2. *Is the radius of the detector the best option?* It seems adequate and good compromise between resolution and angular coverage
3. *Are the goniometer specifications realistic?* Yes, the TTH accuracy could possibly be specified to 10 µrad. We advise to motorize the roll and yaw for goniometer alignment, it is little cost compared to the increase in ease-of-use.
4. *Specifications of the SE table: Height? Load?* This is partially affected by the notion of it carrying a 2D detector. We are not fully convinced that the possibilities offered by this 2D detector balance the associated complications. With the new proposed placement of this instrument, the need for using the SE table for such a detector is even less clear as it could be placed at the end of the hutch.
5. *Is the MS sample spinner the best option?* It is a perfectly good option.

We recommend that the dataflow includes delivery of data in a choice of standard Rietveld/PDF software data formats to accelerate use of the data.

PXRD 2D:

The proposed 2D PXRD setup is very suitable for the intended use and the choice of the Pilatus detector is a good choice considering the budget.

Specific questions from the beamline staff include

1. *Distance from hexapod to beam - 350 mm?* It seems reasonable. With a large distance, however, the travel ranges are restricted. It might be worth (A) exploring the option of spacers beneath the hexapod to allow changing the distance and (B) to consider the need for additional travel range given the potentially limited travel range of the hexapod e.g. through addition of linear stages to extend the range.
2. *Which area detector is the best for this instrument?* The Pilatus is a good choice
3. *Should we have multiple area detectors?* Yes, the addition of a flat planel detector will be valuable (see above)
4. *Is a SDD of up to ~ 1000 mm sufficient?* For most routine use it is probably sufficient, but it would be good to preserve the option of longer distances. This is a renewed consideration considering the proposal to change the placement of the instruments in the hutch. We recommend that at least 2000 mm is kept as an option for good angular resolution. This is especially useful in connection with off axis placement of the detector. It is not clear if there is a horizontal (transverse) translation on the gantry to move the detector perpendicularly to the beam; this capability is important both for diffraction and DF microscopy.
5. *Necessary height and tilt of detector movement?* The proposed values are suitable in our opinion.
6. *Is it necessary with secondary focusing? Or just slits?* The options for secondary focusing are very good and a small investment to keep an interesting option.

Imaging:

The design looks plausible and with good likelihood of success. The design is more complex than standard tomography beamlines due to e.g. the dark field option (see general comments above).
We recommend that initial efforts focus on as automatic as possible standard parallel beam tomography with automated reconstructions and implementation of half-acquisition (off axis detector to generate twice the field of view) since this would add a lot of value for the users. This will ensure service to a majority of users with minimal load on the staff leaving the staff free to dedicate time to the more challenging experiments proposed.

For fast tomography, a balance will have to be struck between spatial resolution and time resolution. Smaller tomograms can increase the number of tomograms measurable at highest speed. Providing estimates of expected speed, data volumes and resolutions would be useful for the user community.

For the rotation stage, a two-stage Aerotech stage is proposed. This seems a good solution, but we have heard some concern from other facilities about integration of the electronics. We recommend that the team reaches out to beamlines with experience in this solution. We note that the community has good experience with LAB.

For the DF setup, a hexapod is proposed. Some concern was raised about the angular travel range being enough for topo-tomography (+/- 20 degrees would be suitable). The travel range should be checked taking into account the sample height above the stage. The load that can be carried by the hexapod is a compromise and it might be worth to reach out to vendors to see if higher load options are available.

As an alternative for the objective lens, it might be an option to explore the use of polymer lenses in addition to the Be ones since they are relatively cheap.

It may be an option to make the hexapod granite block and/or table top longer to allow secondary focusing to be here for the 2D diffraction experiment.

The speed of movement of the gantry is a balance between safety and efficiency and could be specified in more detail.

The committee congratulates the team on the work done and looks forward to seeing a working instrument.